The emergence of biofilms

Computational and experimental studies

Sheraton Muniraj, V.

Publication date
2019

Document Version
Final published version

License
Other

[Link to publication](#)

Citation for published version (APA):
Sheraton Muniraj, V. (2019). *The emergence of biofilms: Computational and experimental studies*. [Thesis, externally prepared, Universiteit van Amsterdam].
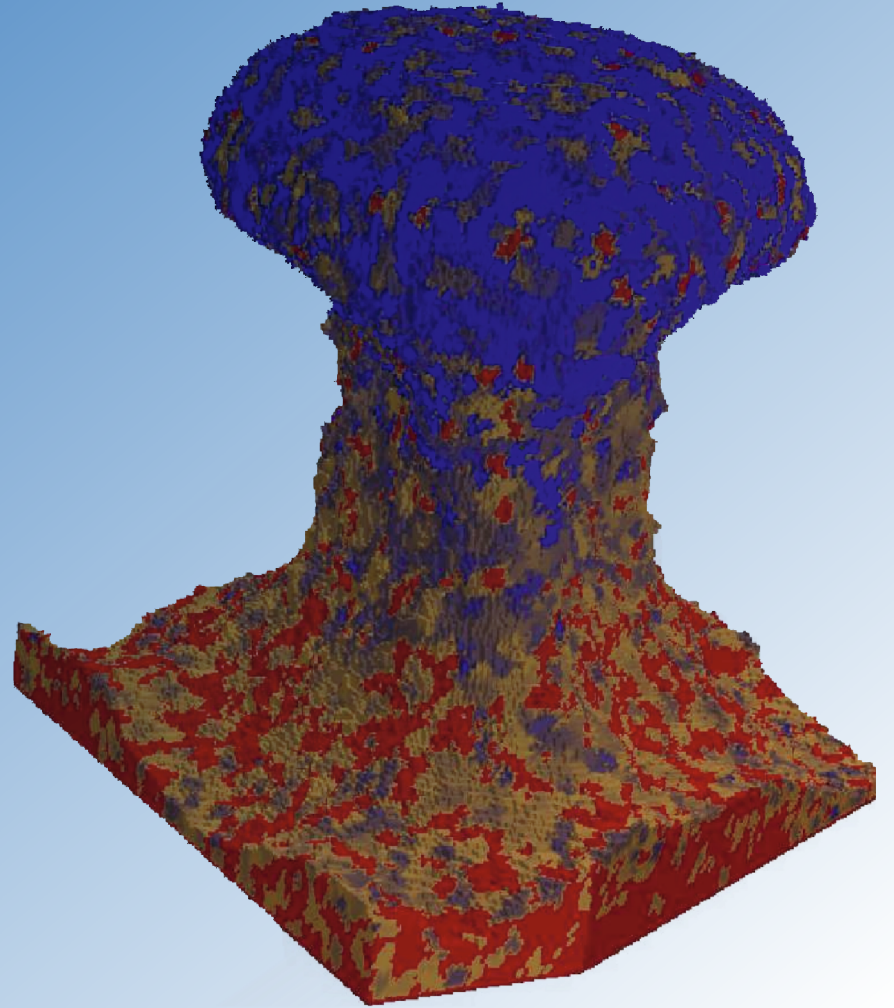
The Emergence of Biofilms: Computational and Experimental Studies

The Emergence of Biofilms: Computational and Experimental Studies

Vivek Shearton Muniraj

Vivek Shearton Muniraj

The Emergence of Biofilms: Computational and Experimental Studies

ACADEMISCH PROEFSCHRIFT

ter verkrijging van de graad van doctor

aan de Universiteit van Amsterdam

op gezag van de Rector Magnificus

prof. dr. ir. K.I.J. Maex

ten overstaan van een door het college voor promoties ingestelde

commissie, in het openbaar te verdedigen in de Agnietenkapel

op woensdag 19 juni 2019, te 12:00 uur

door

Vivek Sheraton Muniraj

geboren te Dindigul

Promotiecommissie:

Promotor:	prof. dr. P.M.A. Sloot	Universiteit van Amsterdam
Overige Leden:	prof. dr. R.M.H. Merks	Universiteit Leiden
	prof. dr. ir. A.G. Hoekstra	ITMO University
	prof. dr. A.H.C. van Kampen	AMC-UvA
	prof. dr. S. Brul	Universiteit van Amsterdam
	dr. J.A. Kaandorp	Universiteit van Amsterdam
Faculteit:	Faculteit der Natuurwetenschappen, Wiskunde en Informatica	

2

Contents

1 Introduction

.

   Bacteria are single cell organisms, which are ubiquitous in nature. They perform different functions in nature depending on their biological needs and can act as decomposers [1], pathogens [2], parasites [3] or just live as commensals [4]. The general life cycle of bacteria includes growth, binary fission, cell death and lysis. Different bacterial species use various metabolic mechanisms to attain cell growth. Two major metabolic mechanisms include heterotrophic [5] and autotropic [6] metabolism. Heterotrophic metabolism involves uptake of organic compounds by the bacteria, which are later oxidized to energy (ATP) and other organic compounds such as glucose, CO_2, etc. In autotrophic metabolism, the bacteria oxidize inorganic compounds such as iron, nitrogen and sulphur in order to acquire their required energy for growth and survival. Autotrophic metabolism encompasses photosynthesis carried out by bacteria such as cyanobacteria. In addition to growth and proliferation, the bacteria are also motile. For their locomotion, the bacteria are equipped with whip like structures called flagella [7]. These structures are also used as sensors to guide the motility of bacteria based on the chemical field [8] or heat signatures [9]. In order to survive, bacteria use different strategies during their lifetime to protect themselves from predators and get the optimal nutrient required for their growth. Some bacteria in their

environment live independently, that is, during the life cycle they proliferate, infect, and move without interaction with the spatially local bacteria. These independent bacteria are called planktonic bacteria [10]. The motile bacteria move across their surrounding using the flagella, a range of motion is exhibited such as swimming, twitching, sliding and gliding [11]. Their direct exposure to the environment makes planktonic bacteria vulnerable to antibiotics, viruses and other bacteriophages in their vicinity. To protect themselves from predators and reduce the hazards from antibiotics and toxic substances, bacteria generally aggregate together and form a single colony known as biofilm [12]. During this transition from planktonic to biofilm, the bacteria move towards the fluid-solid interface and lose their motility after contact with the surface to ensure that the structural integrity of the biofilm is not disturbed due to the motion inside the colony [13]. In addition to sessile behavior, bacteria express different levels of gene regulation before and after the transition from the planktonic to the biofilm state [14, 15]. Inside the biofilm, bacteria secrete enzymes, extra polymeric substance (EPS) [16] and other substances required to hold the colony in place and trap the required nutrients. Thus, the biofilm acts as a safe-house for the bacteria and also as a storage container of solutes [17], which may or may not be useful for the bacterial survival. Once a biofilm is established over a surface it can host millions of bacteria as a single community. EPS secreted by these bacteria act as an adherent and a protective layer guarding the community from external shear stresses, viruses, and antibiotics.

10

Though this is an ideal protection system for bacteria, it has detrimental effects on human beings. Around 80% of infections [18] in the human body caused by microbes originate from a biofilm rather from planktonic cells. Diseases such as cystic fibrosis in lung [19], periodontitis in teeth [20], endocarditis in heart tissue [21] and urinary tract infections [22] are a few diseases commonly caused by biofilms residing in human body. In addition to concerns in healthcare, industrial biofouling [23, 24] is another important field where biofilms have a devastating effect. For instance, the Embalse [25] nuclear power plant has been a victim of biocorrosion with biofilms being its major contributor. Biocorrosion in nuclear reactors or water distribution systems could lead to large scale disasters on public health and spending. Similarly, biofilms have been a major concern for public health throughout the world. A good example would be the listeriosis outbreak in South Africa [26] in 2017 where *Listeria monocytogenes*, a gram-positive anaerobic bacterium, was the reason behind the disease outbreak. It affected foetuses, new-borns, men and women alike, with around one fourth of the cases proving fatal with a death toll of more than 200. The outbreak started through processed meat and other refrigerated products. *L. monocytogenes* are capable of surviving in refrigerated conditions. Generally, during food processing, the food is treated with surfactants which renders these bacteria inert or kills them. However, L. *monocytogenes* can form biofilms, making the chemicals only partially effective on the biofilm population, whereby a part of the population survives and infects human hosts. Hence, interest on biofilm

removal research [27, 28] has increased considerably during the past years. In order to reduce the damage caused by such biofilms, it is important to remove the colony from its parent site. Removal of biofilm is a complex process, as previous research has shown, a single chemical or mechanical scrubbing process [28, 29] is not capable of uprooting and displacing the biofilm completely from the surface. This necessitates a deeper understanding of the dynamics behind formation and spread of the biofilm structures.

1.1 Structure of biofilms

The process of biofilm formation occurs in three distinct phases;

- Adhesion of initial colonizers

- Growth of colony

- Detachment and dispersion of bacteria

1.1.1 Adhesion phase

First, planktonic bacterial cells suspended in the liquid phase settle onto the solid surface. The settling process proceeds through two kinds of processes, active and passive settling. Passive settling involves cells settling due to effect of gravitational force and viscous effects of the suspension fluid. This passive process is relatively slower than the active settling process in which some cells propel themselves towards the surface using their flagella [30] and swim through the liquid. After they reach the surface, depending on the electrostatic charge [31] on

the surface, they secrete enzymes to make the surface suited for their habitat. Followed by the modification of the surface properties, bacteria settle on the surface and adhere to the surface. This process of adhesion is dynamic, the cells repeatedly attach and detach until they find a suitable spot, where their adhesion force to surface is maximum [32]. Once attached, the initial colonizers attract other planktonic cells towards their site of adhesion. The attracted cells adhere to the surface or to the colonizers to form a small colony of cells. Success of colonization of the surface depends on the adhesive characteristics of the bacteria [33]. In addition to adhesion characteristic of the cell, the quorum sensing (QS) phenomenon of bacterial population determines the extent of surface colonization [34, 35]. QS involves inter-bacterial communication through passive diffusion [36] of signal molecules secreted by the bacteria. The bacteria in the biofilm have been shown to sense population density and vary gene expression of cells through QS signaling [37]. In addition to QS, there are also mechanisms through with bacteria can suppress the QS activity, known as Quorum Quenching (QQ) [38]. After the colonizing bacteria settle on the surface, they start to proliferate and establish a suitable base for bacteria to thrive on. This stage is the onset of biofilm formation. During this stage, there is no definable shape or overall structure to the biofilm, since the cells could spread out as they are yet to secrete EPS.

1.1.2   Growth phase

The next stage of biofilm structure evolution is the proliferation of the bacterial cells utilizing the nutrients surrounding them. Most bacteria [39] use organic substrates such as glucose, fructose, and simple sugars as their growth medium. There exist bacteria which thrive in places where there is no oxygen, anaerobic [40], and other bacteria which survive by feeding on metal ions [41], for simplicity and easier understanding we consider only the aerobic bacteria that feed on organic substrates for their growth throughout this work. One important parameter that decides the final shape of the biofilm is nutrient concentration. If the substrate is available in abundance, then the cells grow and divide at a faster pace. The rapid growth results in formation of thick slabs of biofilm [42] around 200-300 µm thickness, that can be observed in most natural flow systems. Under average amount of substrate availability, the cells at the bottom are devoid of nutrients while the cells at top are exposed to relatively high concentration of substrate. Therefore, cells at the top proliferate faster than cells at the bottom. The cells keep stacking over themselves, forming layers of cells over each other, resulting in a structure similar to a heap of sand. Finally, if the nutrient availability is scarce or minimal, then the growth of cells is retarded. Also, due to nutrient deficiency, cell deaths occur inside the biofilm, mostly localized at the bottom parts of the biofilm where the nutrient diffusion or permeation is too low. Such biofilms grown under nutrient deprived conditions result in finger-like projections [43] or structures resembling mushroom shapes [44]. Few

studies have tried to elucidate on the mechanism behind the development of such structures. Klausen et al. [44], designed a system where they used two strains of Pseudomonas aeruginosa bacteria, one is a wild-type with no mutations, the other, a motility mutant which cannot move actively using its flagella. When these two strains were mixed and co-cultured in lab, they formed a biofilm with mushroom shape under low nutrient condition. It was observed that the wild type cells always occupied the top or cap of the mushroom, while the motility mutants were found at the bottom. This suggests that biofilm structure formation depends on cell motility [45] contribute from active motion or from cell chemotaxis. It is important to note that mushroom biofilm structures are one of the toughest biofilm structures that cannot be detached from parent site. The cap of the mushroom structure acts as protective shield against the fluid shear and host majority of growing biofilm population inside it and exposes them to fresh incoming nutrients. In the event of a cap getting detached due to fluid shear, the stalk of the mushroom remains rooted and the cap can redevelop at the same spot. These structures could lead to pressure drop in flow pipes, heat exchangers and boilers [46], which in turn can lead to serious break down and machine damage.

1.1.3 Displacement phase

The final stage of biofilm life cycle is the displacement of bacteria [47] from the parent site. Removal or displacement of bacteria from the parent biofilm site can occur in two different process namely

detachment [47] and dispersal [48]. The passive removal of cells of the biofilm due to external stimuli such as pressure, fluid shear or structural failure be collectively termed as detachment. This type of bacterial removal is seldom initiated directly by the bacteria within the biofilm [49]. Detachment can proceed in multiple ways such as erosion, sloughing and abrasion. Erosion involves removal of few cells of the biofilm due to fluid shear or external pressure. Erosion could be a continual or an intermittent process depending on the environmental constraints. Sloughing is different from erosion in that it involves removal of chunks of biomass, instead of few smaller groups of cells. Sloughing is quite common in biofilms experiencing high fluid shear or when they are structurally unstable. Abrasion occurs due to physical impact of moving or floating particles around the biofilm. Due to the lack of active role of bacteria in the displacement process, detachment is considered as a passive process. On the other hand, removal or ejection of cells from biofilm due to processes such as production of enzymes, extracellular surfactants or other factors by the bacterial cells is termed as dispersion, which is the active process of biofilm removal. Biofilm dispersal could be treated as an analog to dispersion of seeds or pollen from plants. After dispersion of bacterial cells from the parent site, the cells search for new sites to colonize and repeat the life cycle. Biofilm dispersion has a become a subject of intense research in past decade. Researchers have attempted to understand dispersion using multiple analysis techniques such as proteomics [50], calorimetric methods [51] and even gene expression profiling [52]. QS signaling

has also been implicated as a major player in the dispersion processes [53].There have been many contradictory findings reported in literature, for instance, nutrient limitation has been reported as an initiator of biofilm dispersion in *Aeromonas hydrophila* [54], while high nutrient concentration initiated dispersion in Acinetobacter [55]. Similarly, the influence of cell motility on dispersion has not been clearly understood, Tolker-Nielsen et al. [13] showed that flagellar-motility was involved in dispersion while research by Morgan et al. [50] proved motility was not necessary for initiating dispersion. These observations present an unclear explanation for dispersion; a process initiated by bacteria, which breaks the microenvironment that it had already built.

1.2   Biofilm ecosystem

In short, bacterial biofilm is a complex system which exists and evolves as a result of interactions between millions of bacteria within the biofilm and external factors such as nutrients, fluid shear and QS signaling outside the biofilm. Such complex systems cannot be analyzed and understood, by generalizing their overall behavior to the behavior of its individual members. Therefore, the core aim of this thesis is to unravel the underlying mechanisms behind the physical transformations of bacterial biofilms, which arise from the complex interactions of the biological, physical and chemical components present in the system. Due to diverse behavior and biological makeup of individual bacteria, it is often not possible to generalize any

phenotypic expression or evolutionary behaviors on all bacterial species.
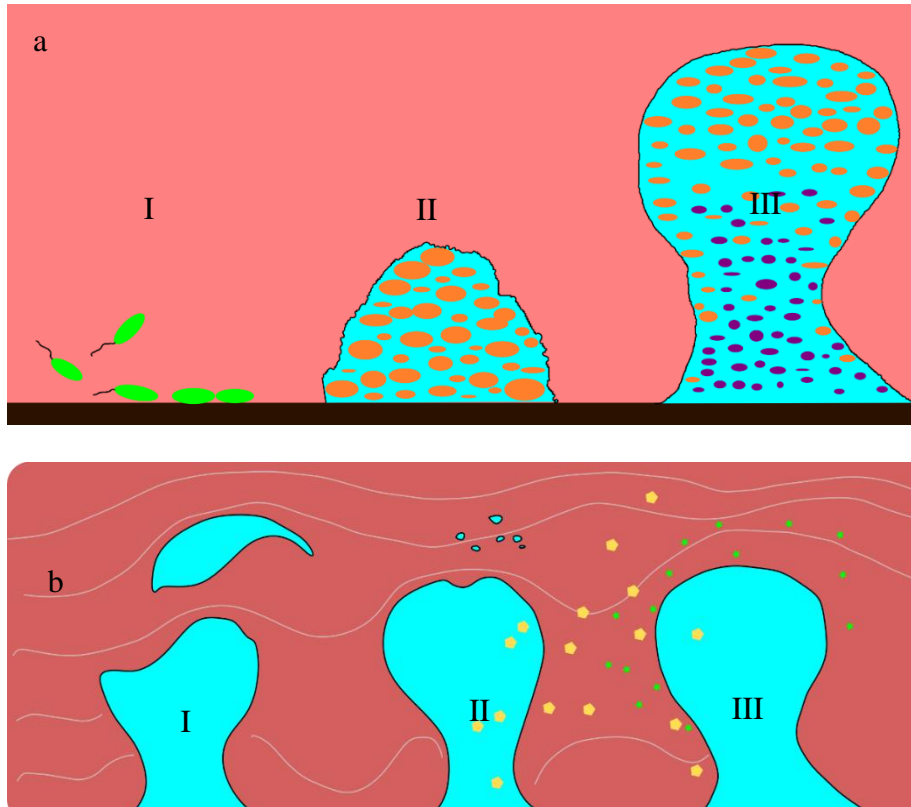
Figure. 1.1 Summary of biofilm phenomena analyzed in this thesis. (a) Various stages of biofilm growth in the presence of a nutrient field, (I) settling phase, (II) cell proliferation and (III) developed mushroom-shaped structures. The green colored cells indicate settlers, orange cells indicate proliferating cells, violet cells indicate dormant and dead cells, blue color indicates the EPS in the biofilm and the surrounding peach color indicates the substrate field around the biofilms. (b) Consequences of fluid flow in the biofilm ecosystem, (I) sloughing and (II) erosion of biofilm due to fluid shear and (III) intra- and inter-biofilm

QS-QQ signaling. The yellow pentagons and green stars denote the QS signals and QQ signals respectively. The dark peach background indicates the fluid field, with the white lines denoting the flow path.

The works presented in this thesis are centered around two bacterial species, *Pseudomonas aeruginosa (PA)* and *Escherichia coli (E. coli)*. The reason for the selection of these model organisms is because of their significance on human health, their abundance in nature and the availability of vast literature/data for it [56, 57]. PA are rod-shaped bacteria with flagella protruding from the shorter edge of the body. It can exhibit both lifestyles – planktonic and biofilm. *E. coli* is a gram-negative bacterium and has a similar body structure as PA. These two model organisms will be used as both mutants and wild-type in the studies included in the thesis. Due to the intertwined nature of the interactions and the evanescent consequences of these interactions, it is rather impractical and time-consuming to analyze the underlying mechanisms of biofilm transformations solely through experiments on the model organisms.

1.3   Emergence of biofilms

What are the crucial physical and biological drivers steering the spatiotemporal evolution of bacterial biofilms? – this is the core question which is explored in this thesis. More specifically, three sub-questions derived from this core question are examined in detail. They are, *how does spontaneous evolution of different biofilm shapes occur in nature? what are the ecological determinants of inter-biofilm*

signalling outcomes? and *how do external physical stresses and internal biophysical cell properties affect the structural integrity of biofilms?* In this thesis, the mechanisms governing these phenomena are unraveled through studies involving both experiments and numerical simulations. The numerical simulations are executed using cell-level mathematical models, capable of handling the intricacies present in the biofilm's ecosystem. A general overview of the mathematical models used in this thesis is presented in chapter 2. An in-depth explanation of individual model is offered in the corresponding chapters, where the model is implemented.

The thesis revolves around three major phenomena associated with bacterial biofilms. The first phenomena analyzed in this thesis pertains to the spontaneous formation of diverse biofilm morphologies in response to the ambient substrate availability. This phenomenon is discussed in chapter 3 of the thesis, which includes experimental and simulation studies carried out using PA biofilms. In addition to analyses on the shape formation principles, the effect of these shapes on the antibiotic resistance levels is also discussed. Chapter 4 analyses the community level effects of QS and QQ signaling. The experiments and the simulations are carried out with mutant *E. coli* bacterial strains capable of expressing QS, QQ and fluorescence. The effects of fluid shear on the biofilm structure is examined in chapter 5 using numerical simulations. These three chapters capture spatiotemporal evolution of the biofilm system in response to external stimuli namely, substrate field (chapter 3), QS-QQ field (chapter 4) and fluid flow field (chapter

5), as summarized in fig 1.1. Chapter 6 discusses the parallel computation efficiency of the multi-physics implementations in the numerical models developed for biofilm growth. As such, analysis on the biofilm interactions are not discussed in this chapter. This chapter is dedicated to the optimization of the computational models developed in the previous chapters (3-5). Chapter 7, the final chapter, elucidates the major conclusions from the studies and provides a glimpse of the possible future works and model extensions.

2 Computational framework

Most phenomena observed in nature are outcomes of cascades of events triggered by single or multiple precursors. For example, consider a school of fish evading a predator attack. Of the thousands of fishes in the school only a few fishes sense or see the predator. These early detectors then adjust their course of swimming to avoid the predator. Inferring a predatorial attack, the other fishes in the school respond to this movement and coordinate in evading the attack of predator by moving away from the predator in multiple ways as shown in fig. 2.1. During this phenomenon there are multiple events occurring. First, the observer fishes are communicating with their nearest neighbors. Then, the other fishes change their course of swimming away from the predator. Factors such as the relative position of the prey, velocity of ambient water, size of the school all determine the outcome of the event. In this phenomenon of natural enemy evasion, the predator's movement is the precursor which triggers the movement of the entire school. Such systems can prove difficult to be studied through a holistic approach since, generally such events have multiple actors and multiple dynamics interacting with each other in the system at different scales.

Figure. 2.1 Response to a predator's attack from a school of fish. Red colored fish indicates the predator and black colored fishes are the evaders.

2.1 An object and its constraints

The optimal way to analyze and understand such systems is through deciphering the actions and consequences of the individual members making up the system and the field affecting such systems. In the case of predator – school model, the fishes are the individuals and the fluid surrounding them is the field. Each member of such system has their own set of characteristics, physical or biological. These characteristics acts as constraints to the ways the system can evolve. In addition to the characteristic constraints, there exist environmental constraints established by the spatial positioning of the prey and predator, the fluid dynamics and the other ambient conditions (such as gravel depth). Table 2.1 lists the members, characteristics and environmental constraints and member actions.

Table 2.1 The objects and their constraints

Object	Characteristics	Environmental constraints
Fish	Movement Predator sensing Communication Finite size	Crowd dynamics Response propagation
Fluid	Viscosity Density Pressure	Stream direction Fish motion Solid obstacles Fish density

As such, there are no simple experimental ways to study such multi-actor and/or multi-scale systems without compromising the complexity associated with such systems. One way to simplify such systems for experimental studies is to limit the number of actors involved. However, such compromised systems may not replicate all the dynamical outcomes possible for the original system. For instance, the reduction in number of prey fishes can result only in an evade response, and any other outcomes observable in a natural school system may not be feasible. Therefore, to study such evolving complex systems, a framework capable of handling all the actors, environmental factors, actor-actor interaction and actor-environment interaction is required. Computational models offer such elaborate framework capable of capturing the physical and biological dynamic properties

associated with complex systems. These methods allow for a wide range of parameters for defining the problem and are limited only by the computational power and time. Every computational method has two major aspects associated with the model development which determines the rigorousness of the model. Defining the conceptual basis or the physical principles is one of the aspects of computational modelling. The conceptual basis can be a physical law, a biological behavior or any other definition of quantifiable/observable processes in a system. In the case of the fish school, the fish's movement and fluid flow, governed by Navier-Stokes equation has to be defined as a conceptual parameter in the model. The numerical basis for solving such concept definitions is the second aspect of model development. In case of fluid flow, the Navier-Stokes equation can be solved by simplifying it to analytical solutions or by implementing sophisticated finite element model-based simulations. Therefore, it is always necessary to validate both the conceptual and the numerical basis used in problem definition. The validation of simulations can be carried out by comparing the simulation results against analytical solution or experimental data. The numerical methods used in the simulations have to be benchmarked against the analytical solutions. In almost all cases, such analytical solutions may not be available for the problem in consideration. Therefore, the planned numerical basis has to be tested for stability and validated against analytical results available for a simplified/similar problem. Experimental data from a less complicated problem observation has to be used for the validation of conceptual

basis. This data could be from an experiment with fewer number of fishes in the school, to analyze the response time of the fish after it encounters the predator.

2.2 Biofilm models

Computational modelling can be used to explore the dynamics of biofilm formation and evolution. Similar to fishes in the school, the bacteria are the actors in the biofilm. The bacteria possess characteristics such as motility, cell growth, cell division and protein secretion. They interact with each other through cell-cell adhesion, communication and physical space adjustments. The environment or the field of the biofilm comprises of nutrient sources, antibiotic solutes, extra-cellular matrix and other abiotic components. The bacteria interact with the field and changes the local dynamics of the field which changes the overall development cycle of the biofilm and in-turn influences the spatio-temporal evolution of the field. Biofilm simulation models for predicting the growth dynamics of bacteria date back to as early as 1976 [58]. The early models focused primarily on the volume increase or quantification of bacterial growth within the biofilms. Williamson and McCarty [58] developed a simplified one-dimensional model for studying bacterial growth in the biofilm structure. As such, the bacteria were not treated as separate actors or entities in the model. Instead, they were modelled as mass points or biomass occupying a finite space in the simulation domain. They modelled the diffusion of substrate (nutrient) using Fick's law of diffusion (eq. 2.1) in one dimension through a liquid-film-media

interface. In equation 2.1, C indicates the concentration of the substrate, D is the diffusivity of the substrate and t is the time.

$$\frac{\partial C}{\partial t} = D\nabla^2 C \tag{2.1}$$

The consumption rate of the substrate or the solute uptake by the bacteria was determined based on the available solute concentration and the biomass concentration of the bacteria occupying a finite space. The growth rate of the biomass was calculated in accordance with the Monod kinetic equation. The increase in the biomass was then translated to increase in the overall thickness of the biofilm in one-dimension. This simplified model has been the basis for the future biofilm model development. Recent research works on biofilm growth modelling have focused on improving the numerical accuracy and implementing cell-level interactions. However, the conceptual basis which are the definitions of bacterial growth, nutrient uptake and solute diffusion has remained the same in the previous decades. Benefield and Molz [59] extended the one-dimensional model to estimate the solute concentration in a three-dimensional space. They implemented a finite difference scheme to solve Fick's law, Monod kinetics and solute advection. The basic aim of the study was to explore the relationship between solute advection and biofilm growth dynamics. Similar to the previous model [58], the entire biofilm community was treated as a collection of mass points without any individual characteristics or unique member identity for the bacteria. Kissel et al., [60] developed a numerical model to understand the competition between multiple

species in a biofilm structure. They model the growth of bacteria in aerobic and anaerobic conditions comprising of five different solutes and effect of such solute variation on the multi-species population balance. This study showed the impact of mass transfer and bacterial competition for nutrients on the community population in a heterogeneous biofilm. Wanner and Gujer [61] further improved this idea by extrapolating the species balance to independent biofilm layers rather assuming the entire biofilm as a single entity. A practical application of such model in a porous media emulating the ground water environment was carried out by Molz et al. [62]. These developments constituted the first phase of biofilm modelling and focused majorly on the growth dynamics associated with the biofilms. Thus, in the early studies, even without introducing a higher level of complexity through assuming bacteria as individuals, research groups were able to show the relevance of simulation models in understanding the biofilm dynamics and design of practical applications.

The second phase of biofilm modelling research started to focus on more sophisticated features associated with the biofilm development. During the early 1990's, the research questions started to get more extensive and questions such as the influence of the biofilm morphology on nutrient distribution[63], antibiotic resistance development [64] and fractal pattern investigation [65, 66]. Simulation models shifted from quantifying growth rate to precise characterization and system evolution of biofilm. The modelling methods started to increase in complexity to include the spatio-temporal interactions

between the cells and the surrounding field. Stewart [64] included antibiotic solute concentration as a field in the simulation model to analyze the effect of antibiotics on the biofilm structure. From his simulations, he observed the competition between bacterial proliferation and efficacy of the antibiotic. The model was able to account for the increased antibiotic resistance observed in thicker biofilms. Therefore, he hypothesized that biofilm simulations can be used in the future to drive the design of experiments. De Beer et al. [63] implemented a hybrid experimental data driven simulation to understand the morphology driven nutrient distribution in the biofilms. They used confocal images as an input to triangulate the position/morphology of biofilms in the experiments. Using mass transfer kinetics, they were able to establish the oxygen concentration profiles within the biofilms in a two-dimensional simulation domain. This stands as an evidence that computational modelling can be used to reveal data which could otherwise be impossible to obtain experimentally. Biofilms have been long known to form fractal patterns during their growth. It has been found that diffusion limitation has been a driving force behind the formation of such fractal patterns [66]. Hermanowicz et al. developed a theory to quantify the fractal dimension based on the height of the biofilm and the substrate concentration. These spatial characteristics would be straight-forward to model using discrete spatial methods such as cellular automata.

2.2.1 Cellular automata

During the early 1940s, cellular automata (CA) [67-70] were a discrete computational method developed by John von Neumann. CA consists of a computation domain represented as two-dimensional cartesian grids which host automatons in the individual square grids as shown in fig. 2.2. In general, these automatons are controlled by algorithms which dictate their movement or replication within the domain. These automatons have neighbors that reside within a specified Manhattan distance [71] from them. There are multiple neighborhood schemes which can be defined in a CA model. A few of those two-dimensional schemes for neighborhood are shown in fig. 2.2. The Von Neumann scheme is the simplest neighborhood allocation scheme which allots a distance of one grid square for a neighborhood. Therefore, any automaton which is in contact with the edges of another automaton is considered its neighbor. Thus, an algorithm for CA modelling can take the states of the neighbor as an input and model evolution of an automaton. This makes the outcomes of a CA model dependent on the spatial and temporal states of the automatons in the domain. There are higher order neighborhood schemes which were developed to prevent anisotropic effects prevalent in models implementing von Neumann neighborhood. These models can consider cells which are in contact with the edges of the automaton and also cells which are completely not in contact with the automaton in consideration. Such contactless neighborhood schemes can be used to simulate density dependent functions and other force effects such as

Van der Waals forces. CA has been used to model and understand different complex systems including but not limited to immune system modelling [72-75], tumor growth[76, 77], language processing [78], finance [79] and fluid flow [80, 81].

The working principle behind cellular automata for biological systems is that macroscopic phenomena observed in the physical world are a result of interactions between physically identical microscopic entities. These micro-scale interactions are the building blocks for the evolution of a larger system and dictate the transitional states of the system. Hence, in order to predict the spatiotemporal behavior of real-world biological systems, it suffices to model the cells along with their surroundings. In a simplified model of cellular automata (CA), the cells are the automatons and are allowed to take discrete positions at grid squares (2D) or grid cubes (3D) in the domain. The cells can then be designated a specific state (such as dead "0" or live "1" for bacterial cells) and their interaction with their neighbors can be programmed as a set of algorithmic rules or mathematical functions. The time and space domain of the grid are discretized and at each instant the cell can represent any one of the defined states. As the simulation progresses for every time step, the cells can interact with their neighbours and evolve based on the rules specified. The outcome of the rules is used to update the state of the cell at that instant. This procedure is repeated iteratively for desired time interval. The entire domain may be n-dimensional depending upon the model requirement.
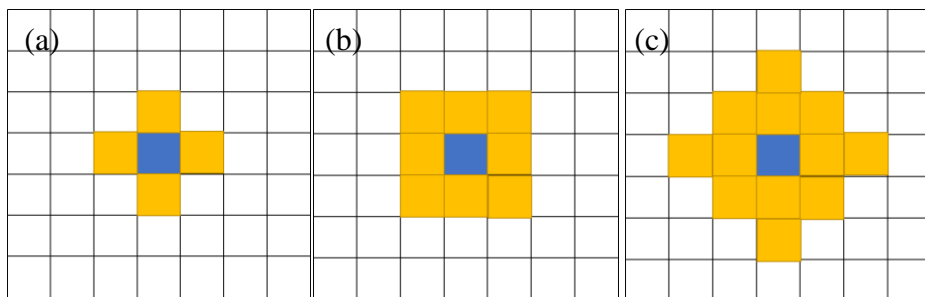
Figure. 2.2 Possible neighbors for the cell at the center as defined by, (a) von Neumann, (b) Moore and radial neighborhood schemes. The blue cell is the cell of interest and the yellow cells indicate its neighbors.

The spatial nature of CA models has made it an efficient tool to study the structural dynamics of biofilm development. Colasanti [82] proposed that cellular automata can be used to model microbial colonies. Later, Wimpenny and Colasanti [83] developed a conceptual model to understand three different common structures observed in biofilms (1) heterogeneous mosaics, (2) dense and (3) porous morphologies. They hypothesized that these structures were formed as a consequence of the nutrient distribution rather the biology of the bacterial cells. Using a very simple stochastic 2D CA model, they were able to simulate the branching structures found in biofilm. The same model was also able to replicate the formation of dense biofilm structures at a high substrate concentration. Following a similar approach Picioreanu et al. [84] developed a hybrid differential-discrete

cellular automaton model to study the surface complexities of biofilms. They were able to use a model to simulate 2D finger-like projections which arise in nutrient scarce conditions. Hermanowicz [85] independently proved that simple 2D CA models can be used to recreate complex structural patterns found in biofilms. Various other models have implemented CA to simulate mixed culture [86], antimicrobial activity [87] and detachment [88]. However, CA models have been well known to suffer minor limitations while simulating EPS present in the biofilms. Since the EPS is assumed stationary in CA models, there is always a vacuum created in the place of bacteria after they decay in the simulations. Similarly, CA models cannot account for any mechanical constraints which would arise from the dense packing of the automaton. In order to overcome these limitations, Individual-based models (IbM) [89, 90] were developed. IbM follow the same theory as CA except that the algorithmic rules are applied to individual bacterial cells instead of grid squares. The model considers bacterial cells as hard spheres which do not intersect each other. The spheres are of fixed size, they can divide and change to live or dead state. EPS modeling was possible using IbM models due to their ability to include forces or Leonard Jones potential [91, 92]. IbM has well known limitations such as artificial porosity introduced due to lack of tight packing of cells, numerical artifacts arising from assumption of spherical particles and formation of physically unrealistic colony structures.

2.2.2 Glazier-Graner-Hogeweg model

Cellular automata have a few limitations that prevents them from replicating the exact physical and biological processes. A major concern of using cellular automata for representing biological processes is the absence of direct ways to account for the energy changes arising from the change of states of the system. Due to lack of energy restrictions in the models, cellular automata can give rise to physically unmeaningful states. For instance, consider a single cell which is about to grow in size. In cellular automata or agent-based models, this growth of cell can be modelled as an addition of extra grid point to the existing cell. This increase in size is modelled by an algorithmic rule, such as, the cell can increase its size by one grid pushing a neighbor's grid in the same direction as shown in fig. 2.3a. Alternatively, the cell can stop its growth depending upon the neighbor density as dictated by the algorithm. Both these cases may not truly represent the actual physical dynamics of the system. Biologically, the cell must increase its size in such a way that it maintains mechanical equilibrium with its neighbors. In real world physiological conditions, the cell grows in a direction which has a least resistance for growth or it pushes the neighbors in a way to minimize the energy of the entire structure or the cell growth is arrested inherently as shown in fig. 2.3b. It is clear that the outcomes of any such physically meaningful adjustments depend upon the mechanical and biological spatial constraints experienced by the cell. Therefore, a model to represent any biological structure should have clearly defined energy-based restraints

which prevent the system from any run off resulting in biologically inconceivable states.

a. Simple rule-based method – cell growth

Cells

Cell size increase

Rule 1: Increase the size of the cell in the middle by 1 μm
Rule 2: Adjust nearest neighbor accordingly

b. Energy-based method – cell growth

Optimal growth configuration

$\sigma\left(\vec{i'_1}\right)$

$\sigma\left(\vec{i'_2}\right)$

No size increase

$\sigma\left(\vec{i'_3}\right)$

Multi-type cell sorting
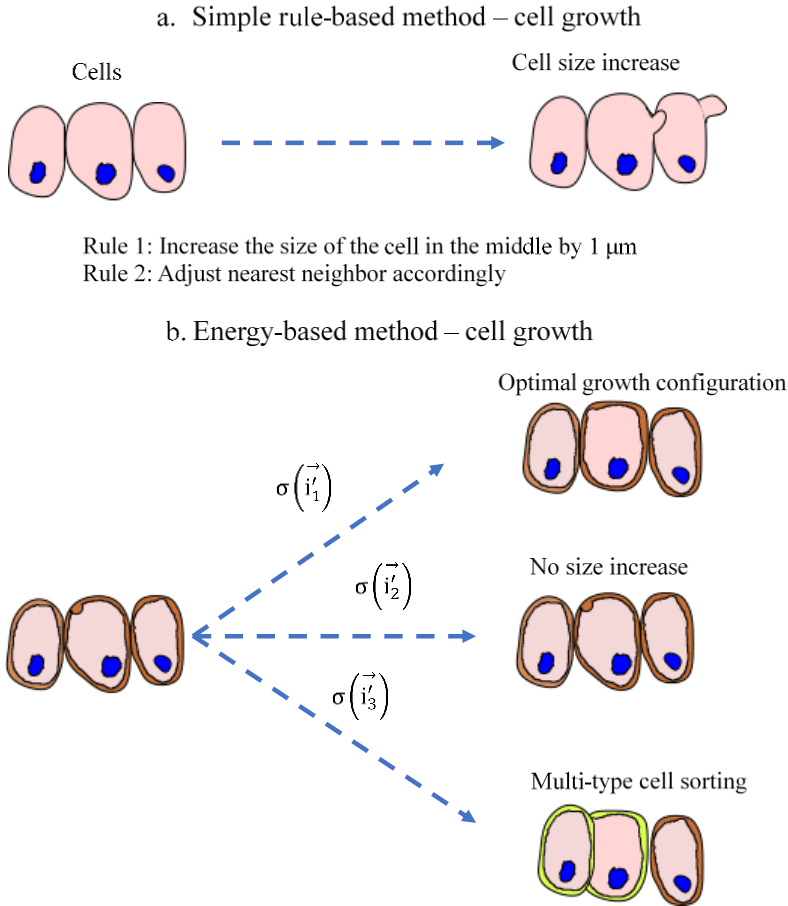
Figure. 2.3 Cell growth as modelled by, (a) simple rule-based method and (b) energy-based method. Different colors of the cells indicate the cell types and the ring around the cells in the energy-based method denotes the adhesion potential.

The Glazier-Graner-Hogeweg (GGH) [93] method is a computational method which offers the freedom of modelling discrete biological cells bounded by discrete or continuum based energy constraints. The history of GGH model can be traced back to the large q-Potts model (qPM) and Cellular Potts Model (CPM). During its initial stages of development, qPM was used in studying crystal growth [94] and coarsening of soap froth[95]. qPM and CPM based models incorporated Hamiltonian energy functions to define the surface energy changes of the individual soap bubbles. The model assumed that the object (froth or crystal) under definition occupies one or more regularly-spaced lattice points in the computational domain. The Hamiltonian (eqn. 2.2) is used to compute the energy changes arising from interactions of neighbouring degenerate spins of a lattice site.

$$H = \sum_{neighbours} 1 - \delta_{\sigma(i,j,k),\sigma(i',j',k')} \tag{2.2}$$

Here, i,j,k and i',j',k' are the lattice coordinates, σ is the spin associated with the lattice site and δ is the Kronecker delta function, which decides the bonding between the sites (0 or 1) based on the spins. The number of possible spin values 'q' decides the possible number of configurations arising from the 'N' spins in a lattice site. There are q^N configurations possible, which is very large to be computed, hence impossible to solve analytically. To model the transitions from one configuration to other, Monte-Carlo method proposed by Ashkin and

Teller [96] can be used. The probability 'p' of jump from one configuration ($\sigma(\vec{\iota})$) to another configuration ($\sigma(\vec{\iota'})$) is given by equation 2.3. Here, T is the system temperature or fluctuation amplitude. It should be noted that out of all the possible q^N configurations, most configurations will tend to have high associated energies therefore less probable of occurring.

$$\frac{p\left(\sigma(\vec{\iota}) \to \sigma(\vec{\iota'})\right)}{p\left(\sigma(\vec{\iota'}) \to \sigma(\vec{\iota})\right)} = \frac{e^{\frac{H\{\sigma(\vec{\iota})\}}{T}}}{e^{\frac{H\{\sigma(\vec{\iota'})\}}{T}}} \tag{2.3}$$

qPM models lack the dynamics needed to define a biological system. Since, biological systems do not jump between different configurations but rather transition through local cell-cell interactions, these models cannot be used to investigate cell level events in biological systems. In addition, CPM models support only a single contact energy constraint between the spins, but biological cells vary in their membrane contact potentials. A modified Metropolis algorithm [97, 98] used in GGH treats the individual cells as unique objects with their own contact potentials. The modified Metropolis algorithm (MMA) considers the energy changes arising from configurational changes happening at a single lattice site. Thus, the transitions following MMA retain memory of the previous configuration and the transition to consequent configuration is dependent on it. From a biological standpoint, while implementing MMA, instead of a cell abruptly changing its boundaries with a nearby cell (as done in Monte-Carlo method), it gradually changes its shape by minimizing the energy

associated with intercellular contact. Figure 2.3b summarizes the general steps in the MMA implementation. Thus, the probability of a lattice/index copy attempt is given by,

$$P\left(\sigma(\vec{\imath}) \rightarrow \sigma(\vec{\imath'})\right) = \left\{\exp\left(-\frac{\Delta H}{T_m}\right)\right\} \qquad \Delta H > 0; \qquad (2.4)$$

$$P\left(\sigma(\vec{\imath}) \rightarrow \sigma(\vec{\imath'})\right) = 1 \qquad \Delta H \leq 0; \qquad (2.5)$$

$$\Delta H_{contact} = \sum_{Neighbours} J\left(\tau(\sigma(\vec{\imath})), \tau(\sigma(\vec{\jmath}))\right)\left(1 - \delta_{\sigma(\vec{\imath}),\sigma(\vec{\jmath})}\right) \qquad (2.6)$$

Where $P\left(\sigma(\vec{\imath}) \rightarrow \sigma(\vec{\imath'})\right)$ is the probability of success of a single index-copy attempt of an entity from one lattice/grid point to the other, ΔH is the change in energy associated with the copy attempt and T_m is the temperature/fluctuation amplitude term. The change in contact energy due to the contact between neighbor cells is quantified by the Hamiltonian in equation 2.6. $J\left(\tau(\sigma(\vec{\imath})), \tau(\sigma(\vec{\jmath}))\right)$ is the contact potential between cell types (τ) of cells (σ) present at lattice positions $\vec{\imath}$ and $\vec{\jmath}$. Since the probability of index copy attempt is inversely proportional to the energy change associated with the index copy, the system will minimize its internal energy as successive copy attempts proceed. In order to properly define a biological system, in addition to the contact energy, other potentials such as growth potential, volume constraints and cell division constraints are needed. GGH model

39

implements these terms using a combination of Hamiltonian and non-Hamiltonian functions. For instance, the increase of cell volume can be coupled with the internal energy using the Hamiltonian ΔH_{vol} defined in equation 2.7, where $v\left(\sigma(\vec{\imath'})\right)$ and $v\left(\sigma(\vec{\imath})\right)$ are the volume of the cell containing the target and source grids respectively, λ_{vol} is the volume constraint parameter (stability parameter) and V_t is the target volume up to which the cell is capable of growing. This algorithm is implemented throughout all the cells in a simulation domain at every instance of time (named as Monte Carlo Steps, mcs).

$$\Delta H_{vol} = \Delta H_{vol}^{new} - \Delta H_{vol}^{old} \tag{2.7}$$

$$\Delta H_{vol}^{new} = \lambda_{vol}\left(v\left(\sigma(\vec{\imath'})\right) + 1 - V_t\left(\sigma(\vec{\imath'})\right)\right)^2 \tag{2.8}$$

$$\Delta H_{vol}^{old} = \lambda_{vol}\left(v\left(\sigma(\vec{\imath})\right) + 1 - V_t\left(\sigma(\vec{\imath})\right)\right)^2 \tag{2.9}$$

By applying equations (2.7), (2.8) and (2.9) in equation (2.4), the algorithm finds if the total energy is minimized in the volume expansion process, if true (P > 1), pixel-copy attempt is executed, else the copy attempt is ignored. The Hamiltonian functions are additive in nature. Therefore, the total change in internal energy from contact potentials and cell volume changes can be calculated as $\Delta H_{contact} + \Delta H_{vol} = \Delta H$.

Non-Hamiltonian functions are used to define cell events such as cell division or cell death. In case of cell division, a cell σ is divided

into two daughter cells σ' and σ''. These daughter cells are assigned new indices and give part of the parent's lattice sites, generally half the number of parent sites for each cell. During this division event, the daughter cells' target volume is reduced to the new volume, so that the internal pressure of the cell keeps itself stable. Similarly, for the case of cell death the target volume can be set to zero, leading to gradual buckling of the cell or the cell's index can be deleted denoting a complete cell lysis.

In all the biofilm models described in the forthcoming chapters, Compucell3D [99] framework is used for numerical simulations. Compucell3D is an open source software implementation of GGH model used to simulate the cell behavior and ambient conditions. Compucell3D provides a GUI for visualizing the simulated dynamics of cells. The core section of Compucell3D is coded in C++ and the built-in modules can be accessed using Python interface. This combination ensures that the core runs efficiently, owing to its precompiled nature, and the modules in the core can be directly called using the python interpreter during runtime, eliminating the need for additional compilation.

2.3   Mass transfer and Computational Fluid Dynamics:

Compucell3D renders a simulation toolkit adequate for simulating and visualizing cell level activities. Therefore, we can define and model our object (bacteria) and its associated characteristics (cell behaviors). But Compucell3D lacks appropriate tools for defining

41

the environmental constraints that affect bacterial proliferation and consequently biofilm evolution. These constraints can include nutrient fields, antibiotic solutes, fluid flow and external forces. Hence, in addition to GGH model, other mass transfer and fluid dynamic models are required to completely define the biofilm ecosystem. These models must be coupled with GGH model at spatial (lattice) and temporal levels to properly synchronize the biological activities of cell and the ambient physical processes.

A simplified metabolic growth process of bacteria will include glucose uptake from the surrounding, mass increase in proportion to the uptake and cell division based on the cell volume and mass. The last two processes, mass increase and cell division, can be simulated using GGH models. The former process, glucose uptake, can be broken down further into glucose transport through convection, glucose diffusion and cell mass-based glucose consumption. For calculating the spatial concentration of glucose transported through convection, we need to estimate the spatial velocity of the fluid carrying the solute (glucose). This can be efficiently modelled and quantified using various Computational fluid dynamics (CFD) techniques. CFD is a discipline concerned with the use of numerical methods to solve the mathematical equations governing fluid flow. The following are the basic steps involved in formulating and simulating a CFD model,

The first step is to develop a numerical description of the flow in the domain of interest [100]. In general, Navier-Stokes equation (eq.

2.10) and other complementary mass conservation equations are used in defining the system.

$$\rho(\vec{u} \cdot \nabla)\vec{u} + \rho \frac{\partial \vec{u}}{\partial t} = \nabla \cdot \left[-pI + \mu(\nabla\vec{u} + (\nabla\vec{u})^T) - \frac{2}{3}\mu(\nabla \cdot \vec{u})I \right] \quad (2.10)$$

$$\rho(\vec{u} \cdot \nabla)\vec{u} + \rho \frac{\partial \vec{u}}{\partial t} = \nabla \cdot [-pI + \tau] \quad\quad (2.11)$$

$$\nabla \cdot (\rho\vec{u}) = 0 \quad\quad (2.12)$$

Here, ρ is the density of the incompressible fluid, $\vec{u}$ is the fluid velocity, p is the pressure, I is the identity matrix, τ is the stress tensor and μ is the viscosity of the fluid. Equation 2.12 is the mass conservation equation, which could be interpreted as,

Rate of Inflow mass = Rate of accumulation of mass in system + Rate of Outflow mass

The initial condition and boundary conditions are applied on the fluid domain. These can include conditions such as,

Initial inlet velocity condition, $\vec{u} = \vec{u_o}$

No slip boundary condition, for solid walls, $\vec{u} = 0$

Slip boundary condition for fluid interfaces, $\vec{u}.\vec{n} = 0$

Fluid flow domain is discretized up to required spatial resolution. Resolution refers to the smallest size of the grid used for the simulation. For cases involving individual bacterial model simulations, the resolution of the domain should be equal to or lower than the volume an individual cell, to correctly estimate the ambient solute concentration of the cell.

The governing Navier-Stokes and mass conservation equations are discretized. In addition to the spatial discretization, temporal discretization is also required for these equations. The temporal resolution should be determined based on the time-scale of the bacterial nutrient uptake and stability of the numerical method used. A brief description of various numerical methods is given below,

2.3.1 Finite difference method (FDM)

FDM is the simplest of discretization methods available [101]. In finite difference method (FDM) we approximate the differentials in the equations by interpreting the differentials as differences in parametric values with respect space and time. Here, the discretization is based upon the differential form of the PDE to be solved. The derivatives in the PDE are replaced with approximate difference formula based on set of weights as shown in equations for the incompressible 1-D Navier-Stoke's equation (eq. 2.13 and 2.14).

$$\frac{\partial \vec{u}}{\partial t} + \vec{u}\frac{\partial \vec{u}}{\partial x} = -\frac{\partial p}{\partial x} + \frac{1}{Re}\frac{\partial^2 u}{\partial x^2} \qquad (2.13)$$

$$\frac{u_j^{n+1} - u_j^n}{\Delta t} + u_j^n \frac{\left[u_{j+1}^n - u_{j-1}^n\right]}{2\Delta x} = - \frac{\left[p_{j+1}^n - p_{j-1}^n\right]}{2\Delta x}$$

$$+ \frac{1}{Re} \frac{\left[u_{j+1}^n - 2u_j^n + u_{j-1}^n\right]}{(\Delta x)^2} \qquad (2.14)$$

Indices j and n indicate the spatial and temporal discretized steps. The spatial parts of the equation are approximated by central difference quotients and the temporal part is discretized using forward difference quotient. These equations can be solved using appropriate numerical methods, based on the required accuracy, convergence and computational speed requirements. A few such numerical methods include, Incomplete Cholesky, Incomplete Lower-Upper factorisation (ILU), Lower-Upper Decomposition and Gauss Jordan elimination.

In the finite difference method, the quantities or variables under study are not conserved, they are estimated as pointwise functions. Therefore, FDM is restricted to use simple geometries and avoided in simulation of complex flows.

2.3.2 Finite Volume Method (FVM):

In FVM, the quantities under study are estimated as conserved entities within small volumes using volume averaged functions. The equations used in the simulations are discretized based upon an integral form of the partial differential equations such as Navier-Stokes. The grids used in FVM simulations are defined as finite control volumes encompassing the domain. The computational node of the variable, whose value is to be found, lies at the centroid of each control volume.

The conservation equations are applied to each control volume. In general, to derive the conservation equations, Gauss divergence theorem is applied to the partial differential equation 2.11. For instance, the conservative form of the 3D-Navier Stokes equation can be written as,

$$\frac{d}{dt}\int_{Vo}\rho\vec{u}dVo + \int_{Vo}\rho(\vec{u}\cdot\nabla)\vec{u}\,dVo = -\int_{Vo}\nabla p\,dVo + \int_{Vo}\nabla\boldsymbol{\tau}\,dVo \quad (2.15)$$

$$\frac{d}{dt}\int_{Vo}\rho\vec{u}dV + \int_{Sf}\overline{\rho\vec{u}}(\vec{u}.\overrightarrow{n_s})dS_f = -\int_{Sf}p\vec{n}dS_f + \int_{Sf}(\boldsymbol{\tau}.\vec{n})dS_f \quad (2.16)$$

Here, the volume (Vo) integral can be approximated over the control volume (ΔVo) and the surface (S_f) integrals can be approximated as a sum over the area of the faces A_f of the control volume as shown in equation 2.17. Where, $\vec{u}_j^n$ represents the fluid velocity $\vec{u}_j$ at time discrete time n, ρ_{fv} is density of fluid at a face of the volume and $\overrightarrow{u_{fv}}$ is the face velocity at time n.

$$\frac{d}{dt}\int_{Vo}\rho\vec{u}dVo = \rho(\vec{u}_j^{\,n+1} - \vec{u}_j^n)\,\frac{\Delta Vo}{\Delta t}$$

46

$$\int_{Sf} \overline{\rho \vec{u}}(\vec{u}.\overrightarrow{n_s})dS_f = \sum_{faces} \rho_{fv}\overrightarrow{u_{fv}}\,\overrightarrow{u_{fv}}\,A_f \qquad (2.17)$$

Due to the conservative nature of the finite volume equations, they are more stable than FDM equations for fluid flow problems in irregular grids.

2.3.3 Finite element method:

Finite element method (FEM) employs integral forms of PDE, similar to FVM. However, in FEM, piecewise representation of the solution is discretized in terms of specified basis functions. The simulation mesh used for the FEM is made up of a set of finite elements which are connected at nodes. The resulting set of non-linear algebraic equations is solved across the entire domain for approximate parameter values at these nodes [102].

3 **Mesoscopic Energy Minimization Drives** *Pseudomonas aeruginosa* **Biofilm Morphologies and Consequent Stratification of Antibiotic Activity Based on Cell Metabolism**

This chapter is based on Sheraton, M.V., Yam, J.K.H., Tan, C.H., Oh, H.S., Mancini, E., Yang, L., Rice, S.A. and Sloot, P.M.A., 2018. Mesoscopic Energy Minimization Drives *Pseudomonas aeruginosa* Biofilm Morphologies and Consequent Stratification of Antibiotic Activity Based on Cell Metabolism. Antimicrobial agents and chemotherapy, 62(5), pp.e02544-17.

Abstract

Segregation of bacteria based on their metabolic activity in biofilms plays an important role in the development of antibiotic drug

resistance. Mushroom-shaped biofilm structures, which are reported for many bacteria, exhibit topographically varying levels of multiple drug resistance from the cap of the mushroom to its stalk. Understanding the dynamics behind the formation of such structures can aid in design of drug delivery systems, antibiotics, or physical systems for removal of biofilms. We explore the development of metabolically heterogenous *Pseudomonas aeruginosa* biofilms using numerical models and laboratory knock-out experiments on wild-type and chemotaxis deficient mutants. We show that chemotactic processes dominate the transformation of slender and hemispherical structures into mushroom structures with a signature cap. Cellular Potts model simulation and experimental data provide evidence that accelerated movement of bacteria along the periphery of the biofilm, due to nutrient cues, results in the formation of mushroom structures and bacterial segregation.

Importance

Multi-drug resistance of bacteria is one of the most threatening dangers to public health. Understanding the mechanisms of the development of mushroom shaped biofilms helps to identify the multidrug resistant regions. We decoded the dynamics of the structural evolution of bacterial biofilms and the physics behind the formation of biofilm structures as well as the biological triggers that produce them. Combining in-vitro gene knock-out experiments with in-silico models shows that chemotactic motility is one of the main driving forces for the formation of stalks and caps. Our result provides physicists and biologists with a new perspective on biofilm removal and eradication strategies.

3.1 Introduction

Bacteria thrive in natural environments using two modes of growth, (i) planktonic growth by independent, single bacteria and (ii) biofilm growth, where the cells function as a group. Planktonic bacteria proliferate, infect hosts, and move without much physical interaction with other bacteria in their vicinity. They are vulnerable to antibiotics, and bacteriophages in their vicinity. In contrast, bacteria have evolved the ability to aggregate together as biofilms to protect themselves from predators and reduce the threats from antibiotics or toxic substances. Once a biofilm is established, it can host billions of bacteria that function communally. However, bacterial cells within a single biofilm exhibit different physiological states. They can be alive and active; alive and metabolically less active (dormant) or dead and decaying in different parts inside the biofilm [103, 104]. Some bacteria in biofilms are known to develop resistance to multiple antibiotic drugs [105, 106]. For example, cells present at the top or cap of mushroom shaped biofilms have been shown to be resistant to colistin [107]. Cells within or on the stalk of mushroom shaped biofilms however, have shown resistance to carbapenem and tobramycin antibiotics [108]. This suggests that it is impossible to eliminate the entire mushroom structure using a single drug. Even worse, it could lead to selective killing of non-drug resistant bacteria, leaving behind the drug-resistant strains and accelerating the spread of an infection. In a few cases, it has been shown that dormant bacteria are resistant to antibiotic treatments, therefore the segregation of bacteria into different states within the

biofilm will lead to differential drug resistance expression at different regions [109].

Recently, the World Health Organisation [110] published a list of 12 bacteria which could be of great threat to human health due to their multidrug resistance. *P. aeruginosa* has been identified as one of the bacteria of critical priority. *P. aeruginosa* is known to form mushroom shaped biofilm structures in nature and during spaceflights[111]. Cells in the interior of the mushroom-shape biofilm have low metabolic activity, while the cells near the cap of the mushroom-shape biofilm have high metabolic activity [112, 113]. They can exhibit multidrug resistance within the same mushroom structure as a consequence of these microcolonies harboring cells in different metabolic states [114]. Thus, due to the differences in physiological status among the cells within the biofilm, it is difficult to eradicate the biofilm via drug monotherapy. For example, colistin selectively kills less active cells [113, 115, 116] while tobramycin kills highly active cells in the biofilm [117, 118]. While some studies have focused on microcolony formation, the mechanisms and dynamics of micro colony formation are currently not well understood [44, 119-121]. If a mixture of two strains of *P. aeruginosa* bacteria, e.g. wild-type with motility and a non-motile mutant, are cultured together, mushroom structures are formed with the wild-type motile bacteria on the cap of the mushroom and the non-motile mutants occupying the stalk of the mushroom [44]. Modelling studies have shown that bacterial motility plays a major role in determining the shape of the biofilm structure.

Farrell et al. [122],developed a Quasi-two-dimensional force-based biofilm growth model to study the branching of biofilms consisting of non-motile bacteria. It was shown numerically that mechanical interactions between the bacteria lead to the formation of 2D finger like biofilm structures, which was previously thought to be an outcome of diffusion limitation. This observation suggests that the macroscopic biofilm structure is actively changed by microscopic interactions between individual bacteria and is not a passively evolved structure due to nutrient gradients. However, extensive studies considering interaction forces between the bacteria and nutrient limitations were unable to predict the formation of the observed complex 3D mushroom shapes [92, 122-125]. Typically, these studies predicted a series of hemispherical shapes but were not able to predict the mushroom shapes observed in nature, specifically with those involving wild-type bacteria. In this work, we report on the dynamics of biofilm shapes as they are influenced by the availability of nutrients, the distribution of motile cells and cell-cell interactions through volume and chemotactic forces. Using laboratory experiments coupled with *in silico* numerical studies, we identify the key parameters that determine the thickness and height of the stalk as well as the cap of these macroscopic structures and consequently the distribution of dormant and metabolically active bacteria. The laboratory experiments, utilizing wild-type bacteria and specific mutants, were used to quantify and validate the outcomes of the biofilm growth simulation model. We also show that chemotactic

processes dominate the transformation of slender and hemispherical structures to mushroom structures with a signature cap.

3.2   Material and method

3.2.1   Bacterial strains and growth conditions

The bacterial strains used in this study are listed in table 1. *P. aeruginosa* strains were grown at 37°C in ABT minimal medium supplemented with 5 *gl $^{-1}$* glucose (ABTG) [126]. Gentamicin (30 μg *ml $^{-1}$*) or tetracycline (50 μg *ml $^{-1}$*) was used appropriate for marker selection in *P. aeruginosa*.

3.2.2   Cultivation of biofilms in flow chambers

P. aeruginosa biofilms were cultivated in ABTG medium at 37°*C* using *40 mm x 4 mm x 1 mm* three-channel flow chambers as previously described [127]. Briefly, the bacterial strains were grown overnight in 2 ml of LB medium in 37°*C* shaking condition (200 rpm). The overnight cultures were diluted *1:100x* with ABTG and 300 *μl* of the diluted culture was injected via syringe and needle into each channel. The ABTG medium flow was halted for 1 h for bacteria incubation before resuming the flow at the rate of 4 *ml h $^{-1}$* using Cole-Parmer Masterflex® peristaltic pump (Cole-Parmer, United States) for development of biofilm. At each time-point, 3.34 *μM* SYTO9 and 20 *μM* propidium iodide (PI) stains (LIVE/DEAD™ BacLight™ Bacterial Viability Kit, Invitrogen) were injected into each channel to stain the biofilm for live and dead cell populations respectively for 15 min prior

to confocal microscopy imaging. Experiments were performed in triplicate, and the representative images were shown as results.

3.2.3 Confocal microscopy imaging

The stained-biofilm was observed under confocal laser scanning microscopy (CLSM) (LSM 780, Carl Zeiss, Germany) and images were acquired using either x20 or x40 magnification objective lens. The argon laser (488 nm) and HeNe laser (561 nm) were used to observe the green and red fluorescence respectively. The captured images were further processed using IMARIS software (Bitplane AG, Zurich, Switzerland) to generate the orthogonal view of the biofilm. Experiments were performed in triplicate, and the representative images were shown as results.

Table 3.1 Bacterial strains used in the experiments

Strains	Characteristic(s)	Reference
PAO1	Wild-type	[128]
ΔbdlA	PW3587 *bdlA*-F03::ISlacZ/hah *bdlA*-deficient strain. Tc^R	[129]
ΔCheY	*CheY*-deficient strain. Gm^R	[45]

TC^R - tetracycline resistant. Gm^R - gentamicin resistant.

3.3 Simulation model

Each bacterium in the simulation is considered as a collection of compute pixels. As the mass increases, the number of pixels for each

cell increases proportionally and the cells divide once the number of pixels have doubled. The cells' mass increment is modelled using Tessier kinetics [130]. We consider two nutrients, glucose and oxygen diffusing from the top of the simulation domain. Glucose is present in excess in both the experiments and the numerical models. Single solute Monod kinetics is the common choice in most biofilm models[98, 125, 131, 132]. This, however, would result in exponential cell growth in the simulations due to the presence of excess nutrients. Unlike single solute Monod kinetics, double solute Tessier kinetics models the bacterial mass increase in a more realistic way by establishing a nutrient consumption rate that is dependent on both limiting and excess nutrients, thereby preventing exponential cell proliferation. It has been shown in previous studies that Tessier kinetics models the growth of *P. aeruginosa* biofilms more accurately than Contois, Monod or other combined kinetics [130, 133]. We have therefore developed two substrate Tessier kinetics for modelling the biofilm growth from uptake of oxygen and glucose. Compared to previous *P. aeruginosa* biofilm simulations (25,27-29), our model based on Tessier kinetics is a more accurate predictor of the proliferation rate of bacterial cells, which is an important parameter for active to dormant cell transformations.

$$\frac{\partial S_o}{\partial t} = D_o \left(\frac{\partial^2 S_o}{\partial x^2} + \frac{\partial^2 S_o}{\partial y^2} + \frac{\partial^2 S_o}{\partial z^2} \right) - r_o(S_o, S_g, B_C) \qquad (3.1)$$

$$\frac{\partial S_g}{\partial t} = D_g \left(\frac{\partial^2 S_g}{\partial x^2} + \frac{\partial^2 S_g}{\partial y^2} + \frac{\partial^2 S_g}{\partial z^2} \right) - r_g(S_o, S_g, B_C) \qquad (3.2)$$

$$r_o(S_o, S_g, B_C) = \left(\frac{\mu \left(1 - e^{\frac{C_o}{K_o}} \right) \left(1 - e^{\frac{C_g}{K_g}} \right)}{Y_o} + m_o \right) B_c \qquad (3.3)$$

$$r_g(S_o, S_g, B_C) = \left(\frac{\mu \left(1 - e^{\frac{C_o}{K_o}} \right) \left(1 - e^{\frac{C_g}{K_g}} \right)}{Y_g} + m_g \right) B_c \qquad (3.4)$$

Equations 3.1 and 3.2 describe the time-evolution of nutrient concentrations in the simulation domain, 3.3 and 3.4 quantify the rate of nutrient consumption by the biomass. The equations are solved until steady-state is reached and the concentration at steady state is used to estimate the mass increase through Eq. 3.7. The motile bacteria can move through the domain between each time step of nutrient estimation, which is one hour. The motility of the cells is based on their energy constraint, based on the Glazier-Graner-Hogeweg model (GGH) [134, 135] given by Eq. 3.8. Motility is then dependent on the volume constraints, chemotaxis and contact adhesion between cells, substratum and media. In the absence of volume increase and chemotaxis, this motility corresponds to bacterial random walks as

observed in nature and is referred to as bacterial diffusion. The fluctuation amplitude term T_m determines the average velocity of a random walk in the simulation. The value of T_m is fixed in such a way that in the simulation the average distance moved by a cell in one hour due to bacterial diffusion falls within the average distance moved by *P. aeruginosa* bacteria on a glass slide for one hour in the experiments, which is around $145 \frac{\mu m}{h}$ [136].

S_o and S_g are the concentrations of oxygen and glucose respectively, D_o and D_g are the diffusion coefficients of oxygen and glucose respectively, μ is the cell growth rate and B_c is the biomass. The constants K, Y and m are half-saturation, yield, and metabolic coefficients respectively, with their subscripts indicating the corresponding substrates, oxygen, or glucose. The mass increase as estimated by Eq. 3.7 is translated into a corresponding target volume (V_T) increase, calculated from the mass density of the cells. The rate of volume increase or pixel addition to a cell is controlled by the change in energy shown in Eq. 3.9. In a sparsely populated space, a bacterium will be able to increase its volume faster than a bacterium in a densely packed space based on the volume constraint constant. Bacteria in tightly packed configurations however must push others towards the edge to increase their volume. Thus, the local energy interactions for pixel space allocation will result in an overall change in the structure of the biofilm. This energy interaction also prevents a cell from growing when there is no space to place the additional biomass, thus

avoiding unrealistic cell proliferation. Therefore, the increase in biofilm biomass is controlled by nutrient consumption kinetics and by structural energy constraints within the biofilm.

$$\frac{\partial B_{co}}{\partial t} = Y_o \left(r_o \left(S_o, S_g, B_C \right) - m_o B_C \right) \tag{3.5}$$

$$\frac{\partial B_{cg}}{\partial t} = Y_g \left(r_g \left(S_o, S_g, B_C \right) - m_g B_C \right) \tag{3.6}$$

$$\frac{\partial B_c}{\partial t} = \begin{cases} \dfrac{\partial B_{co}}{\partial t} \;, \dfrac{\partial B_{co}}{\partial t} < \dfrac{\partial B_{cg}}{\partial t} \\[4mm] \dfrac{\partial B_{cg}}{\partial t} \;, \dfrac{\partial B_{co}}{\partial t} \geq \dfrac{\partial B_{cg}}{\partial t} \end{cases} \tag{3.7}$$

B_{co} and B_{cg} are the biomass contribution from oxygen and glucose uptake, respectively.

$$P\left(\sigma(\vec{\imath}) \to \sigma(\vec{\imath'}) \right) = \begin{cases} \left[exp\left(-\dfrac{\Delta H}{T_m} \right) \right], & \Delta H > 0 \\[3mm] 1 \;, & \Delta H \leq 0 \end{cases} \tag{3.8}$$

$$\Delta E_v = \lambda (V_{cell} - V_T)^2 \tag{3.9}$$

$$\Delta E_c = \sum_{i,j} Con(\tau_{\sigma(i)}, \tau_{\sigma(j)}) \left(1 - \delta_{\sigma(i),\sigma(j)} \right) \tag{3.10}$$

The probability of a pixel copy [137] is calculated in Eq. 3.8, $\sigma(i)$ is the pixel occupied by the cell, V_{cell} is the volume of the cell and λ is the volume potential. Equation 3.10 describes the contact adhesion energy between the cells of different types τ, at positions i and j, where δ is the Kronecker delta function and $Con(\tau_{\sigma(i)}, \tau_{\sigma(j)})$ is the contact adhesion parameter. In the simulation, it is assumed that the cells are more adherent to the substratum than to each other, meaning less local energy change for adhering to the surface. The energy changes due to adhesion ΔE_C and volume change ΔE_V are combined to evaluate the total energy change, $\Delta H = \Delta E_V + \Delta E_C$.

Table 3.2 Summary of the values of different parameters used in the Tessier kinetics model simulations

Parameter	Value	Unit
Domain size	150 x 150 x 150	μm
Initial mass of bacteria [131], B_C	1.315×10^{-13}	g
Initial volume of bacteria [131], V	27	μm^3
No. of initial bacteria	5	cells
Half-saturation coefficient of glucose [130], K_g	26.9	$g\ m^{-3}$
Half-saturation coefficient of oxygen [130], K_o	1.18	$g\ m^{-3}$
Boundary layer thickness [131], B_{LT}	16.5	μm

Diffusion coefficient of glucose, D_g	2.52 x 10^{-6}	$m^2\ h^{-1}$
Diffusion coefficient of oxygen, D_o	7.2 x 10^{-6}	$m^2\ h^{-1}$
Maintenance coefficient for glucose (26), m_g	0.0078	$g\ g_b^{-1}h^{-1}$
Maintenance coefficient for oxygen (26), m_o	0.014	$g\ g_b^{-1}h^{-1}$
Specific growth rate (27), μ_{max}	0.29	h^{-1}
Yield coefficient of oxygen (26), Y_o	0.635	
Yield coefficient of glucose (26),Y_g	0.628	
Chemotaxis potential, $\lambda_{chem,fix}$	400	
Fluctuation amplitude term, T_m	40	
Initial glucose concentration, S_g	400	$g\ m^{-3}$
Initial oxygen concentration, S_o	8	$g\ m^{-3}$

3.4   Results and discussions

The simulations were carried out for 50 simulation hours. The change in structure of the biofilm with time is summarized in fig. 3.1 During the initial 20 h, the biofilm spreads itself across the surface because of the minimal energy change through bacteria-substratum contact. Later, when the nutrient concentration availability falls below the metabolic requirement of bacteria, the bacteria become dormant, indicated by light blue color in the simulation. Dormant bacteria in their natural habitat generally are confined to their space without movement.

In a similar way, dormant bacteria in the simulation lose their motility and their consumption rate becomes negligible. These processes add an extra layer to the growth segregation zone, the bottommost, no-growth dormant zone. Therefore, as time progresses the zones vary in thickness and, as expected, the final shape of the biofilm after 50 h was hemispherical. The preservation of segregation zones during the entirety of the growth process, is due to the moving diffusion boundary layer and the increasing nutrient consumption rate at the dense lower layers. Most models in the literature, including the forced based model [122], predict finger projection formation in 2D and simulate a hemisphere shape as shown in fig. 3.1, rather than the mushroom shape observed in laboratory experiments with wild-type *P. aeruginosa* PAO1 biofilms (fig. 3.2a). This indicates that some key mechanisms are missing, and the current model is not capable of simulating the dynamics of mushroom-shape formation. We performed experiments with *ΔbdlA,* a *P. aeruginosa* dispersion mutant. We characterized the structures with clearly distinguishable stalks and caps, at least 70 μm tall, as mushroom-shaped biofilms. *ΔbdlA* mutants produce mushroom shapes as shown in fig. 3.2b, suggesting that the ability of bacteria to leave the biofilm through active dispersal does not influence the formation of these mushroom shapes and that the formation is inherent in all wild-type *P. aeruginosa* bacteria irrespective of favourable or detrimental environmental cues.
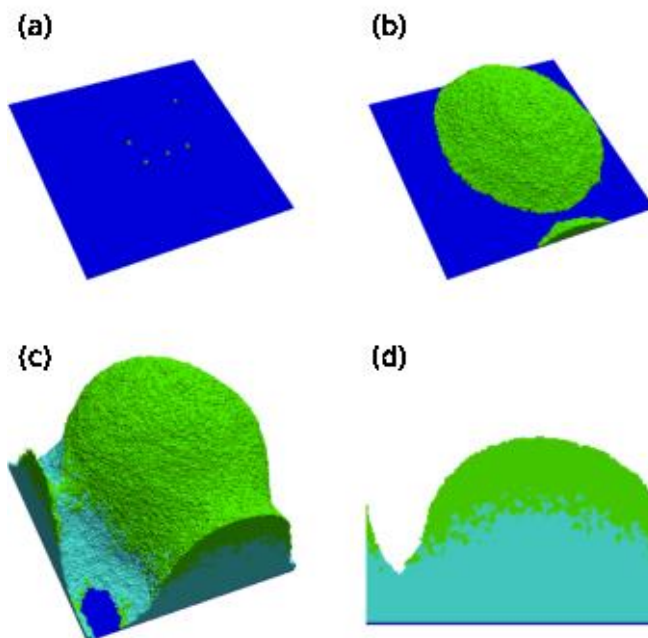
Figure. 3.1 Simulated biofilm growth without chemotaxis. 3D views of the progress of biofilm development at (a) 10 h, (b) 30 h, (c) 50 h and 2D x-z cross section at (d) 50 h. The green color indicates active cells and the light blue indicates dormant cells.

As shown in fig. 3.2, *bdlA* is not required for mushroom formation. Therefore, we carried out experiments using *ΔCheY*, a chemotaxis mutant. These mutant lacks chemotactic motility, the motility associated with the directional movement of bacteria towards a nutrient presence. The biofilms produced by this *ΔCheY* mutant did not produce mushroom structures and instead formed large stalks without caps (fig. 3.2c). This indicates a link between mushroom structure and chemotactic motility. The simulation model was modified accordingly to include bacterial chemotaxis. This chemotactic

parameter was subsequently included as an energy term, ΔE coupled with the already existing contact adhesion and volume constraint energy as, $\Delta H = \Delta E_V + \Delta E_C + \Delta E$. The chemotactic energy potential satisfies three conditions,

If the critical chemotaxis concentration is zero then the change in energy potential should be zero,

$$C_{sat} \to 0, \Delta E \to 0 \tag{3.11}$$

This condition biologically corresponds to the solute which does not evoke chemotaxis in cells, ergo critical chemotaxis concentration is zero.

For solute concentrations below the critical concentrations C_{sat}, the change in energy potential should be negative and chemotaxis should depend on the magnitude of the gradient in concentration.

$$C_{sat} > S_o\left(\vec{i'}\right), \Delta E < 0 \tag{3.12}$$

If the critical concentration is very high, then the change in energy potential should be minimum, which sets the cell to be always in motion along the gradient field with the minimum chemotaxis potential, $\lambda_{chem}\left(S_o\left(\vec{i}\right) - S_o\left(\vec{i'}\right)\right)$.

$$C_{sat} \to \infty, \Delta E \to min \tag{3.13}$$

$$\Delta E = \lambda_{chem} \left[\frac{S_o\left(\vec{i}\right)}{1 + \dfrac{S_o\left(\vec{i}\right)}{C_{sat}}} - \frac{S_o\left(\vec{i'}\right)}{1 + \dfrac{S_o\left(\vec{i'}\right)}{C_{sat}}} \right]$$
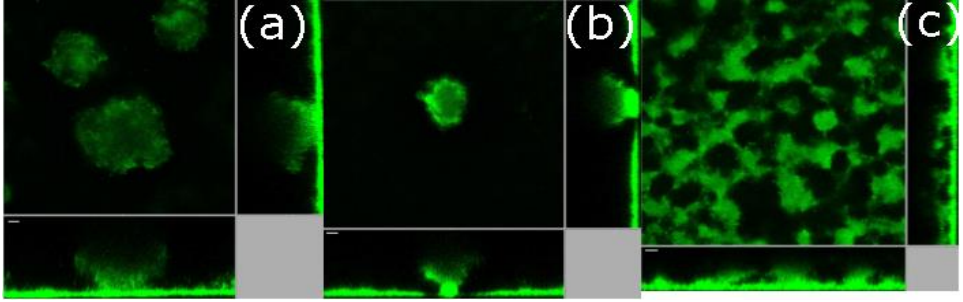
<div align="right">(3.14)</div>

Figure. 3.2 Confocal images for different strains of *P. aeruginosa* biofilms after 3 d, (a) wild-type, PAO1, (b) dispersion mutant, *ΔbdlA* and (c) a chemotaxis mutant, *ΔCheY.* The scale bars are 20 μm.

Equation 14 satisfies all three chemotaxis conditions and is used in the model to implement chemotaxis based on oxygen concentration. As mentioned, an increase in volume of a cell in the simulation is modeled by increase in the number of pixels associated with the cell. The newly added pixels of a growing cell are placed in such a way that the local change in energy is minimized. Placing the new pixels along the oxygen gradient, decreases the chemotactic energy and consequently the local energy change. Thus, favoring the cell growth along the nutrient gradient. It is expected that the bacteria in the biofilm will grow or move towards the nutrient enriched zone to sustain activity and biofilm growth. In the simulations, the motility is now a function of

contact adhesion, volume constraint and chemotaxis. Simulations with this new model with modified chemotaxis constraint produce mushroom shapes (fig 3.2a - c). The potential, λ_{chem}, determines the "chemotaxis velocity", the velocity at which the bacteria move along the nutrient gradient. Higher chemotaxis velocity therefore thins out the stalk of the mushroom.
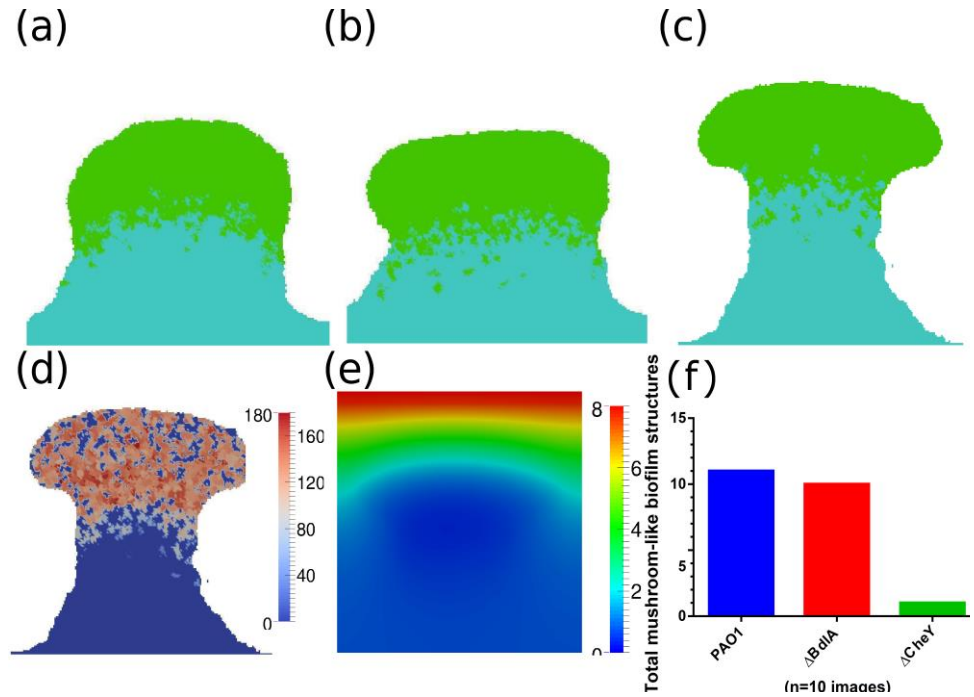

Figure. 3.3 Simulated biofilm growth with modified chemotaxis. 2D section views of the progress of biofilm development after 50h at different λ_{chem} values (a) $0.75 \, \lambda_{chem,fix}$, (b) $\lambda_{chem,fix}$ and (c) $1.25 \, \lambda_{chem,fix}$. The green color indicates active cells and the light blue indicates dormant cells. The bottom panel shows the distribution of (d) oxygen concentration (e) cell motility in the model simulation with λ_{chem} =

λ$_{chem,fix}$ and (f) Estimate of mushroom-shaped biofilm structures produced by different strains used in the experiments.

The change of the height of the biofilm and the number of live cells with time is shown in fig. 3.4a. During the early stages of biofilm growth (20-30 h), the rate of height increase is significantly lower than the proliferation rate. This is due to the biofilm spreading across the substratum and covering a larger area, as was also observed in experimental data for day 1 biofilm (fig. 3.4d). After 35 h, the height of the biofilm increases at a faster rate to accommodate for the increase in total biomass. At the later stages of biofilm growth, even though the proliferation rate decreases, the height of biofilm increases exponentially. The critical point in time (35 h) after which the height increases exponentially is when the stalk of the mushroom starts to grow rapidly and a clear distinction between the cap and stalk appears. This critical point can be better estimated using the change in surface to volume ratio shown in fig. 3.4b. After 35 h, the critical point, the surface area of the biofilm increases rapidly leading to the formation of a broad cap at the top of mushroom. The spatial distribution of oxygen and the motility are shown in fig. 3.3d and e respectively. The cells at the bottom, which proliferate must find a new space which is energetically favorable. The energetically favorable outcome for the cell is to move along the increasing nutrient gradient. In this GGH model with cell-cell adhesion energy, a cell in a crowded environment needs to expend more energy to push the nearby cells to move in its intended direction, than a cell in a sparsely populated environment. Due

to this inherent density-controlled cell motility, the model favors the mobility of cells in the periphery of the biofilm.
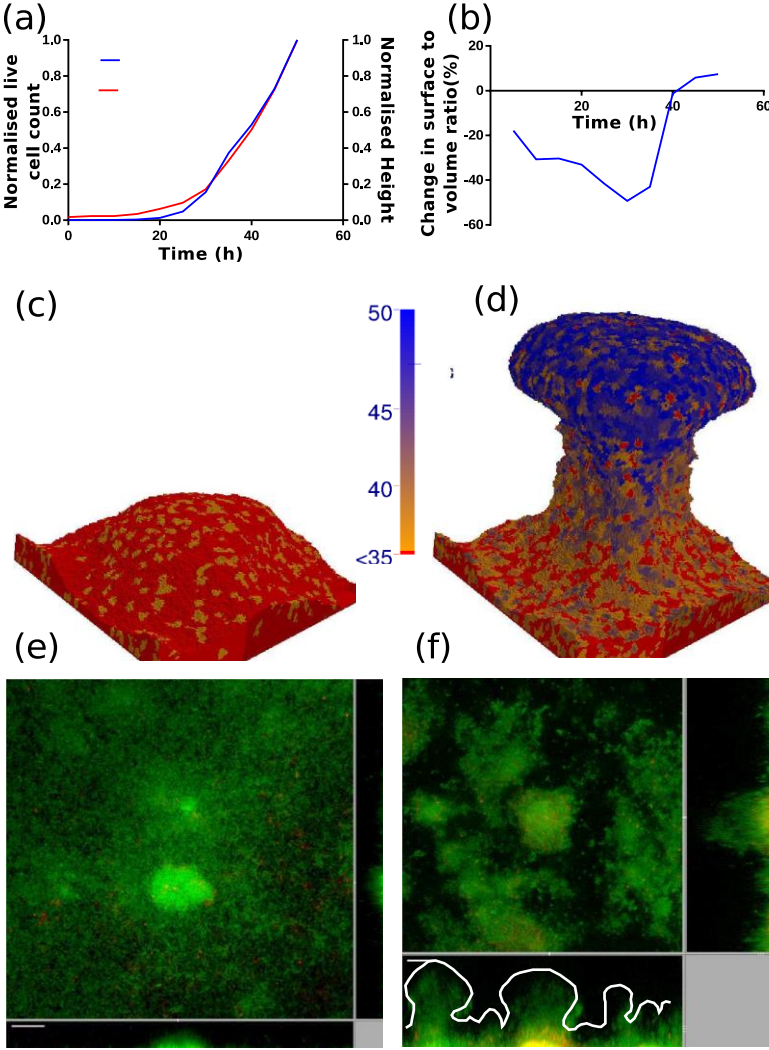

Figure. 3.4 (a) Change of biofilm height and cell count with time; (b) Change in surface to volume ratio of the biofilm with time. Simulation results showing the creation-time of the bacterial cells at different layers within the biofilm, the legend denotes the time of cell creation,

(c) at 35 h and (d) 50 h. Panels e and f show the formation of mushroom structure of PAO1 wild-type biofilm after (e) 1 d and (f) 3 d. Green color indicates live cells, red color indicates dead cells and the white curve is a trace line on the outer surface of the biofilm.

Movement along the periphery of the microcolony is motion along the path of least resistance to minimize the local energy and consequently, the global energy. As the cells in the periphery start to move upwards, the central width of the biofilm begins to thin, and the stalk starts to form in the middle (fig. 3.4b). The mature cells, colored red, are found to climb over the relatively new cells at the stalk and periphery guided by the chemotaxis gradient. Once the chemotaxis potential has been maximized the motile cells start to aggregate into a crown at the top of the biofilm, in other words the cells have reached the region where oxygen is available for survival. This process continues, and a clear distinction appears between the cap and the stalk part of the mushroom shape.

The model simulations without chemotaxis (fig. 3.1) and the experiments using chemotaxis deficient mutant $\Delta CheY$ (fig. 3.2c) did not produce any significant number of mushroom shaped structures as shown in fig. 3.3f. This clearly shows that chemotaxis is one of the key mechanisms in determining the shape of the biofilm. The formed structures in $\Delta CheY$ biofilms closely resemble the hemispherical shape formed by the contact and volume constraint version of the model. Segregation of bacteria within the biofilm based on their metabolic activity is conclusive from the model. In the simulations, three unique zones are observable in the formed mushroom structure,

- The dormant bottom layers
- Nutrient limited layers of the stalk
- Fast proliferating cells at the cap of mushroom

The bacteria in these three unique zones show differential responses to antibiotics. As such, the entire biofilm becomes highly heterogenous over time similar to the observations made by Williamson et al [138]. Therefore, eradication of the biofilm through clinical or chemical treatments is not straightforward due to the varying levels of antibiotic resistance at different layers of the biofilm. This antibiotic resistance could arise due to the physiological heterogeneity [138] of the cells or the accumulation of genetic mutations based on the local stresses acting on the cells [139]. Removing the cap and stalk of the mushroom will expose the dormant cells to fresh nutrient supply. This would help them revert to metabolically active state. In diseases such as cystic fibrosis involving *P. aeruginosa* biofilms, the reversion of dormant bacteria to an active state could result in exacerbations resulting in acute infections [140]. Our model can help understand the time-evolution of biofilm structure in *P. aeruginosa* biofilms and along with it the spatial distribution of antibiotic drug resistance. The model can be used to estimate antibiotic penetration and oxygen limitations, which have been shown [141] as contributors of antibiotic tolerance in *P. aeruginosa* biofilms. Using model simulations to estimate the parameters, which could otherwise be hard or impossible to measure experimentally, will aid a clinician to understand the inherent heterogeneity and provide valuable decision-making insights in

selection of antibiotics. Additional development of the current model for other bacteria and inclusion of drug induced cell lysis mechanisms can establish the model as a predictor of clinical efficacy of antibiotics.

3.4.1 Acknowledgements

4 Convection and matrix dictate inter- and intra-biofilm quorum sensing communication

This chapter is based on Tan C.H. †, Oh H.S. †, Sheraton M.V. †, Mancini E., Chye1 J.L.S., Kjelleberg S., Sloot P.M.A., and Rice S.A. The Impact of Mass Transfer and Quorum Quenching on Quorum Sensing Behaviors, submitted to Science Advances.

ABSTRACT

While the molecular mechanisms and impact of quorum sensing (QS) at the population level are well studied, it is unclear how QS functions in species-rich, matrix-encased communities. Here, we explore the impact of quorum quenching (QQ) activity on QS signalling in spatially organised biofilms in scenarios that mimic the open systems of natural and engineered environments. Using a functionally differentiated biofilm system and numerical modelling, we show that the extracellular matrix, local flow and QQ interact to modulate communication. In a biofilm, the matrix restricts QS and QQ to the site of production, and QQ impacts QS as a function of spatial distribution and organization. For aqueous environments, signals are rapidly disseminated by convection and received by distant responders via

matrix-trapping. This process enables signalling between biofilms even when the overall extracellular signal level is below the activation threshold. Using this model, we tested the potential impact of QQ on QS responses and show that QQ enzymes degrade signals as a function of the local hydrodynamics, rather than spatial localization, in water-saturated conditions. The predictions from the mathematical model were experimentally validated, supporting the application of in-silico models for the design of laboratory experiments. We further show that intracellular QQ activity does not influence the QS function of surrounding organisms, as previously suggested. Our studies highlight that convection facilitates inter-biofilm communication in the environment while the extracellular matrix further dictates the transport of the competing QS and QQ molecules within biofilms, leading to heterogenous QS behaviour in multispecies biofilm communities.

4.1   Introduction

Quorum sensing (QS) is a microbial communication system that relies on the production, secretion and perception of small diffusible signalling molecules. This system has evolved to control social behaviours that influence the fitness of microbial populations [142, 143]. The genetics and the regulatory pathways of many QS systems are well documented and the means by which such cooperative traits are protected from exploitation by QS cheaters have also begun to be described [144-147]. However, despite our understanding of QS gained from studying individual, planktonic model organisms in the laboratory, we have very limited information on how QS is achieved in

spatially organised, microbial communities in natural and engineered environments. Although QS has been implicated in the formation of complex, mixed species granular biofilms and sludge biocakes in bioreactor ecosystems [148, 149], QS signals in the liquid phase frequently occur at concentrations that are significantly lower than the typical QS thresholds (i.e., ~ 500 pM) recorded for planktonic cultures [149]. Hence, it is unclear how distinct biofilm communities may communicate via QS signals and achieve QS regulatory control at such low extracellular concentrations. Furthermore, the levels of QS signals can be influenced by quorum quenchers (QQ) that coexist with the QS signal producers in the community, impeding the formation of granular biofilms [150]. Given the high frequencies of co-occurrence of QS and QQ organisms in nature [151, 152], the interplay between the QS and QQ activities is likely to have profound impacts on the behavior of biofilm communities. Thus, while QS organisms are prevalent, it remains to be determined how the QS process varies according to the dynamics of cellular activities and the community composition in any specific environment.

Within biofilms, microorganisms often grow as highly structured cell clusters encased in an extracellular matrix of polymeric substances (EPS)[149, 153-155]. The EPS matrix thus serves not only as a protective structure enabling biofilm cells to survive, but it can also partition different populations or communities within the environment [156]. In monospecies cultures, biofilm thickness and the abundance of the EPS matrix have been associated with the ability of the biofilm to

retain signals for QS induction under flow conditions [157], and the EPS components have been shown to influence communication between aggregates of biofilm populations [158-161]. However, little is known about how the extracellular matrix impacts QS signalling in microbial consortia with communal interactions (i.e., QS vs. QQ), and how spatial distribution and organization of individual competing populations, as segregated by the EPS matrix, may determine the outcome of communication within the biofilm communities.

To address this knowledge gap, we have developed an experimental system to mimic QS processes reflective of open systems of naturally occurring biofilms that have functionally distinct community members [149, 155]. In this biofilm model, each bacterial population was encapsulated within a microliter-scale hydrogel granule and grown into a biofilm aggregate. By patterning these engineered aggregates onto an agar surface, we defined how the spatial organization of functionally distinct organisms impacts the interaggregate communication in different ecological contexts, including the presence and absence of local flow, using both experimental and numerical models.

4.2 Results

4.2.1 Designing a microbial biofilm system for QS study

An experimental biofilm model comprised of individual populations of QS signal producers, responders and quenchers was

assembled to study the impact of the extracellular matrix, hydrodynamics and signal interference on QS signaling at a macroscale level (i.e., centimeters) (fig. 4.1). To minimise confounding variables that potentially arise from interactions between different bacterial species, we engineered the QS and QQ functions into different populations of *Escherichia coli* (Appendix Table S1). The signal producer was an *E. coli* strain harboring a pTrcHis2 plasmid with an acyl-homoserine lactone (AHL) signal synthase, *esaI*, derived from *Pantoea stewartii*[150]*,* while the signal quencher strain encoded *aiiO*, an AHL acylase from *Ochrobactrum anthropi*[162]. Both *esaI* and *aiiO* genes were fused to a P_{trc} promoter, and constitutively expressed in all experimental conditions (data not shown). EsaI synthesizes *N*-(3-oxohexanoyl)-L-homoserine lactone (3OC6-HSL) while AiiO degrades a wide spectrum of AHLs, including 3OC6-HSL [162, 163]. *E. coli* JB525 is a signal reporter strain that is unable to produce AHLs, but senses them with high sensitivity (e.g., 3OC6-HSL at 1 nM) and expresses the green fluorescent protein (GFP) in a signal concentration-dependent manner [164]. To simulate densely packed biofilm aggregates, such as those found in aerobic granules in wastewater treatment systems (fig. 4.1a), individual bacterial strains were encapsulated using alginate polymers to produce aggregates of cells (i.e., granules) with an average dimension of 1.91±0.06 mm (fig. 4.1b and Appendix fig. 4.1). Bacterial microcolonies, similar to microbial clusters found in naturally occurring biofilms [165, 166], were formed within the alginate matrix after 24 h incubation at room temperature

77

(fig. 4.1c). Using these strain-defined alginate aggregates (defined as producers, responders and quenchers), we built a microbial biofilm system on the surface of an agarose hydrogel (1% w/v) where the spatial coordinates of each aggregate population were defined along the grid (fig. 4.1d). Unless otherwise stated, bacterial aggregates were placed at a distance of 1 cm apart from one another (in coordination x and y). Nutrients for growth were supplied in an agarose hydrogel (1% w/v), representing the extracellular matrix, or in a liquid medium, characteristic of the open systems of aqueous environments (fig. 4.1f). The biofilm was cultured in a dark-chamber, and signalling (activation of the QS reporters, i.e., QS activation) was visualised under UV illumination using a camera equipped with a GFP emission filter (fig. 4.1e). This setup thus provided a platform to study how species interact based on diffusible molecules, such as AHLs and QQ enzymes, in natural communities.
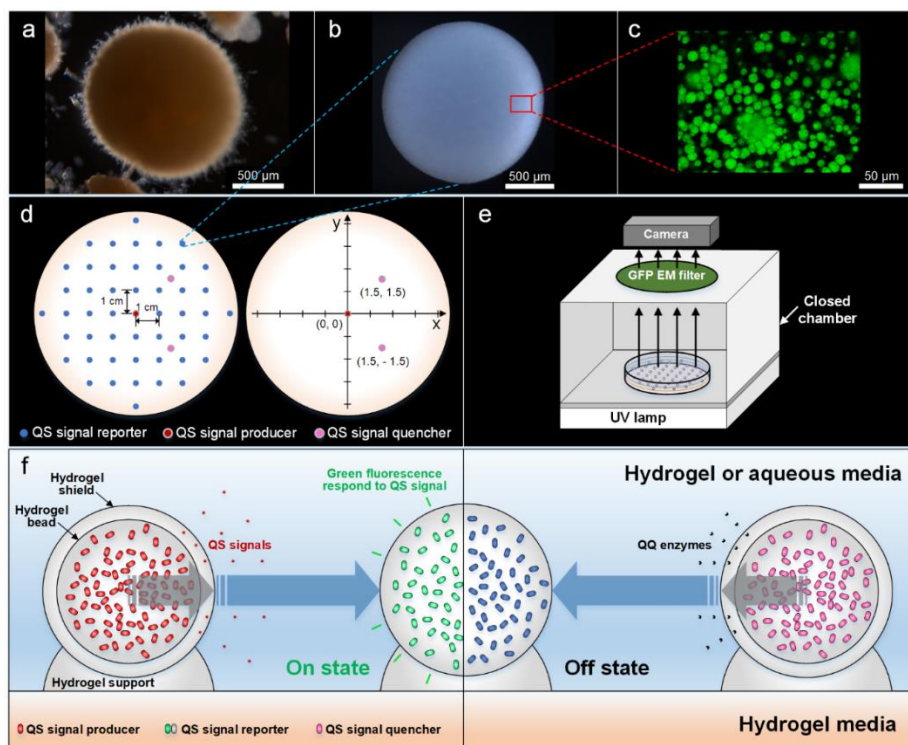
Figure. 4.1 Experimental configuration. a, Natural biofilm aggregate – a highly structured, multispecies microbial community in wastewater treatment plant/bioreactor. Scale bar: 500 μm. **b,** Synthetic biofilm aggregate – a biofilm model engineered by encapsulating individual strains into an alginate-based hydrogel granule. Scale bar: 500 μm. **c,** Microcolonies of QS signal reporter strain developed within an alginate-based hydrogel granule after incubating for 24 h at room temperature. The reporter aggregate was exposed to 100 nM of QS signal (i.e., 3OC6-HSL) for 4 h for GFP induction prior to imaging by confocal laser scanning microscope at 488/510 nm. Scale bar: 50 μm. **d,** Layout of a microbial biofilm system comprised of individual biofilm aggregates of QS signal reporters (blue), producers (red) and quenchers (pink) on a 9 cm petri dish. **e,** The setup for time series snapshots of signalling events in the experimental system. The GFP fluorescence, representing QS

activation, is visualised under UV illumination using a camera equipped with a GFP emission filter in an enclosed chamber. **f,** An illustration of the cross-sectional view of a microbial biofilm system setup on a 9 cm petri dish. The biofilm aggregates were crosslinked onto an agarose hydrogel layer (1% w/v) and overlaid with 10% lysogeny broth (w/v), with or without 1% agarose (w/v) supplementation, to represent the hydrogel matrix or the aqueous environment, respectively. Both QS signal producer (red) and quencher (pink) aggregates were protected with an additional layer of alginate (i.e., hydrogel shield) to prevent cell leakage. QS signals and QQ enzymes are expected to be released from the respective source of biofilm aggregates into extracellular space to activate the QS signal reporters (green – on state) or to inhibit reporter activation (blue – off state) by degrading the QS signals. The image for the natural biofilm aggregate (a) is adapted from Tan *et al.* [149].

4.2.2   QS signalling in a hydrogel matrix

To simulate QS signalling in natural biofilms such as microbial mats, where the organisms appear to be embedded in continuous patches of extracellular matrix, we used 1% agarose hydrogel (w/v) as the biofilm matrix of the microbial system (fig. 4.2). In this experiment, AHLs were secreted from two spatially separated, actively growing signal-producing aggregates located at positions (1, 1) and (0, -2) (fig. 4.2a). Activation of the surrounding reporter populations was uniform and symmetric. Individual reporter aggregates were sequentially activated, where the signal acquisition time for each reporter increased with their distance from the AHL producer, which is a reflection of signal concentration and diffusion rates. To elucidate the mechanism responsible for this pattern of induction, we developed a three-

dimensional (3D) *in silico* model that integrated simple AHL diffusion with the dynamic signal production rate according to the logistic growth of the AHL producer, abiotic signal degradation rate, as well as cooperative activation behaviour of the reporter (fig. 4.2b, Appendix fig. 2 and *see* Mathematical Model). The model predicted the spatiotemporal changes in signal profiles, showing localised AHL accumulation around the producer (fig. 4.2c) as well as limited signal diffusion away from the producer within biofilms. Diffusivity of the AHL was the only free parameter in this model and was tuned using experimental reporter granule activation results (data not shown). Based on the simulations, the diffusivity of AHL (D_{AHL}) in the hydrogel matrix was determined to be 4.75×10^{-6} cm^2/s (fig. 4.2d), which is close to the estimated diffusivity of AHL in water, 4.9×10^{-6} cm^2/s, reported previously [167]. The average relative error of mismatch in the QS activation time between the experiment and numerical simulations was approximately 6%, and the Fréchet distance showed a maximum mismatch of 3.5 h (fig. 4.2e), indicating a good match between the experiment and the simulations.
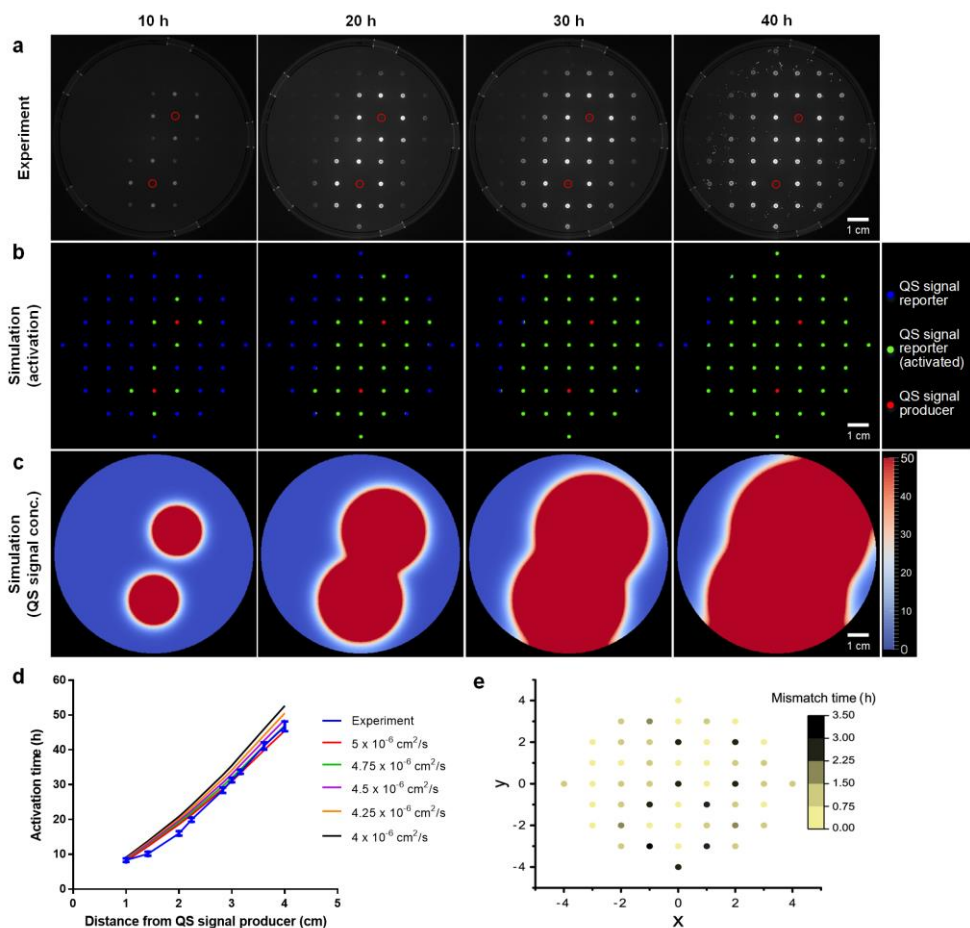
Figure. 4.2 QS signalling in a hydrogel matrix. a, Activation of QS signal reporter aggregates, i.e., GFP induction, in response to signals generated by QS signal producer aggregates (open red circles) located at (1, 1) and (0, -2). **b,** Simulations of QS activation based on the signal diffusivity (D_{AHL}) of 4.75×10^{-6} cm^2/s. Blue and green circles indicate uninduced and QS-activated states of reporter aggregates, respectively. Red circles indicate QS signal producer aggregates. **c,** Spatio-temporal prediction for the QS signal concentration profile based on the signal diffusivity of 4.75×10^{-6} cm^2/s. The colour scale: 0-50 nM. **d,** Simulations of spatio-temporal QS responses based on

different QS signal diffusivities. Means ± SD are presented (n = 3) for the experiment. **e,** The mismatch of QS activation times for the experimental results and the simulations with a signal diffusivity of 4.75×10^{-6} cm^2/s. The colour scale: 0-3.5 h.

4.2.3 QS signalling in a hydrogel matrix in the presence of quorum quenchers

To determine the impact of physical distribution of quorum quenchers on QS signalling in the biofilm context, two signal-quenching aggregates were placed in proximity to (-0.5, -0.5), or at a distance away from (1.5, 1.5), the signal producer (0, 0) (fig. 4.3). Both quenchers exhibited localised QQ effects but differed in their impact on QS activation, depending on the relative position of the respective quencher to the signal producer (fig. 4.3a). For the quencher positioned at a greater distance from the signal producer (1.5, 1.5), signal inactivation was seen for the granules positioned to the left and right as well as behind the QQ strain (fig. 4.3a). In contrast, QS inhibition was only observed for the granules behind the QQ strain, where the QQ is between the producer and sensor granule, when in close proximity to the QS producing strain (fig. 4.3a). Thus, the QQ effectively creates a 'shadow' effect, blocking QS activation based on diffusion of the signal around the QQ strain.

AiiO has been reported to be a cytoplasmic QQ enzyme in the original host *O. anthropi* [168], and it was therefore assumed here that the AiiO remained as an intracellular protein when it is expressed heterogeneously in *E. coli*. Additionally, the production rate of AiiO was expected to be similar to that of EsaI since both enzymes were

synthesised using the same expression system. We therefore performed simulations assuming that no AiiO was released outside the quencher aggregates and that quenching of AHL occurred based on diffusion of the AHL into the quencher aggregates where they are degraded by AiiO in the cells. These simulations suggested that all reporter populations were activated after a certain period of time despite the presence of quenchers. Thus, the effect of QQ was predicted to be negligible, even when adjacent to the quencher aggregates (Appendix fig. 4.3). Since the experimental data showed QS inhibition, these results suggested that QQ activity was not limited to the intracellular/intra-aggregate process and that the enzymes may be released into the extracellular/extra-aggregate space. We subsequently confirmed the presence of extracellular QQ activity outside the quencher aggregate after incubating the aggregate in the growth medium for 6 h or more (Appendix fig. 4.4a and b). The release of AiiO corresponded to the detection of the intracellular enzyme alkaline phosphatase extracellularly, suggesting that AiiO might be released via cell lysis by a small subpopulation of cells (Appendix fig. 4.4c). The incorporation of these findings into our existing model enabled an improved and more accurate simulation of the experimental observations of reporter activation with an average relative error of mismatch of approximately 6.5% (fig. 4.3b, Appendix fig. 4.5 and *see* Mathematical Model).
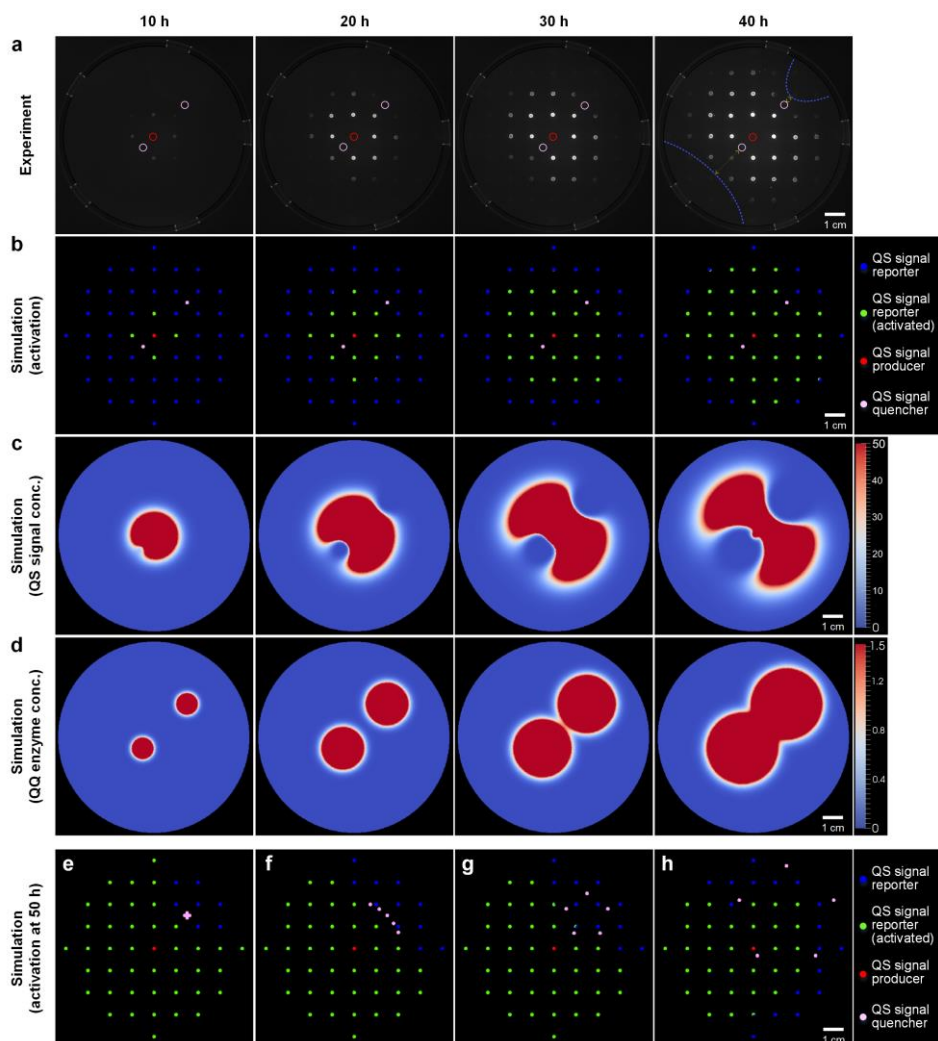
Figure. 4.3 QS signalling in a hydrogel matrix in the presence of quorum quenchers. **a,** Activation of QS signal reporter aggregates, i.e., GFP induction, in response to signals generated by QS signal producer aggregate (open red circles) located at (0, 0) with the presence of QS signal quencher aggregates (open pink circles) located at (1.5, 1.5) and (-0.5, -0.5). Blue dashed line indicates the zone of QS inactivation. **b,** Simulations of QS activation. Blue and green circles indicate uninduced and QS-activated states of reporter aggregates,

respectively. Red and pink circles indicate QS signal producer and quencher aggregates, respectively. **c,** Spatio-temporal prediction for the QS signal concentration profile. The colour scale: 0-50 nM. **d,** Spatio-temporal prediction for the QQ enzyme concentration profile. The colour scale: 0-1.5 nM. The diffusivities of QS signals (D_{AHL}), i.e., 4.75×10^{-6} cm^2/s and QQ enzymes (D_{AiiO}), i.e., 1.35×10^{-6} cm^2/s were used in all simulations. **e-h**, Simulation of QS signalling in a hydrogel matrix in the presence of quorum quenchers with different spatial configurations. Specifically, the QS signal quencher aggregates positioned with a geometric centre at (1.5, 1.5) and vertices spaced equally from this centre as **e,** concentrated, **f,** arc, **g,** small pentagon and **h,** large pentagon configurations. Blue and green circles indicate uninduced and QS-activated states of reporter aggregates, respectively. Red and pink circles indicate QS signal producer and quencher aggregates, respectively.

The model was tuned for two free parameters, diffusivity of *AiiO* and amount of *AiiO* released by cell lysis (K_{leak}) using experimental reporter granule activation results (data not shown). The diffusivity of AiiO (D_{AiiO}) in the hydrogel matrix was determined to be 1.35×10^{-6} cm^2/s, which is approximately 3.6 times slower than the diffusivity of the AHL. Correspondingly, the model predicted minimal AiiO transport in the hydrogel matrix and hence allowed the build-up of the released enzyme around the quencher aggregate over time (fig. 4.3d). As a consequence, AHL concentrations around the quencher aggregate were predicted by the simulations to be significantly reduced compared to other regions (fig. 4.3c), though it might still sufficient to allow QS activation depending on the relative distance to the signal producer (fig 4.3a and b). Our numerical model further predicted that

dispersed QQ populations would have a greater impact on QS behaviour compared to the highly clustered QQ populations (fig. 4.3e-h). For example, 14% of the responder populations were inactive with the clustered QQ populations (fig. 4.3e) while up to 35% of the responders, depending on specific configurations, were inactive when the QQ populations were dispersed throughout the system (fig. 4.3f-h).

4.2.4   QS signalling in an aqueous environment

In contrast to the highly organised, symmetrical QS activation pattern observed in the hydrogel matrix (fig. 4.2a), activation of QS in the aqueous environment was random and uneven (fig. 4.4a). The reporter populations were activated independent of their distance from the signal producer. The activation process often occurred unidirectionally, initiating from one edge of the plate with activation proceeding away from that edge until all of the reporter populations were activated. The entire reporter population could be fully activated by a single signal producer in 15.5 h (i.e., with a 6 h interval from the time the first aggregate was activated until all of the reporter aggregates were fully induced), while this might take more than 50 h in the hydrogel matrix model and setup (Appendix figs. 6 and 7).
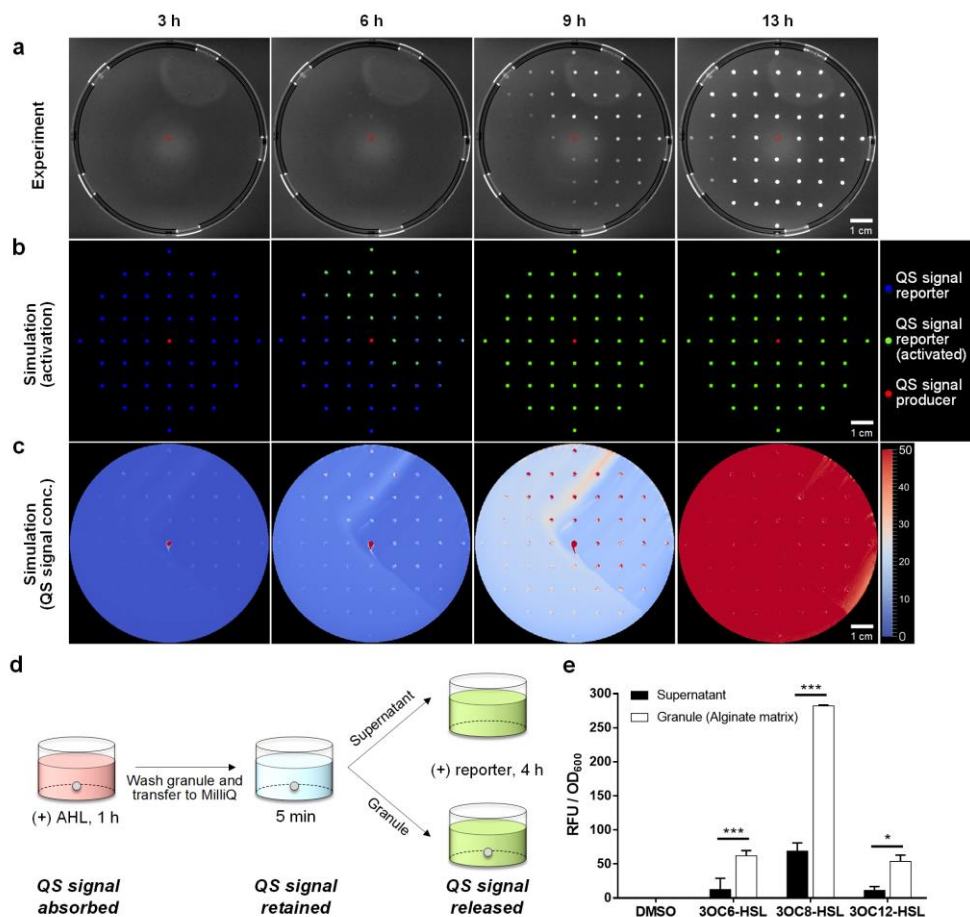
Figure. 4.4 QS signalling in an aqueous environment. a, Activation of QS signal reporter aggregates, i.e., GFP induction, in response to signals generated by QS signal producer aggregate (open red circles) located at (0, 0). **b,** Simulations of QS activation based on the Navier-Stokes model for fluid convection. Blue and green circles indicate uninduced and QS-activated states of reporter aggregates, respectively. Red circles indicate QS signal producer aggregates. **c,** Spatio-temporal prediction for the QS signal concentration profile. The colour scale: 0-50 nM. **d,** Experimental design to test for QS signal absorption, retention and release by extracellular matrix (e.g.,

88

alginate granule). **e,** GFP induction in the QS reporter strain by QS signals, including 3OC6-HSL, 3OC8-HSL and 3OC12-HSL, released from supernatant or alginate granule. DMSO was used as a solvent control. Relative fluorescent intensity was determined at 488/510 nm and normalized by OD_{600} for each sample. Means ± SD are presented (n = 3). Multiple *t*-tests with corrections using the Holm-Sidak method were performed to compare the QS signal retention by the alginate matrix to the supernatant, where significant differences are indicated as follows: * *P* < 0.01, ****P* < 0.001.

Given the discrepancy in the QS activation times, the hydrogel based mathematical model was not able to reproduce the rapid QS induction profile in the aqueous environment, even if the signal production rate was increased 100 fold (Appendix fig. 8). For example, a 100 fold increase in the signal production rate only reduced the time to full QS activation by 18 h (i.e., from 52 h to 34 h). Thus, it was clear that the irregular and rapid QS activation in the aqueous environment could not be simply driven by diffusion but involves other modes of signal transport, including convection. The presence of a local flow in the enclosed incubation chamber was verified by a drift assay (Appendix fig. 9a). When the petri dish was covered with a lid, the local flow was prevented but evaporation-induced convection remained (Appendix Fig. 9b). Correspondingly, the rate of QS activation was reduced remarkably in the closed system (Appendix fig. 10c) compared to the open lid experiments. For example, 88% of the responder populations were activated within 10 h in the open aqueous system (i.e., without lid) compared to only 37% in the closed aqueous

system (i.e., with lid) and 8% in the open hydrogel system (i.e., without lid) (Appendix fig. 10). By incorporating a convection term, as a means of local flow and evaporation induction, to the hydrogel-based model, we simulated the experimental observations in the aqueous environment with velocity being the only free, tuneable parameter and found that an x-velocity of 0.1 cm/s and y-velocity of 0.2 cm/s qualitatively best reproduced the QS pattern (fig. 4.4b and *see* Mathematical Model). Although it was not possible to precisely simulate the spatial QS activation profile in the experimental data, the simulations predicted similar activation times of 13.5 h for the entire system, with a 5 h interval from the time of activation for the first aggregate until all were induced, indicating a close match of the experiments and the simulations.

The simulations subsequently predicted non-circular or asymmetrical signal concentration contours in the aqueous environment (fig. 4.4c). The signal accumulation was estimated to occur rapidly and the entire system could reach a uniform minimum concentration of 50 nM in 13 h. Interestingly, many signal hot spots, where significantly higher signal concentration was anticipated to accumulate than in the immediate surroundings, were found across the system for the early time points (i.e., < 9 h). The majority of these hot spots overlapped with the positions of the reporter aggregates, which were encapsulated in the alginate matrix, indicating that the signals may preferentially accumulate in, or are retained by, the matrix. Based on these outcomes, we further hypothesised that the biofilm matrix

90

(e.g., alginate) may absorb AHLs from the aqueous environment to achieve a higher AHL concentration in the granule over time to enable reporter activation within the matrix. To verify this hypothesis, we exposed alginate granules without bacteria to different AHL solutions, including 3OC6-HSL, 3OC8-HSL and 3OC12-HSL for 1 h (fig. 4.4d). After a brief washing, the alginate granules were added to a reporter assay to represent the matrix sample while the 'washout' was taken as the supernatant. In all cases, the reporter strain was activated by signals released from the alginate matrix and the level of activation was significantly higher than that of the supernatant (i.e., > 5 fold, $P < 0.05$ for all) (fig. 4.4e), demonstrating the reversible binding of signals into the biofilm matrix. This outcome underscores a crucial role of biofilm matrix in QS signalling in aqueous environments.
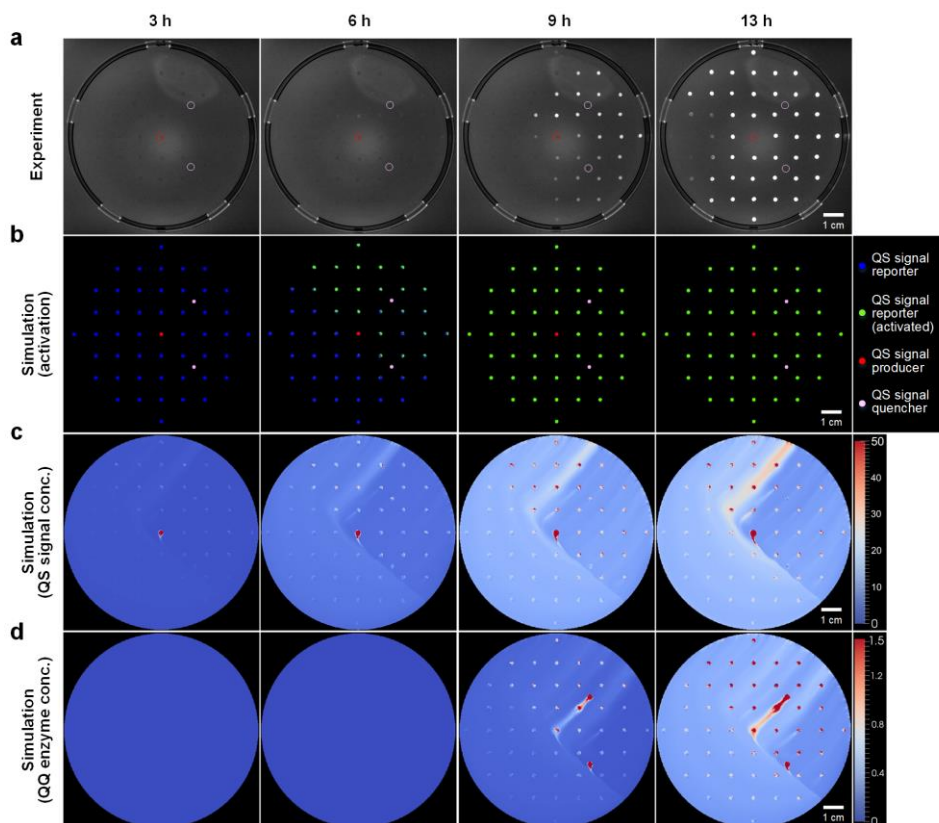
Figure. 4.5 QS signalling in an aqueous environment in the presence of quorum quenchers. a, Activation of QS signal reporter aggregates, i.e., GFP induction, in response to signals generated by QS signal producer aggregate (open red circles) located at (0, 0) with the presence of QS signal quenchers aggregates (open pink circles) located at (1.5, 1.5) and (1.5, -1.5). **b,** Simulations of QS activation based on the on the Navier-Stokes model for fluid convection. Blue and green circles indicate uninduced and QS-activated states of reporter aggregates, respectively. Red circles indicate QS signal producer aggregates. **c,** Spatio-temporal prediction for the QS signal concentration profile. The colour scale: 0-50 nM. **d,** Spatio-temporal prediction for the QQ enzyme concentration profile. The colour scale: 0-1.5 nM.

4.2.5 QS signalling in an aqueous environment in the presence of quorum quenchers

Unlike the case for the hydrogel matrix (fig. 4.3a and Appendix fig. 11), the addition of two signal-quenching aggregates at positions (1.5, 1.5) and (1.5, -1.5) in the aqueous environment did not alter the QS activation profile, with the exception of a limited number of reporter aggregates that remained partially inactive after 13 h incubation (fig. 4.5a). Such experimental observations were also predicted by the simulations (fig. 4.5b and *see* Mathematical Model). While the presence of QQ aggregates had little impact on the pattern of QS activation experimentally (fig. 4.5a vs. 4.4a), the simulations suggested that the quenchers could strongly suppress the accumulation of high concentrations of signal (i.e., >10 nM) (fig. 4.5c vs. 4.4c). For example, in the absence of quenchers, the entire system was saturated with signals with a minimum concentration of 50 nM by 13 h (fig. 4.4c), while in the presence of quenchers, the average signal concentration was predicted to be less than 15 nM by 13 h (fig. 4.5c). Thus, in an aqueous environment, it is likely that QQ can cause more global but varying impacts on the QS responses, depending on the QS activation thresholds of the responders, than in a biofilm context.

Extracellular matrix, hydrodynamics and QQ dictate the pattern of QS signalling. To quantitatively measure the impacts of the extracellular matrix, hydrodynamics and QQ on QS signalling, we compared the cumulative QS responses of reporter populations in

different environments. In these experiments, the spatial coordinates of individual populations in each system were standardised (fig. 4.1d). The activation time for each experimental condition was normalised by subtracting the time taken for the first reporter aggregate to be activated and the subsequent time for activation of the reporter populations in the system (fig. 4.6). In the hydrogel matrix, the normalised time for activating the first 50% of the reporter populations was almost identical for experiments with and without the quenchers (fig. 4.6a). However, the time for activation of 90% of the reporters, in the presence of quenchers, was significantly longer compared to when the quenchers were absent (i.e., with a mean difference varied from 4 h to 18 h). The experimental variability, as indicated by the 95% confidence interval based on three independent studies, was minimal with or without the quenchers. In contrast, in the aqueous environment, quenchers appeared to have a strong influence on the reproducibility of the experiment in terms of activation time (fig. 4.6b). While the experimental variation in the absence of quenchers was negligible, there was high variability in QS activation when the quenchers were present. The difference in mean activation time between experiments with and without quenchers increased from less than 30 min to more than 6 h as the percentage of activated reporters increased from 15% to 90%. These findings were consistent with the prediction of AHL profiles in both scenarios (fig. 4.4c and 5c), indicating a reduced, but global QQ impact on QS. Importantly, in the absence of quenchers, full QS activation in the aqueous environment could be achieved at least 10

times faster than that in the hydrogel matrix (fig. 4.6). Even with the presence of quenchers, the duration required to arrive at more than 90% of signal responder populations activated was approximately five times shorter than that in the hydrogel matrix, highlighting the extent by which the interaction with the physical environment may influence QS behaviour.
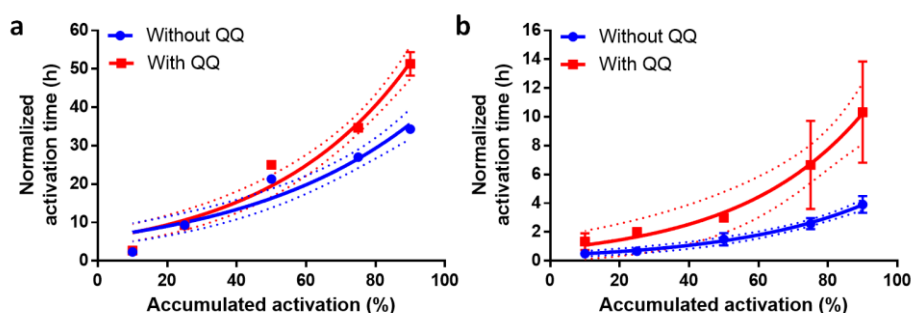
Figure. 4.6 Extracellular matrix, hydrodynamics and QQ dictate the pattern of QS signalling. Cumulative QS responses of the signal reporters embedded within **a,** a hydrogel matrix and **b,** an aqueous environment, determined in the absence (blue circles) or the presence of signal quenchers (i.e., QQ - red squares) according to the experimental system layout shown in fig. 4.1d. The QS activation time was normalised by subtracting the time taken for the first reporter aggregate to be activated and the subsequent time spent for cumulative activation of the reporters in the system. Means ± SD are presented (n = 3). The dotted lines represent the 95% confidence intervals.

4.3 Discussion

The spatiotemporal activity of QS signaling and QQ is strongly influenced by the mode of mass transport and/or the biogeography and organization of individual populations in the biofilm system. First, monospecies biofilm studies have indicated the ability of biofilms to retain AHLs at concentrations 1,000 fold higher than in the liquid phase [169] and the biofilm thickness can affect the levels of QS induction under flow conditions [157]. Here, we further show that the EPS matrix of the biofilm governs molecular transport (e.g., QS signals and QQ enzymes) via diffusion mechanisms, resulting in distinct zones of QS signalling and QQ inhibition (figs. 4.2 and 4.3). These findings clearly support the hypothesis that QS would be most pronounced in the vicinity of QS organism/population clusters within biofilms [36, 170]. Since the production of EPS matrix in many organisms is directly regulated by QS [171-173], one might speculate that AHL-EPS synthesis/secretion has co-evolved to facilitate cooperative QS behaviour to immediate neighbours for population benefits and evolutionary stability of QS, according to the kin selection hypothesis [174, 175]. Similarly, QQ activity would be concentrated within biofilms and thus compete with QS signalling. It is important to note, however, that although the QQ function is localised within the biofilm matrix, the impact of QQ on the QS behaviour may vary according to the spatial organization and distribution of different species. Specifically, we found that dispersed QQ populations have greater influence on the QS behaviour compared to the QQ populations present

in clusters (fig. 4.3e-h). Also, it was noted that a QQ population in close proximity to a QS signal source may not necessarily affect the QS behaviour in the immediate vicinity but it may otherwise influence those at a further distance (fig. 4.3a-b and h). These observations are likely due to the differences in production rate and diffusivity of the molecules. Hence, these findings strongly suggest that heterogenous QS may be an emergent property of multispecies biofilm communities.

In contrast, in an aqueous environment the transport of molecules was mainly driven by convection, including the local flow and evaporation-induced advection [176]. Although convection at high velocity (e.g., 1 cm/s), for example in the flow cell system, has been shown to dilute signals and deter QS induction [157], we demonstrated here that convection at low velocity (i.e., < 0.1 cm/s) mediates rapid AHL and AiiO dissemination and allows for their activity, in a relatively open environment. For example, in the absence of quenchers, full QS activation in an aqueous environment could be accomplished at least ten times faster than that in the extracellular matrix (fig. 4.6). Under these conditions, it was not possible to establish local gradients of QS signals or QQ enzymes and there was little or no heterogeneity in the QS response of the system (figs. 4.4a and 5a). In fact, QQ had a limited effect on the QS behaviour measured here with a low activation threshold of 1.5 nM. Nonetheless, a reduced but global QQ effect on QS signalling was predicted (fig. 4.4c vs. 4.5c) and may therefore affect QS behaviours that rely on higher activation thresholds. These QS signalling and signal-quenching interactions could be particularly

relevant in environments where significant hydraulic retention time (HRT, i.e., water retention time) is expected, including water pockets in the rhizosphere [177], on wetted leaves [178], in sequencing batch bioreactors [149], in wastewater treatment plants [165] or even in the animal gastrointestinal tract [179]. For example, a previous study comparing the quorum size of *Pseudomonas syringae* on dried and wetted leaves, indicated that the total population on the wetted leaves displayed at least 25% more QS activity compared to that of the dried condition after 48 h of incubation [178], suggesting that liquid/convection-mediated transport enables interaggregate communication. It is also likely that convection plays a critical role in mediating signal transduction in engineered ecosystems, such as in granular bioreactors where the suspended biofilm aggregates are constantly mixed by aeration, allowing signal exchange to occur between individual granules in the liquid medium [149]. The observation that the EPS matrix absorbs signals from the environment (fig. 4.4e) provides a mechanistic insight into how biofilm aggregates effectively perform QS, even at extremely low signal concentrations (i.e., ~500 pM) in a continuous suspended condition [149].

The experimental and modelling data show that QQ activity, in the hydrogel matrix, must be an extracellular/extra-aggregate process to deliver any significant impact on QS. This raises an important ecological question regarding the role of QQ in nature, as the majority of QQ isolates from different environments exhibit intracellular or cell-associated QQ activity, which is presumed to result from a lack of a

signal peptide for secretion [180, 181]. Without secretion of the QQ enzyme, the cellular uptake and degradation of the environmental AHL by the QQ organism is probably too limited to compete with the signal production rates by other species. Therefore, our data suggest that the intracellular QQ enzymes may not have evolved primarily to degrade environmental AHL signals as a competition measure as previously proposed [182], at least not in habitats where the movement of QQ organisms is bound by the extracellular matrix. Instead, it is likely that the intracellular QQ enzymes have evolved to control other important cellular processes; for example, regulating QS signal level in the AHL producers [183]. Alternatively, for QQ to evolve as a competitive advantage, high production rates of QQ enzymes are needed to counter the much higher population densities of co-occurring QS producing organisms. We observed extracellular QQ, which was also associated with the extracellular activity of alkaline phosphatase, an intracellular enzyme [184]. This suggests that cell lysis plays an important role in localised QQ activity, and could be achieved by a subpopulation of cells undergoing lysis, as was observed for extracellular DNA (eDNA) release in *P. aeruginosa* [185].

In summary, our data provide a quantitative assessment of QS in biofilms and reveal that the pattern of QS signalling is primarily governed by the physics of mass transport. In a diffusion limited environment, afforded by the extracellular matrix, both QS signalling and QQ function are restrained to close neighboring cells, and the impact of QQ on QS behaviour is highly dependent on the species

localization. By contrast, the operational range of QS signalling and QQ activity is greatly enhanced by the local flow as well as the binding affinity of signals or quenching enzymes to the EPS matrix. Importantly, these findings have strong implications for how other extracellular metabolites behave in the environment and explain complex spatiotemporal patterns of cellular or social activities in mixed species communities.

4.4 Methods

4.4.1 Engineering of biofilm aggregates using alginate polymers

Sodium alginate solution was prepared by autoclaving 1.3% w/v sodium alginate (Thermo Fisher Scientific, Singapore). Overnight cultures, i.e., QS signal producer (*E. coli* EsaI), quencher (*E. coli* AiiO) and reporter (*E. coli* JB525), were washed three times with MilliQ water. Thirty microliters of each bacterial culture were mixed with 970 µl of sodium alginate solution (1.3% w/v) to reach a final OD_{600} of 0.25. Approximately 4 µl of alginate-bacteria suspension were dripped, via a syringe needle (26G), into a sterile $CaCl_2$ (4% w/v) (Merck, Singapore) solution to crosslink the alginate polymers. The Ca-alginate-bacteria aggregates, with an average diameter of 1.92±0.04 mm, were formed in $CaCl_2$ solution after incubation for 20 min and washed twice with MilliQ water (Appendix fig. 1a). To prevent any leakage of QS signal producers or quenchers, the alginate aggregates of QS signal producers or quenchers were coated with an additional layer of Ca-alginate with a thickness ranging from 0.03-0.07 mm (Appendix fig. 1b). These Ca-alginate-bacteria aggregates were

allowed to grow into biofilm aggregates in nutrient media as described below.

Arraying bacterial aggregates into a microbial biofilm system. The Ca-alginate-bacteria aggregates were arrayed onto a 9 cm petri dish, containing 1% w/v agarose hydrogel (with a thickness of 2.5 mm) to construct a biofilm system, using the Ca-alginate gelation method. Briefly, 1 µl of sodium alginate solution (1.3% w/v) was dropped evenly onto the agarose hydrogel according to the grid at an interval of 1 cm. The Ca-alginate-bacteria aggregates were placed onto the sodium alginate drops and 3 µl of $CaCl_2$ (4% w/v) solution were added to each aggregate to allow crosslink formation between aggregates and the agarose for 10 min. Twenty millilitres of 10% w/v lysogeny broth (Lennox, Difco, Singapore), with or without 1% w/v agarose supplementation, were overlaid onto the plate to represent the hydrogel matrix or the aqueous environment, respectively. $CaCl_2$ (0.095% w/v) was supplemented to each medium to prevent swelling of Ca-alginate aggregates during the experiment.

4.4.2   Imaging and image processing

The plate containing the microbial biofilm system was placed inside a Gel-Doc XR+ system (Bio-Rad Laboratories, Singapore). UV fluorescent images were captured every 15 min with 20 s exposure for the aqueous environment experiment using a GFP emission (520/530 nm) filter. The exposure time was reduced to 5 s for the hydrogel matrix experiment to minimise the background fluorescence, which was

observed to increase linearly with time. The raw data were exported as 1392- by 1040- pixel (91.2 x 91.2 μm pixel size) 16-bit TIFF images for image analysis (Appendix fig. 12). To quantify the fluorescence intensity for each reporter aggregate, we first created a binary template image by localizing every reporter aggregate to a new layer using the 'Pencil Tool' (size 20 px) of Photoshop software (Adobe, USA). The template image was used to determine the mean grey value of each reporter aggregate using the 'Analyse Particles' command of ImageJ (version 1.48, National Institute of Health, USA). After normalising the mean grey value of each reporter aggregate by deducting the background fluorescence over time, the fluorescence intensity of each aggregate relative to a fully QS-activated aggregate (i.e., the relative fluorescence intensity) was determined. The overall shape of synthetic aggregate and microcolonies of QS signal reporter strain developed within the synthetic aggregate was visualised using Stereomicroscope (Stereo Discovery V8, Zeiss, Singapore) and confocal laser scanning microscope (LSM 780, Zeiss, Singapore), respectively.

4.4.3 Determination of QS activation thresholds in experiments and simulations

The thresholds of AHL concentration and incubation duration required for QS activation (i.e., GFP detection) in simulations were determined by wet-lab experiments. The experimental setup described above using a 9 cm petri dish was adapted to a 24 well microtiter plate (id. 15.6 mm). A single reporter aggregate was fixed onto an agarose surface (1% w/v with 2.5 mm in height), at the centre of the well, using

the Ca-alginate gelation method. Six hundred microliters of nutrient medium (10% w/v lysogeny broth + 0.095% CaCl2) supplemented with varying concentrations of synthetic AHL (i.e., 3OC6-HSL; ranging from 0 to 50 nM) were added to the well as a hydrogel (+1% w/v agarose) or an aqueous overlay. Fluorescent images were captured at 20 s exposure time and quantified as described above. The relative fluorescence intensity of reporter aggregates exposed to different concentrations of AHL were plotted against the incubation time (data not shown). Based on the curves, the thresholds of AHL concentration and incubation duration required for GFP expression (i.e., time delay, t_{delay}, for QS activation) were determined to be 1.5 nM and 4 h, respectively, for both hydrogel matrix and aqueous environment simulations. For the analysis of experimental results, 60% of relative fluorescence intensity was determined as the threshold for QS activation in the aqueous environment based on the same curves. It was adjusted to 5% of relative fluorescence intensity for the analysis of results from hydrogel matrix experiments, in which the fluorescent images were captured at shorter UV exposure time (5 s).

4.4.4   Numerical model

We modeled the transport of QS signals (i.e., AHL) and QQ enzymes (i.e., AiiO) using advection-diffusion-reaction equations. Equation 4.1 describes the change in concentration of AHL with time. The first term describes the diffusion of the molecules (Fick's law). The diffusivity of AHL, D_{AHL}, varies spatially depending on whether AHL is present in an aqueous or a hydrogel medium. The second term

103

represents the production rate of AHL by the signal-producing aggregates, which is described as functions of time. The parameters of these functions were fitted to the experimental data describing the actual production of AHL by isolated signal-producing aggregates. The third and fourth terms describe the degradation rate of AHL due to interaction with AiiO and the abiotic degradation rates, respectively. The degradation rate of AHL by QQ activity ($r_{AHL,QQ}$) is described by a Michaelis-Menten reaction (Equation 4.1a) and the abiotic degradation of AHL ($r_{AHL,deg}$) follows simple first order degradation kinetics (Equation 4.1b). The final term represents the advection of AHL in an aqueous solution. In Equation 4.1, the only free parameter is D_{AHL}. The key parameters used in the model are listed in Table 4.1. The simulations are carried out in two different phases, (i) data tuning, which is used to find the values of the free parameter(s) in the model and (ii) model validation, where the value obtained from the data tuning is used in simulating different spatial setups of QS and/or QQ granules and the results are validated.

Equation 4.2 describes the transport of AiiO. The equation is similar to Equation 4.1 except for the absence of the degradation due to the interaction with AHL. Since AiiO catalytically degrades AHL, they are not consumed in the AHL degradation process and are only subject to abiotic degradation. We derived the production rate of AiiO (r_{AiiO}) from r_{AHL} by assuming that the production rate of AiiO and EsaI (i.e., AHL synthase) is equal since both enzymes were expressed using the same promoter system (i.e., P_{trc}) and their molecular weights are

similar (Equation 4.2a). β represents the maximum production rate of AHL by a mole of AHL synthase, based on literature values[186]. By assuming that the intracellular AiiO is released from the quencher aggregates only when the cells lyse, the final production rate of AiiO from a quencher aggregate was determined by the concentration of AiiO and K_{leak}, the first order rate constant. In addition, the leakage of AiiO was determined to be zero for the first 6 h due to the time delay for cell lysis (Appendix fig. 4a), which is also observed in experiments as shown in Appendix fig. 4a and b. D_{AiiO} and K_{leak} were treated as free parameters in the model. Both free parameters were optimized simultaneously with the experimental data (Appendix fig. 13).

Equation 4.3 is the incompressible Navier-Stokes equation for the aqueous medium, so it applies only to experiments simulating the aqueous environment (where I is the identity matrix, p is the pressure and ρ is the density and μ is the viscosity of the fluid). Equation 4.3 is used to obtain the steady state velocity vectors ($\vec{u}$), which are later used in Equation 4.1 for solving the advection term. When solving Equation 4.3, four different boundary conditions were implemented (Appendix fig. 14).

- No slip boundary condition – at the walls of the petri dish plate and at the interfaces with aggregates and agarose layer;
- Sliding wall boundary condition – at the air-liquid interface at half of the upper aqueous layer, with $\vec{u}_w$ and $\vec{n}$ being the wall velocity and the normal vector respectively;
- Slip boundary condition – at the air-liquid interface at the other half of the upper aqueous layer;

- Pressure point constraint – at one point at the bottom of the dish.

$$\frac{\partial C_{AHL}}{\partial t} = D_{AHL}\nabla^2 C_{AHL} + r_{AHL} - r_{AHL,QQ} - r_{AHL,deg} + \nabla.(\vec{u}\, C_{AHL}) \quad (4.1)$$

$$r_{AHL,QQ} = \frac{k_{cat}\, C_{AiiO}}{K_m + C_{AHL}} C_{AHL} \qquad (4.1a)$$

$$r_{AHL,deg} = k_{deg,AHL} C_{AHL} \qquad (4.1b)$$

$$\frac{\partial C_{AiiO}}{\partial t} = D_{AiiO}\nabla^2 C_{AiiO} + r_{AiiO} - r_{AiiO,deg} + \nabla.(\vec{u}C_{AiiO}) \qquad (4.2)$$

$$r_{AiiO} = K_{leak}C_{AiiO} = K_{leak}\frac{r_{AHL}}{\beta}, (\, r_{AiiO} = 0\,, \qquad 0 < t < 6\,h\,) \,(4.2a)$$

$$r_{AiiO,deg} = k_{deg,AiiO} C_{AiiO} \qquad (4.2b)$$

$$\rho(\vec{u}\cdot\nabla)\vec{u} = [-\nabla p + \mu(\nabla^2\vec{u})] \qquad (4.3)$$

$$\nabla \cdot \vec{u} = 0 \qquad (4.3a)$$

No slip boundary,

$$\vec{u} = 0 \qquad (4.3b)$$

Sliding wall boundary,

$$\vec{u} = \vec{u}_{w,proj} \qquad (4.3c)$$

$$\vec{u}_{w,proj} = (\vec{u}_w - (\vec{u}_w \cdot \vec{n})\,\vec{n}) \cdot |\vec{u}_w| \,/\, |\vec{u}_w - (\vec{u}_w \cdot \vec{n})\,\vec{n}| \quad (4.3d)$$

Slip boundary,

$$\vec{u} \cdot \vec{n} = 0 \qquad (4.3e)$$

Pressure point constraint,

$$p = 0 \qquad (4.3f)$$

$$\delta_{activation}(C_{AHL}, t) =$$

$$\begin{cases} 0, & C_{AHL} < C_{AHL}^* \\ 1, & C_{AHL} \geq C_{AHL}^*, \ continously \ for \ t_{delay} \end{cases} (4.4)$$

To solve Equations 4.1 and 4.2 we use FiPy, a python (version 2.7) based finite volume solver. The advection-diffusion-reaction of AHL is modelled using Equation 4.1 and solved using FiPy. The equation is solved on a cylindrical mesh generated using GMSH (version 3.0). In a similar fashion, the change in concentration of AiiO is modelled using Equation 4.2. Both the Equations 4.1 and 4.2 are coupled and solved to estimate the spatiotemporal variation of the concentration levels of AHL and AiiO. If the concentration of AHL in an inactive aggregate was greater than a certain threshold value, C_{AHL}^*, continuously for t_{delay} (the time delay for GFP expression), then the aggregate was considered to be active and expressing GFP (Equation 4.4). The thresholds of AHL concentration (i.e., 1.5 nM) and the time delay (i.e., t_{delay}: 4 h) for GFP expression (i.e., QS activation) were determined as described above.

For simulation of fluid dynamics, we use a commercial fluid dynamic solver, COMSOL Multiphysics (version 4.4). A single-phase fluid (water) was simulated assuming the top half of the aqueous layer to be dragged by air in the vicinity, thus setting the other half layer in motion as shown in Appendix fig. 15. Finally, we use CompuCell-3D (CC3D 3.7.5) for visualization purposes.

Table 4.1 Model parameter definitions

Parameter	Definition (value)	Source
D_{AHL}	diffusivity of QS signal (4.75×10^{-6} cm^2/s)	free parameter
D_{AiiO}	diffusivity of QQ enzyme (1.35×10^{-6} cm^2/s)	free parameter
k_{cat}	catalytic rate constant (22.68 1/s)	[187]
K_m	Michaelis constant (2.95 mM)	[187]
$k_{deg,AHL}$	0.005545 1/h	[188]
$k_{deg,AiiO}$	0.005545 1/h	assumed to be equal to $k_{deg,AHL}$
q_{leak}	fraction released from the granule out of the total QQ enzymes produced (0.011)	free parameter
$q_{turnover}$	proportional amount of QS signal synthase produced with respect to the QS signal production rate (1.1 mol AHL/mol AHL synthase)	[186]
C_{QS}^*	minimum concentration of QS signal to activate granule (1.5 nM)	calibration experiment
t_{delay}	delay time for GFP expression (4 h)	calibration experiment

4.5 QS signal absorption, retention and release by extracellular matrix

Alginate granules without bacterial cells were prepared as described above. The alginate granules were exposed to AHLs at final concentrations ranging from 100 nM to 1,000 nM for 1 h at room temperature. After brief washing in PBS for 5 min, the alginate granules were added to a reporter assay, i.e. JB525, to represent the matrix sample while the 'washout' was taken as the supernatant. DMSO was used as a solvent control. Relative fluorescent intensity was determined at 488/510 nm and normalised by OD600 for each sample using a microplate reader (Tecan Infinite M200pro, Switzerland). The experiment was repeated three times.

4.6 Statistical analysis

All statistical analyses were performed using Prism (GraphPad version 6). Multiple t-tests with corrections using the Holm-Sidak method were performed to compare the QS signal retention by the alginate matrix to the supernatant. The significance levels for the family of comparisons were set at 5%. The corrected P values were reported. Data in all figures show means $\pm$ SD (n = 3 to 6, biological replicates).

4.7 Acknowledgements

4.8 Author contributions

5 Prediction and Quantification of Bacterial Biofilm Detachment Using Glazier-Graner-Hogeweg Method Based Model Simulations

This chapter is based on Sheraton M.V., Melnikov V and Sloot P. M. A Prediction and Quantification of Bacterial Biofilm Detachment Using Glazier Graner Hogeweg Method Based Model Simulations. Submitted to Journal of Theoretical Biology.

Abstract

Morphological changes in bacterial biofilm structures arise from the fluid-structure interactions between the biofilm and the surrounding fluid. Depending on the magnitude of the force acting on the structure, the bacteria rearrange to attain an equilibrium shape or get washed away by the moving fluid. Understanding the dynamics behind the evolution of such equilibrium or failed states can aid in development of tools for biofilm removal or eradication. We develop a Glazier-Graner-Hogeweg method-based model to explore the collective evolution of biofilm morphology arising from cell-cell and cell-fluid interactions. We show that low adherence and high motility of the cells

lead to sloughing of biofilms and streamers form under laminar flow conditions in tightly packed biofilms. Also, in mixed species biofilms, we found that a species with less cell-cell binding affinity gets eroded faster than its counterpart. Therefore, we hypothesize that in nature these less adherent species should be present encapsulated within the biofilm structure to maximize their chances of survival.

5.1   Introduction

Biological cell-cell interactions have been modelled using agent-based models[189, 190] since they can handle individual attributes of the cells and simulate the evolution of a larger system which encompasses these cells. Frameworks such as NetLogo [191], FLAME [192, 193] and MASON [194] offer a wide range of tools to develop agent-based models. These frameworks can handle a wide range of problems in economics, socio-political and geographical domains, which require and agent-based approach. However, to handle individual biological cells in the model, along with their associated physical characteristics such as cell shape, intercellular adhesion and cell signaling, a robust biophysics-based model is required. iDYnomics [195], an individual Based Model framework (iBM), is one such biophysics-based model, which simulates cells as hard spheres with an adhesion potential serving as a mechanical link between these cells. The adhesion potential varies as a function of the distance between the cells. iDYnomics was developed with primary focus on simulating bacterial communities and their associated surroundings. Jayathilake et al. [196] developed   a   flexible   iBM   model   based   on   Large-scale

Atomic/Molecular Massively Parallel Simulator (LAMMPS) to simulate the adhesion between the cells using springs and dashpot model. The major drawback of using the above iBM based models for simulating bacterial communities is the absence of proper mechanisms to incorporate the dynamics associated with cell shape variations, topographical cell stacking[197], and the consequent effects associated with cell-cell interactions. Glazier-Graner-Hogeweg model (GGH) [98] eliminates these shortcomings by implementing energy-based evolution of cell shapes [198, 199]. In addition, the energy-based approach restricts the evolution of physically unrealistic scenarios which would otherwise arise in other simplistic approaches [195, 196], which assume cells to be a fixed solid geometry such a sphere. The proliferation of cells in GGH is also indirectly governed by the energy minimization principle, thus preventing artificial growth dictated by the nutrient diffusion-reaction equations. GGH model has been used in simulating various cell level and tissue level phenomena such as avascular tumor growth, angiogenesis[97], and biofilm simulations[98, 197]. Due to their ability to handle multiple cell types, each with their own interacting energies, GGH model can be readily used to simulate multispecies bacterial communities somitogenesis [200].

Bacterial biofilms are community-driven biological systems, which warrant the use of Agent-Based simulations to explore their emergent properties[12]. In general, bacterial biofilms consist of structures that house millions of bacteria that stay as a single colony. The bacteria in the biofilms are different from planktonic cells, the free roaming

bacteria, in that they are confined within the biofilm and are seldom motile. The community members (bacteria) interact at microscopic levels with each other and the ambient environment to define the overall evolution of the system[201]. Such a community-driven system can only be effectively modelled using Agent-Based methods, in particular GGH models. The biofilms offer cover to the confined bacteria from antibiotics [202, 203], bacteriophages, and external stresses. Due to their strong adherence to the substratum, they are hard to remove or eradicate, thus leading to biofouling and microbial induced corrosion (MIC) of the adhering surface. Biofouling of pipes used in heat exchangers[204] or offshore structures[205] may lead to pressure drop, leading to system failure and damage. Bacterial biofilms are also a major concern in Fast Breeder Test Reactor[206] or other nuclear reactors [25] due to their presence in the cooling water systems. Any uncontrolled build-up of biofilms within these systems will result in devastating consequences. In cases of water treatment plants, growth of biofilms decreases the flux of treated water, necessitating increase of pressure within the system [207, 208] thus adding to operational costs. To prevent such outcomes, bacterial biofilms must be periodically removed from the systems. The mechanical process of biofilm removal is known as detachment, where a part or whole of the biofilm is removed from its original site due to mechanical stresses from flowing fluid and localized structural defects occurring within the biofilm. In most industries, detachment of biofilms is carried through high pressure washing or mechanical scrubbing [209]. The efficiency

of such methods depends on parameters such as the type of the biofilm, the location of biofilm within the structure and device geometry. There have been simulation studies to estimate the detachment rate of biofilms in various systems. Quantifying the detachment process started with modelling the rate of detachment as a function of biofilm thickness [210, 211] or biomass density, ignoring the spatial effects of the biofilm structure. There have been models that address the spatial detachment process using stochastic variables dependent on the height of the biofilm or relative position of the bacteria in a biofilm [212]. Piciorreanu et al[213] developed a more realistic shear stress-based detachment model assuming the biofilm as an elastic structure. They simulated 2D flow in a channel comprising the biofilm and evaluated the detachment rate of the bacteria with time. Following a similar approach, Tierra et al.[214] developed a three- phase multicomponent model, where they considered biofilm as an incompressible viscous fluid that deforms from interaction with the ambient forces. Similar fluid structure interaction models have been developed for other biological systems such as corals [215] and blood flow [216]. However, treating the entire biofilm as a single mechanical structure with homogenous physical and biological properties does not truly represent the heterogenous nature biofilm's mechanical properties. It has been shown that the physical properties such as tensile strength vary throughout the biofilm based on the localized bacterial populace and EPS distribution. To capture such cell level dependencies of the mechanical properties of biofilm, Jayathilake et al. [196] implemented

117

mechanistic interaction between the cells using discrete element method. They assumed a fixed shear rate profile for the fluid interacting with the biofilm, which composed of hard spherical particles. This fluid-particle interaction in the model was used to predict the roughness and detachment rates of the biofilm formed. All these models, however, do not account for the localized interactions arising from the cell motility and cell shape fluctuations, which are important determinants of the biofilm's response [217] to the eradication techniques. These cell level activities can give rise to formation of mechanically interesting structures such as streamers[218], piece-wise detachment[219] of the structure and further colonization of the neighborhood[217]. GGH model-based simulations can include all such cell level activities and incorporate external force coupling with the cell through the Hamiltonian and Non-Hamiltonian energy [93] potential associations. In this paper, we develop a hybrid GGH - Finite Element Method [220] based model to understand the effect of shear stress on the shape of the biofilm and to quantify the loss of biomass due to detachment. We analyze the potential outcomes of the detachment process, based on the strength of the biofilm or the adhesion strength between individual bacteria. Since there are numerous models in literature [221] detailing the bacterial cell proliferation and nutrient based growth of biofilms, we initialize the model with a fixed structure such the classical mushroom shape, ignoring the evolution of biofilm before the initiation of the removal processes. We then examine the influence of various

biophysical model parameters such as, shear stress, adhesion potential and motility on the morphology of the biofilm structure.

5.2　Model description

5.2.1　Model for bacterial cells

We implement our GGH model using the opensource "CompuCell3D" software framework. The individual bacteria are modelled as a collection of pixels, with each pixel of length 'dx' occupying one grid point in space. The volume of the cells 'V_c' is set equal to the average volume of *Pseudomonas aeruginosa* cells [131]. The cells have inherent motility based on the membrane fluctuations, modelled by the temperature term 'T_m' in GGH model. At each simulation time step, one of the pixels (target) in the domain is chosen at random and copied to a (destination) grid point in its neighbourhood, this process is known as pixel copy attempt. If the target and destination grid points are of the same cell, then there is no pixel copy. This means that only the pixels residing along the periphery the cells or in other words, the membrane of the cells, are involved in the pixel copy attempts. The probability of success for such a pixel copy attempt or in this case the bacterial membrane fluctuation, is dictated by equation 5.1.

$$P\left(\sigma(\vec{\imath}) \to \sigma(\vec{\imath'})\right) = \begin{cases} \left[exp\left(-\dfrac{\Delta H}{T_m}\right)\right], \Delta H > 0 \\ 1, \qquad \Delta H \leq 0 \end{cases} \quad (5.1)$$

The term, ΔH is the change in energy due to the pixel copy event for the cells at positions $\sigma(\vec{\imath})$ to $\sigma(\vec{\imath'})$, where $\vec{\imath'}$ and $\vec{\imath}$ are the pixel

119

positions on the domain. The larger the value of T$_m$, the faster the membrane fluctuations occur.

Equation 5.2 imposes a volume constraint on the cell and equation 5.3 addresses the adhesion between the cells. In addition to the bacterial cells, we model the substratum as immobile group of cells with fixed volume. These cells form the bottom layer on which the bacterial cells rest and adhere to. Therefore, the adhesion between bacteria and substratum is made stronger than the bacteria-bacteria adhesion, which is reflected in the model by a lower adhesion C$_{BB}$ or $\text{Con}(\tau_{\sigma(i)}, \tau_{\sigma(j)})$ parameter for the bacteria-substratum interactions. Here, τ indicates the type of cell at the location '$\sigma(i)$' or '$\sigma(j)$. λ is the volume potential, V_T is the target volume and V$_{cell}$ is the volume of the cell. In addition to the volume and contact constraints, a connectivity constraint is included in the model. The connectivity constraint ΔE_p acts as a penalty parameter which prevents the cells from fragmentation, due to numerical instabilities[222].

$$\Delta E_V = \lambda(V_{cell} - V_T)^2 \qquad (5.2)$$

$$\Delta E_c = \sum_{i,j} Con(\tau_{\sigma(i)}, \tau_{\sigma(j)}) \left(1 - \delta_{\sigma(i),\sigma(j)}\right) \qquad (5.3)$$

The normal and shear forces experienced by the cells are modelled as a field around the cells. Since, the volume of individual pixels are very small compared to the size of the domain and the cells themselves, the

forces are applied over the surface of the pixels. In scenarios, where a part of a cell is exposed to flowing fluid, this enables applying force to only that region instead of the entire cell surface. Equation 5.4 describes the change in energy arising from the displacement of cell pixels ($|\vec{\iota'} - \vec{\iota}|$) by the GGH pseudo-force ($\overrightarrow{F_{GGH}}$ or GGH F). The GGH pseudo-force in the model is directly proportional to the stresses per unit area of pixel (Traction, $\vec{T}$), developed by the biofilm structure in response to the ambient fluid flow. (The overall implementation of the module in Compucell3D is done similar to the 'ExternalPotential' plugin [223]. The traction force $\vec{T}$ is converted to equivalent force $\vec{F}$, which acts along the entire area (S_A) of the pixel. This equivalent force is converted to pseudo GGH force, GGH F, using the proportionality constant k_{GGH}, as shown in equation 5.5b

$$\varDelta E_f = \overrightarrow{F_{GGH}} \cdot \left(|\vec{\iota'} - \vec{\iota}|\right) \tag{5.4}$$

$$\overrightarrow{F_{GGH}} \propto \vec{T} \tag{5.5}$$

$$\vec{T} = \frac{\vec{F}}{S_A} \tag{5.5a}$$

$$\overrightarrow{F_{GGH}} = k_{GGH} \, \vec{F} \tag{5.5b}$$

Thus, the Hamiltonian ΔH now includes the change in energies originating from volume constraints, adhesion potentials, connectivity penalty and pseudo-force potentials as shown in equation 5.6. This Hamiltonian is calculated at every simulation time step or Monte Carlo Step 'mcs', to determine energy of the cells and the system.

$$\Delta H = \Delta E_V + \Delta E_c + \Delta E_p + \Delta E_f \qquad (5.6)$$

5.2.2 Model for stress calculations

To estimate the traction force $(\vec{T})$ and consequently the normal (σ_n) and shear stresses (τ) arising from fluid interaction with the biofilm surface, we solve the continuity equation and incompressible Navier-Stokes (NS) equation in a 2D channel of dimensions x' × y'. An opensource finite element method-based solver, FENICS, is used for solving the continuity and NS equations. Incremental Pressure Correction Scheme (IPCS) [224] is used for the simulation of the transient state fluid flow. The biofilm is considered as a solid object along the flow path and therefore no-slip boundary conditions are applied along the surface the biofilm. The inlet velocity is fixed as a parabolic velocity profile at the channel inlet (at x = 0) as shown in equation, where $\vec{u}$, $\vec{v}$ and $\overrightarrow{u_{max}}$ are velocity in x-direction, velocity in y-direction and maximum inlet velocity respectively. a and b are constants similar to the study by Tierra et al. [214].

$$\vec{u} = \frac{\overrightarrow{u_{max}}}{a}(bY - Y^2), \vec{v} = 0, Y = \frac{y}{b}; \qquad (5.7)$$

$$p = 0; \qquad (5.8)$$

Atmospheric pressure is fixed at the exit boundary (at x = x'), the equations are solved transiently at discrete time intervals, Δt =4 min. A very low Reynold's number, $Re \ll 1$, similar to other experimental biofilm studies [225-227], is maintained in all model simulations. From the velocity and pressure values the traction force $\vec{T}$ acting on the surface of the biofilm is calculated from the stress tensor σ using equations 5.9.

$$\vec{T} = \sigma.\vec{n} \qquad (5.9)$$

The traction force is split into individual stress components acting on the surface, namely normal stress σ_n and shear (or tangent) stress τ. Normal stress acts along the normal direction $\vec{n}$ to the surface of the biofilm and shear stress acts parallel to the surface $\vec{s}$. The calculated stresses are applied as an equivalent force (eq. 5.5a) $\vec{F}$, which is then translated to GGH pseudo force $(\overrightarrow{F_{GGH}}$ or GGH $F)$ on the individual pixels of the cells, whose surface is exposed to the incoming fluid.

$$\sigma_n = \vec{T}.\vec{n} \qquad (5.10)$$

$$\tau = \vec{T}.\vec{s} \qquad\qquad (5.11)$$

The GGH pseudo-force is applied along the surface of the biofilm for approximately every 600 mcs depending on the numerical stability of the flow simulations and meshing. The mcs can be related to the real-time, based on the discrete time unit, Δt, used in the fluid flow simulations. We assume that the changes in shape of the biofilm due to the application of force does not alter the flow patterns and the shear stresses significantly within this interval (600 mcs or 4 minutes). Therefore, the steady state stresses are calculated at time 't' and the resultant GGH forces are applied on the cells from t $\rightarrow$ t+dt in the GGH interval (dt ~ 600 mcs). During this interval, the bacteria in the model respond to forces acting on the biofilms surface) based on the energy changes ΔH goverened by equation 5.1. After t+dt, the fluid flow simulations are run with the new shape configuration and the cycle is repeated until t_{max}. The entire simulation accounts for about 60 minutes in real time or 9000 mcs.

5.2.3 Generation of meshes for fluid dynamics

We generate the meshes for different biofilm shapes at different time instances using GMSH. The generation of meshes is an automated process using the grid point data of individual cells from CompuCell3D

output. We use adaptive mesh refining to make the mesh finer near biofilm surfaces and coarser elsewhere as shown in fig. 5.1c.
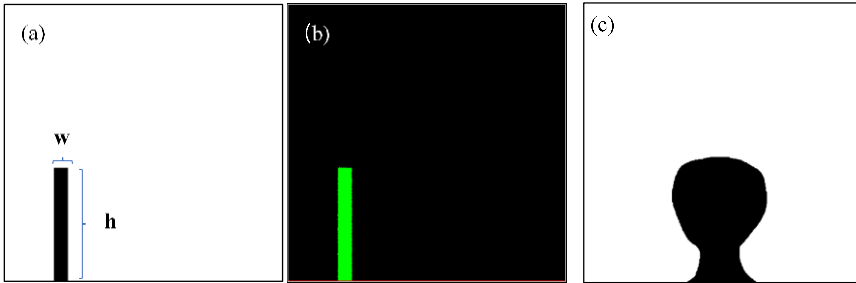

Figure. 5.1 Generation of biofilm lattice and mesh for the numerical simulations. (a) Portable Network Graphics file (PNG) describing the shape of the structure, (b) Compucell3D cell lattice recreated from the PNG file and (C) Portable Network Graphics file describing the shape of mushroom-shaped biofilm structure. Here, h is the height of biofilm, which is 405 grids and w is the width of biofilm, which is 100 grids.

5.2.4   Results and discussion

An arbitrary stump-like biofilm shape configuration (fig. 5.1a) similar to the one used by Tierra et al. [214] is drawn as an outline Portable Network Graphics (PNG) file. This outline image is initialized in CompuCell3D and discretized to individual bacterial cells occupying the marked biofilm area as shown in fig. 5.2a. The cells initialized from the image are square shaped and a few may not have their target volume V_T at the time of initialization. Therefore, the simulation is let to anneal

125

for the first 600 mcs, during which the local energy of the cells is minimized, and they attain a uniform volume and shape closer to their target volume V_T by the end of annealing steps. As the simulation proceeds, the biofilm structure starts to deform based on the stresses acting on its surface. Thus, the forces applied along the periphery are transformed into an energy perturbation traversing through the biofilm volume. The model in turn adjusts the position of the cells within the biofilm to minimize the local energy and consequently the final structure of the biofilm evolves with time. However, since the applied force is a pseudo-force, there are multiple outcomes possible with the change in values of the proportionality constant k_{GGH}. Physically, $k_{GGH}\vec{F}$ or $\overrightarrow{F_{GGH}}$, represents the strength of the force acting on the biofilm surface for 1 mcs and the order of magnitude 'O' of this force impacts the shape of the biofilm structure. In addition to the applied forces, the change in morphology of biofilm structure can be affected by two other model parameters namely, the membrane fluctuations T_m and the contact energy between the bacterial cells [C_{BB}]. These three parameters were therefore varied to understand their effects on the biofilm structure. The results from the parametric

126

variation study are summarized in fig. 5.2. The volume changes for each case of parameter variation (fig. 5.2a – g) clearly shows that there are no numerical instabilities in the GGH model and that the cells are not swelled up or crushed due to the force applied on them. Three distinct morphological outcomes are observed in fig. 5.2, (i) bending, (ii) distortion and (iii) detachment. The process of distortion occurs when the biofilm changes its shape without much loss of its individual members. This loss of bacterial cells from biofilm occurs due to their displacement by fluid shear. Heavy distortion of structures is commonly observed in biofilms with high contact energy as visible in fig. 5.2 c and 5.2 d. A high contact energy between the cells translates to less adhesion between the cells. The porosity of these distorted structures is very high compared to other biofilms in the simulation. This could mean that biofilms that do not secrete large quantity of EPS during their lifetime or biofilms that have loosely packed structures are bound to be heavily deformed by the incoming flow. The porous nature of the deformed structures indicates the propagation of the surface shear effects through the entire volume. In general, with the progress of simulation, majority of the deformed structures get removed from

their site due to fluid stress. This process is defined as detachment. From the graphs we observe two types of detachments originating in the simulations. They are removal of chunks of biofilm knows as sloughing and wash-away of individual cells in small quantities known as erosion. Erosion is a common characteristic observed in all the biofilm simulations. Erosion starts only after a considerable time since the introduction of fluid stresses. This is due to the structure getting progressively weakened by fluid flow. If erosion were to be imminent once the fluid is introduced in simulation, then the cells would be outright plucked from the biofilm by fluid force, but this is not the case. As expected, the structure experiencing high GGH forces (fig 5.2a) is more readily weakened, with erosion starting as early as 2000 mcs. But surprisingly, the structures are also weakened swiftly when their members possess high membrane fluctuation values (T_m). High values of membrane fluctuation translate to faster motility of the cell. Increased motility should have made it easy for the biofilm to adjust its structure swiftly in response to the forces experienced by its cells, instead it has resulted in an unstable configuration. This could be a side effect of the model's basic formulation which combines motility with

high energy probabilities (eq. 5.1). Minimization of the energy of the system could result in minimized external force experienced by the cells. Therefore, increase in the fluctuation amplitude will result in increased frequency of non-optimal positioning of the cells against the external field. This results in increased erosion of cells which are directly exposed to the incoming fluid.

Sloughing follows a similar pathway as erosion, removal of cells due to external force, except it is characterized by critical or total capitulation of the structural integrity as seen in fig5.2a,c,d,f and g. There are simulations in which sloughing has occurred in a biofilm more than once such as in fig 5.2a. This shows that there are multiple tipping points in the biofilm's structural integrity, which occur based on the local internal stress effects originating within the biofilm. Sloughing effects are incredibly strong in biofilms with low cell-cell adhesivity (fig 5.2c and 5.2d) due to the inherent structural instability arising from loose packing of cells. In loosely packed structures, almost entire biofilms have been detached in very early stages, as early as <3500 mcs.

Table 5.1 Parameter values used in the biofilm simulations. (mcs indicates a Monte Carlo Step, J$_{GGH}$ and N$_{GGH}$ indicate the energy and force units in the GGH domain respectively.)

| Parameter	Value
Length of simulation domain, x'	1000 grids
Height of simulation domain, y'	1000 grids
Grid size, Δx	1×10^{-6} m
Time step, Δt	240 s
Total simulation time, t	9000 mcs
Volume of bacteria [131]	27×10^{-18} m^3
Contact energy between two bacteria of specie 'B', C$_{BB}$	5-15 J$_{GGH}$
Contact energy between two bacteria of specie 'B*', C$_{B*B*}$	15 J$_{GGH}$
Contact energy between bacteria of specie 'B' and specie 'B*', C$_{BB*}$	15 J$_{GGH}$
Membrane fluctuation temperature, T$_m$	10-30 J$_{GGH}$
Pseudo GGH force, $\overrightarrow{F_{GGH}}$	$0 - 10^5$ N$_{GGH}$
Reynold's Number, Re	0.07
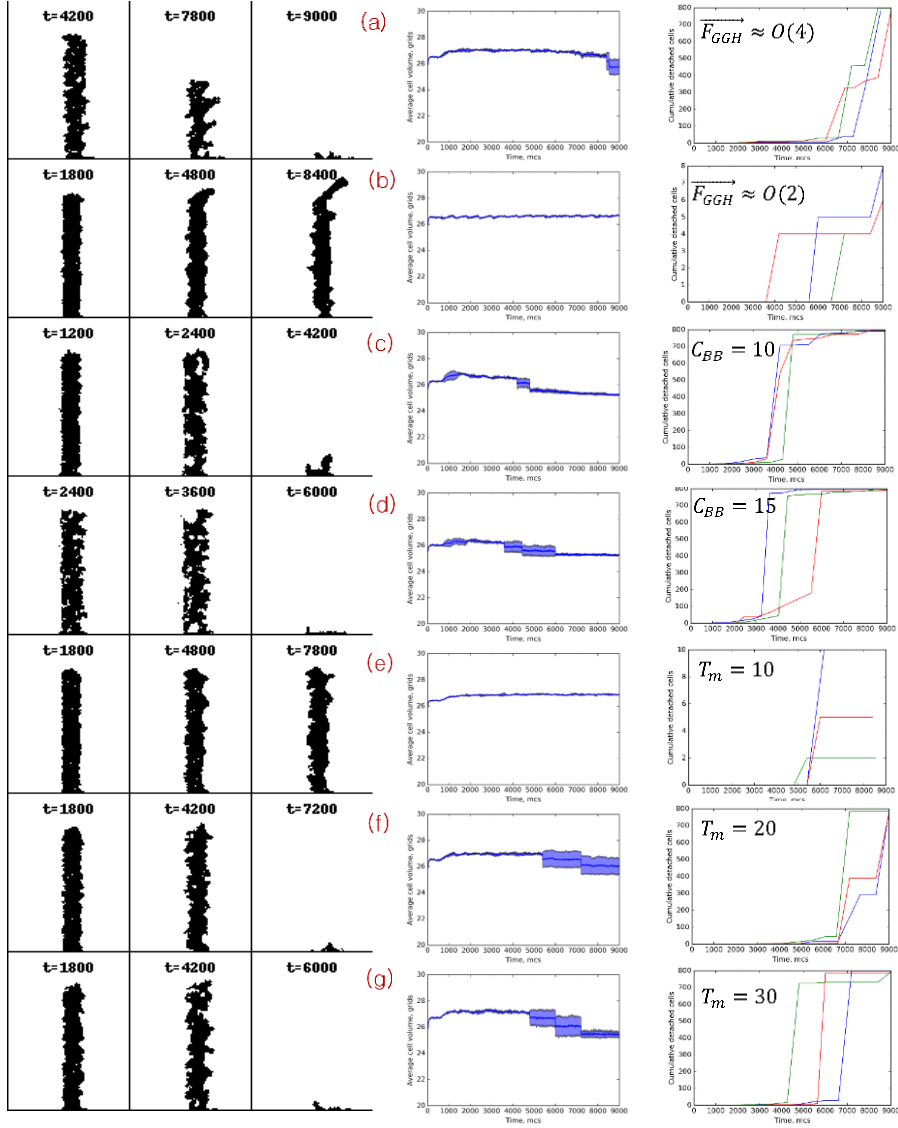
Figure. 5.2 Effect of fluid stresses acting on the biofilm structure. The snapshots show the structural deformation at different time instances, the xy plots show the change in volume with time and the second xy plots are detachment plots that show the cumulative

detached cell count with time for simulations with $T_m = 20$, C_{BB} =5 and (a) $\overrightarrow{F_{GGH}} \approx O(4)$, (b) $\overrightarrow{F_{GGH}} \approx O(2)$; $T_m = 20$, $\overrightarrow{F_{GGH}} \approx O(3)$ and (c) C_{BB} =10 , (d) C_{BB} =15; $\overrightarrow{F_{GGH}} \approx O(3)$, C_{BB} =5 and (e) $T_m = 10$, (f) $T_m = 20$ and (g) $T_m = 30$. (The values $T_m = 20$, C_{BB} =5 and $\overrightarrow{F_{GGH}} \approx O(3)$ are used as base sets and one of these values is changed in simulations. The varying parameter for each simulation is listed in the detachment plots for easy following)

To gain a better understanding of the sloughing phenomena, the velocity vectors and pressure contours are shown for a biofilm at the verge of sloughing in fig.5.3. For this case, the simulation parameters are $T_m = 20$, C_{BB} =5 and $\overrightarrow{F_{GGH}} \approx O(4)$. From plots 5.3a and b, it is clear that the velocity of the fluid near the head of the biofilm is relatively much higher than elsewhere in the biofilm. This could mean a higher force acting on the top surface compared to the bottom, which leads development of high localized stresses in this area. The only way to minimize this localized high stress is for the cells to move down or climb up the structure. Since the space above the zenith of the structure is devoid of cells and is low pressure, the cells will try to climb up, rather than moving down. But moving up the biofilm would mean fewer cells at the bottom and reduced stability of the structure. Therefore, the structure will start to detach at weak spots, where the

cell density is at its lowest. Thus, there are multiple failure points in the biofilm structure, from which sloughing can initiate and in general, these points correspond to locations with low cell density.
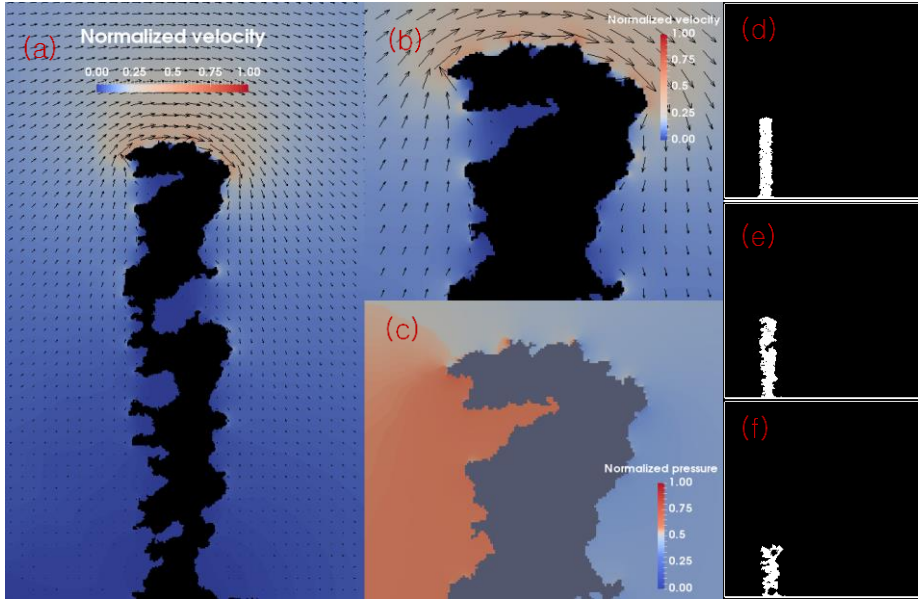

Figure. 5.3 Fluid dynamic parameters around a biofilm about to be detached. Normalized velocity vector plot for (a) entire biofilm and (b) at the top of the biofilm. (c) Normalized pressure values at the top of the biofilm. Progress of biofilm detachment at (d)1200 mcs, (e) 4200 mcs and (f) 7200 mcs.

In contrast to completely detached biofilms, in couple of cases, we find that majority of the biofilm structure has been left intact by the fluid flow (fig. 5.2b and e). These cases exhibit a bending structure,

with curved a bottom and top, which is similar to the behaviour of viscoelastic fluid under low external shear. The biofilms in these cases are elongated than their counterparts due to appearance of slender elongated structures at their top. These protrusions of single or multiple cells forming at the top of these biofilms are similar to streamers that appear in bacterial biofilms growing in an environment with continuous flow. The shape of the streamers allows them to be hydro-dynamically stable in the flowing fluid by reducing the external forces experienced by the cells within the streamer structure. Figure. 5.4 d, e and f capture the formation process of a streamer from the biofilm structure. As seen in fig. 5.3 b and c, the velocity magnitude is higher around the zenith of the biofilm (near the streamer), which could further bend the streamer and elongate it. Thus, the structure remains stable since the cells move horizontally along the streamer, parallel to the flow direction. This cell migration pattern is in stark contrast to the sloughing case where the cells could only ascend due to the absence of horizontal elongated protrusions. These observations suggest that the best way to eradicate a streamer is through back washing, whereby the

pressure is reversed. A reversal in flow would snap the streamer at its

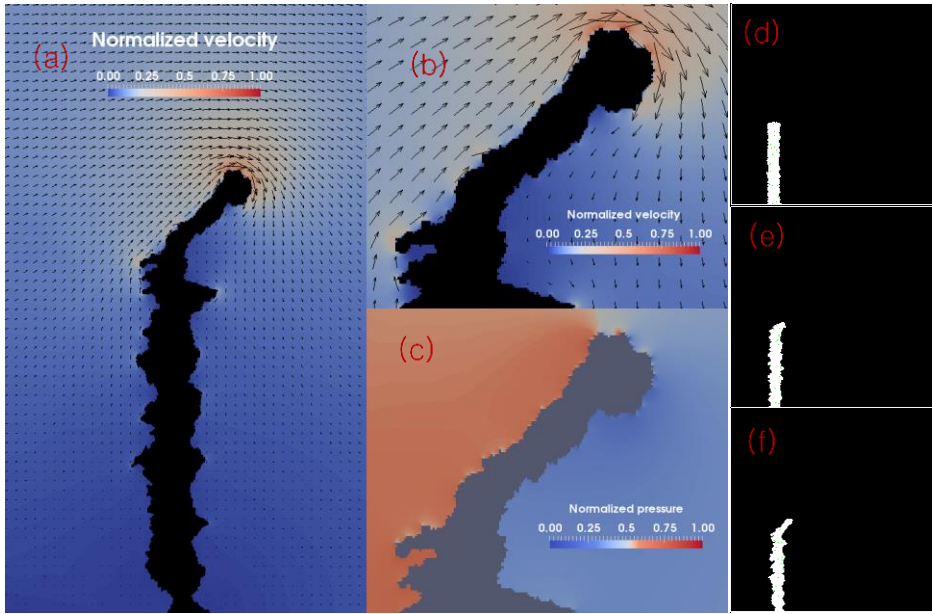base, where the cell density is very low.

Figure. 5.4 Fluid dynamic parameters around a biofilm with streamers. Normalized velocity vector plot for (a) entire biofilm and (b) near the streamers. (c) Normalized pressure values near the streamers. Progress of biofilm streamer formation at (d)1200 mcs, (e) 4200 mcs and (f) 7200 mcs.

All the discussions with regards to the arbitrary stump-like

structure simulations was centred around a homogenous bacterial

biofilm population. In natural environments, biofilms seldom exist as

homogenous entities made of same species of bacteria. They exist as

multispecies communities with each specie possessing its own biological and mechanical characteristic. In order to capture the response of such heterogenous biofilm systems to fluid shear, we carried out simulations on a mixed species biofilm modelled akin to the classical biofilm mushroom-shaped structure shown in figure 5.1c. The same base parameters ($T_m = 20$, C_{BB} =5 and $\overrightarrow{F_{GGH}} \approx O(3)$) used in the stump-like structure simulations were used for the new simulations. Three different cases were studied using the mushroom-shaped structure simulations, (i) a homogenous population, (ii) less adherent and (iii) more adherent cap mixed species populations. The less adherent species used in the simulation are denoted as B* and more adherent species is denoted by B. The contact energy values between these species are listed in table 5.1.

The results from the multispecies biofilm simulations are summarized in figure 5.5. In general, all the mushroom structures, homogenous and heterogenous, suffered structural deformation due to the fluid flow to varying degrees. The bottom parts or the stalks of the mushrooms, which face the incoming fluid, were displaced from their original position in all the cases. The effect of fluid force is more

pronounced at the cap of the mushroom, where the structure is heavily distorted. On the leeward side, the peripheral cells are found to move faster than any other cells in the structure, further confirming the propagation of stress effects through the structure. This increased motility is observed in the motility plots of fig $5.5a^+$, b^+ and c^+. Erosion is predominantly seen to occur in species B* due to their low binding affinity with each other and members of species B. It is important to note that when species B* occupies the bottom as in fig 5.5b, the stalk thins out at a rapid pace compared to the structure with species B occupying the stalk (fig. 5.5c). This means that structural configuration in fig 5.5b is inherently unstable and can be completely sloughed away earlier than its counterpart (fig 5.5c). Hence, species B* can destabilise the entire system based on its localization in the biofilm structure. Among all the three cases compared, the case with B* localization to the cap shows accelerated cell erosion as evident in the detachment plots (fig 5.5 a', b' and c'). In addition, the calculated roughness of the biofilms [133] is higher for these structures (fig. 5.5 c"). This observation suggests that accelerated erosion should be due to the lowered adhesion potential between the cells at the top, which in turn

varies the biomass thickness leading to increased roughness. Such species (B*) should be localized to the interior core of the biofilm structure, where they can protect themselves from erosion and avoid any unintended structural weakening. In nature, morphologies with strong adherent (B) bacterial species covering the peripheral structure and internalized weak adherent species (B*) should evolve spontaneously in flow systems.
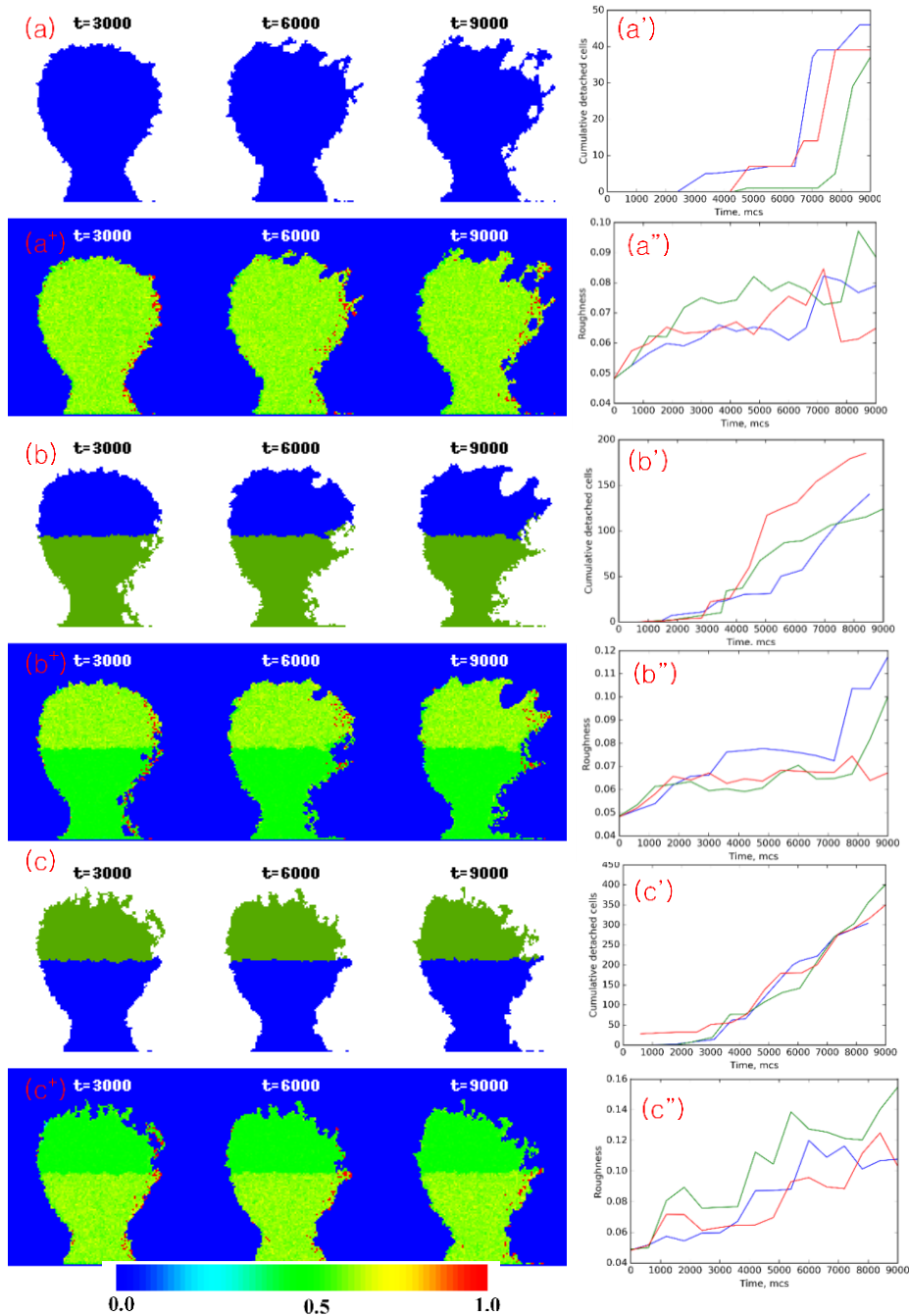
Figure. 5.5 Effect of fluid stresses acting on the mushroom-shaped biofilm structure. The snapshots show the structural deformation at different time instances ($T_m = 20$, C_{BB} =5, $C_{B^*B^*}$ =15 and $\overrightarrow{F_{GGH}} \approx O(3)$), for biofilm constituted of (a) homogenous bacterial population, (b) heterogenous bacterial population with less adherent cells at the bottom and (c) heterogenous bacterial population with less adherent cells at the cap. Plots named with superscript $^+$ show the variation of normalized cell motility with the biofilm structures, the xy plots named with superscript $'$ show the cumulative cell detachment rate and the second xy plots named with superscript $''$ are biofilm roughness plots for cases (a) , (b) and (c). The color bar at the bottom indicates the normalized cell motility for a$^+$, b$^+$ and c$^+$.

5.3   Conclusions

A GGH method-based model has been developed to understand the effects of shear stress on bacterial biofilm structures. Although we have assumed a hypothetical fluid in our simulations, based on the flow similarity principle, the velocity and pressure should have the same magnitude for any fluid flowing in the same channel with identical Reynolds number. However, the magnitude of stresses calculated will change for different fluids, depending on the density of the fluid used (lighter or heavier). Therefore, the results from the simulations will be the same for any fluid, provided the magnitude 'O' of force, $\overrightarrow{F_{GGH}}$, used

in the simulations are same. This value of $\overrightarrow{F_{GGH}}$ can be adjusted by changing the k_{GGH} in equation 5.5b. The model is also capable of predicting the formation of streamers under low stress conditions. Streamers are found to form in biofilms experiencing low external force or in biofilms with slow moving cells. Multi-event sloughing has been observed in the simulations, suggesting the presence of multiple inflection points in biofilm strength, based on local cell densities. In addition, cells with different adhesivities were introduced to examine the strength of multi-species heterogenous biofilm systems. From the simulation results, it can be hypothesised that less adherent species should always occur enclosed within the biofilm structure for prolonged survival. In future, this model can be combined with growth dynamics to predict the exact time scale of the detachment events. The model can be further improved to accommodate various other external forces such as scrubbing, impact or attrition to evaluate the efficiency of such methods in industrial biofouling clean-up activities.

6 Parallel Performance Analysis of Bacterial Biofilm Simulation Models

This chapter is based on Sheraton, M.V. and Sloot, P.M.A.,2018. Parallel Performance Analysis of Bacterial Biofilm Simulation Models. Lecture Notes in Computer Science (LNCS).

Abstract

Modelling and simulation of bacterial biofilms is a computationally expensive process necessitating use of parallel computing. Fluid dynamics and advection-consumption models can be decoupled and solved to handle the fluid-solute-bacterial interactions. Data exchange between the two processes add up to the communication overheads. The heterogenous distribution of bacteria within the simulation domain further leads to non-uniform load distribution in the parallel system. We study the effect of load imbalance and communication overheads on the overall performance of simulation at different stages of biofilm growth. We develop a model to optimize the parallelization procedure for computing the growth dynamics of bacterial biofilms.

6.1 Introduction

Computational models involving grid based or lattice-based systems are solved in parallel to reduce the overall computation time. In cases of uneven spatial distribution of grids or non-homogenous presence of model objects such as cells, catalysts or solid structures in the domain, the allocation of computational load to the processors may not be uniform. Such discrepancies will result in decrease of parallel computing efficiency. In multiphysics systems comprising of fluid flow, solute diffusion, reaction (or consumption) and cell growth, multiple methods of solving the models need to be implemented. For instance, Finite Element based Method (FEM) [228] or Lattice Boltzmann Method (LBM) [229] can be used to solve fluid dynamic equations, FEM or Finite Volume Method (FVM) [220] to solve the Fick's Equation of diffusion and solute consumption and Agent Based Method (ABM) [230] to handle the cell behavior. When combining these methods, there always exists a communication channel between them. This contributes to communication overhead in parallel computations. In addition, there will be fractional communication overhead [231] within a method resulting from memory access (gathering and scattering) between each processor. Therefore, it is necessary to estimate the communication overhead between the methods, fractional overhead, and the parallel execution durations to optimize the parallel computation process.

In nature, bacteria exhibit two modes of growth, planktonic and biofilm. During their planktonic form of growth, bacteria exist as

individual cells that float around in a fluid medium. Due to their direct exposure to ambient environmental conditions, planktonic bacteria are susceptible to antibiotics, bacteriophages, and other chemicals. In contrast, during the biofilm mode of growth, the bacteria adhere to a solid surface and to other bacteria near them, forming a large colony of bacteria confined within a structure known as biofilm. By shielding the bacteria from harsh environmental conditions, biofilms protect them from detrimental external factors and act as a platform for developing antibiotic drug resistance. Therefore, to tackle the health hazards and environmental issues arising from detrimental bacterial biofilms it is necessary to understand the dynamics of biofilm formation. Bacterial biofilm modelling has become an important tool in analyzing and predicting the quorum sensing [232] within the bacterial community, detachment of biofilms [49, 233], and phage-bacteria interactions [234]. Bacterial biofilms are complex systems that require multiphysics based models to effectively describe their evolution process. In most studies [98, 131, 132], proliferation of bacteria is modelled by considering the diffusion of essential nutrients such as oxygen or glucose around them. The individual bacterial cells are commonly represented as 'point sinks' or reaction zones within the diffusion domain. Thus, bacteria consume diffusing nutrients and proliferate based on the rate of consumption governed by Monod kinetics [235], Tessier kinetics [130] or other rate equations. The diffusion process is usually solved using grid-based methods, which can also be parallelized. Bacterial distribution on the grids is non-homogenous and

localized to regions where biofilms are present. This leads to variable load allocation on the processors, with maximum load on the processor solving the grid points comprising most bacteria. In addition, bacterial biofilms in experiments are grown in flow cells [127], which have fluid flowing within the chambers growing biofilm. Here, computational fluid dynamics (CFD) needs to be implemented to model the effect of fluid on the mass transfer of nutrients. Such complex model system with CFD and solute mass transfer necessitates parallelization and optimization of the solving process. A few studies in literature have addressed the concerns of parallel computation in cell-level biological models [236, 237]. However, these studies are restricted to analysis of parallel efficiency in a single method (either CFD or solute mass transfer) and ignore the communication overhead arising from coupling multiple methods.

We develop a model to analyze and optimize parallel computations in biofilm growth simulations. In the model, we extend the load balancing model proposed by Alowayyed et al. [236] to include the communication overhead between the methods. The effects of domain size, bacterial cell distribution and mesh element size on the parallelization efficiency are analyzed. Also, we develop a simplified function based on the above parameters to obtain the optimal number of processors required to simulate different stages of biofilm growth.

6.2 Methodology

6.2.1 Computational Methods

We have two processes involved in the biofilm model, (m1) fluid dynamics simulation and (m2) solute simulation. To model the fluid dynamics of the growth medium in the simulation domain, we solve the incompressible Navier-Stokes (NS) equation and continuity equation listed in Eq. 6.1 and Eq. 6.2 respectively. In Eq. 6.1 $\boldsymbol{u}$ is the velocity vector, $\boldsymbol{p}$ is the fluid pressure, ν is the kinematic viscosity and g is the external force (gravity) acting on the fluid. In cases of biofilm growth, the knowledge of steady-state nutrient concentration is required to model the cell proliferation. There are two ways to predict the steady state velocity profiles, solve the NS and continuity equations assuming no change of velocity with time, ie., $\frac{\partial \boldsymbol{u}}{\partial t} = 0$, or solve the equations taking small time steps 'dt' until the spatial velocity values converge. In our study, for numerical stability and accuracy we use the latter method of solving the transient state flow to arrive at steady state velocity. For simulating the flow, we use FENICS [238, 239], an open source finite element based partial differential equation solver. NS and continuity equations in FENICS were implemented using Incremental Pressure Correction Scheme (IPCS) [240]. The meshing for the fluid flow domain was done using GMSH [241]. GMSH is an open source mesh generation tool. We generate adaptive meshes to simulate the flow, that is, the mesh elements get finer as they approach the surface of biofilm.

147

$$\frac{\partial \boldsymbol{u}}{\partial t} = \nu \nabla^2 \boldsymbol{u} - \nabla \mathbf{p} + \boldsymbol{g} \qquad (\mathbf{6.1})$$

$$\nabla. \boldsymbol{u} = 0 \qquad (6.2)$$

The second simulation (m2) is the solute convection-diffusion-consumption (CDC) simulation, modelled using Eq. 6.3 and Eq. 6.4. The solute concentration evolution is defined by Eq. 6.3. where, C is the concentration of glucose, D is the diffusivity of glucose, r is the rate of consumption of glucose by the cells. The steady state velocity for estimating the convection-diffusion is obtained from the FENICS solution. This solution is coupled with the Finite Volume (FV) mesh generated in FiPy [242]. FiPy is a partial differential solver based on (FV). To solve the equations in parallel we use the solver module, PyTrilinos, a python wrapper for open source Trilinos modules [243].

$$\frac{\partial C}{\partial t} = D\nabla^2 C - \boldsymbol{u}.\nabla C - r \qquad (6.3)$$

$$r = \left(\frac{\mu_m}{Y} + m\right) B \frac{C}{K + C} \qquad (6.4)$$

6.2.2 Modelling set-up and assumptions

The bacteria in the biofilm are modelled to occupy a set of connected grid points with the simulation domain. In this study, we analyze three different biofilm settings, (i) The initial adhesion stage where only a few cells are present, (ii) Intermediate growth stage with a hemispherical structure and (iii) A final mushroom shaped structure as shown in fig 6.1. For the boundary conditions in FENICS, we assume a constant velocity inlet, atmospheric pressure boundary condition at the outlet and no slip boundary conditions near the bacterial cells in the domain as mentioned in equations 6.5,6.6 and 6.7 respectively. The mesh is refined near the bacterial cells to improve numerical accuracy. All the simulations are carried out for a Reynold's number, Re, of 100. A fixed number of iterations is carried out such that the solution converges to a steady state.

$$\boldsymbol{u} = \boldsymbol{u_o}, \qquad \text{at x} = 0 \qquad\qquad (6.5)$$

$$\boldsymbol{p} = 0, \qquad \text{at x} = \text{nx} \qquad\qquad (6.6)$$

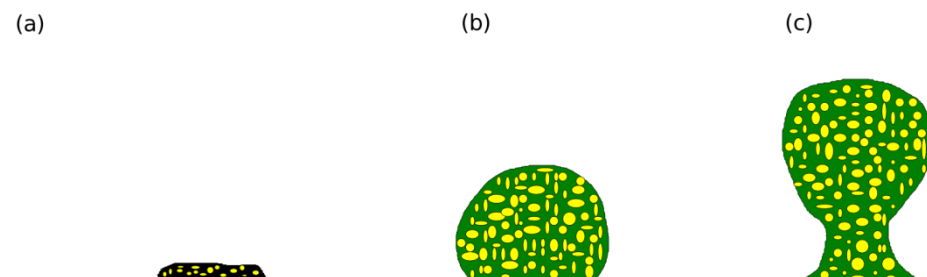$$\boldsymbol{u} = 0, \qquad \text{along biofilm surface} \qquad\qquad (6.7)$$

Figure. 6.1 Schematic of various stages of bacterial biofilm growth, (a) Stage 1: The initial adhesion stage, (b) Stage 2: Intermediate growth stage and (c) Stage 3: Mature mushroom shaped biofilm structure. Yellow color indicates the bacterial cells and dark green color indicates the extracellular polymeric substances.

We model growth dynamics of the bacteria using single substrate Monod kinetics given by Eq. 6.4 Here, μ_m, is the maximum specific growth rate, Y is the mass yield coefficient, m is the metabolic maintenance coefficient, B is the biomass present at the grid and K is the saturation coefficient. Multiple studies involving the bacteria, *Pseudomonas aeruginosa*, have used Monod kinetics due to its simplicity and the availability of literature data [123, 131]. Here, Glucose (C) is assumed to be the critical nutrient for the bacterial growth and survival. The convection-diffusion-consumption is solved for steady state by assuming $\frac{\partial C}{\partial t} = 0$. A fixed concentration inlet 'G_{ini}' is used at the inlet boundary, x = 0 and at all other boundaries no-flux boundary condition is used. We use a fixed number of iterations, large

enough to let the solutions converge. The values used in the simulation are listed in table 6.1.

Table 6.1 Parameter values used in the biofilm simulations. (g_b is the quantity of biomass, expressed in grams)

Parameter	Value
Length of domain [131]	750 x 10^{-6} m
Height of domain [131]	450 x 10^{-6} m
Number of grids in FiPy simulation	1250 x 750
Initial glucose concentration, G^{ini} [131]	3 $g\ m^{-3}$
Initial mass of bacteria, B_C [131]	1.315 x 10^{-13} g_b
Half-saturation coefficient, K_s [131]	2.55 $g\ m^{-3}$
Diffusion coefficient, D$_s$	2.52 x 10^{-6} $m^2 h^{-1}$
Specific growth rate, μ_m [131]	0.3125 h^{-1}
Mass yield coefficient, Y [131]	0.45 $g_B\ g^{-1}$
Metabolic maintenance coefficient, m [131]	0.036 $g\ g_b^{-1}\ h^{-1}$
Reynold's Number, Re	100

To estimate the parallel performance, we adapt the models developed by Axner et al. [244] and Fox [231]. We use Eq. 6.8 to estimate the time taken to complete the computation through parallel execution, T_{mi}, from number of processors (P), the time for sequential computation ($T_{i,s}$), and the overheads arising within the individual process ($T_{overheads}$). The term $T_{overheads}$ does not include the

communication overhead between the processes m1 and m2. We introduce an additive term T_{comm} which considers the overhead from communication between the two processes m1 and m2. Thus, Eq. 6.8 is now modified as Eq 6.9 which estimates the total time 'T' taken for the computation of both the processes, where the i in T_{mi} indicates the process number.

$$T_{mi} = \frac{T_{i,s}}{P} + T_{overheads} \tag{3.8}$$

$$T = T_{comm} + \sum_{1,2} T_{mi} \tag{3.9}$$

Now we estimate the fractional load imbalance on each processor using the model developed by Alowayyed et al [236]. Consider $t_{j,i}$, the time taken by processor j working on process i to complete the computation. When the load is distributed properly, that is when the domain decomposition and cell data allocation to processors is done evenly, we have $t_{1,i} = t_{2,i} = t_{3,i} = ... = t_{P,i}$. However, due to heterogenous cell distribution in the domain and differences in spatial grid smoothness such a scenario is not possible. Thus, the fractional load imbalance $f_{l,i}$ is calculated depending on the average execution time, $<t_i>$ and maximum processor execution time t_i^m using equation 6.10. The speed up and parallel efficiency are quantified using Eq. 6.11 and Eq. 6.12 respectively.

$$f_{l,i} = \left(\frac{\left(t_i^m - \left(\frac{T_{i,s}}{P} \right) \right)}{\frac{T_{i,s}}{P}} \right) = \frac{t_i^m}{<t_i>} - 1 \qquad (6.10)$$

$$S_p = \frac{T_{i,s}}{T_p} \qquad (6.11)$$

$$E_p = \frac{S_p}{P} \qquad (6.12)$$

6.3   Results and Discussion

Initially, we fix the domain size, the mesh smoothness and run the simulations on a single processor (sequentially) to analyze the velocity patterns and concentration contours developed in the domain containing a mature biofilm structure shown in fig. 6.1c. As shown in fig. 6.2, the simulations can predict the changes in velocity and glucose concentration in the vicinity of the cells.
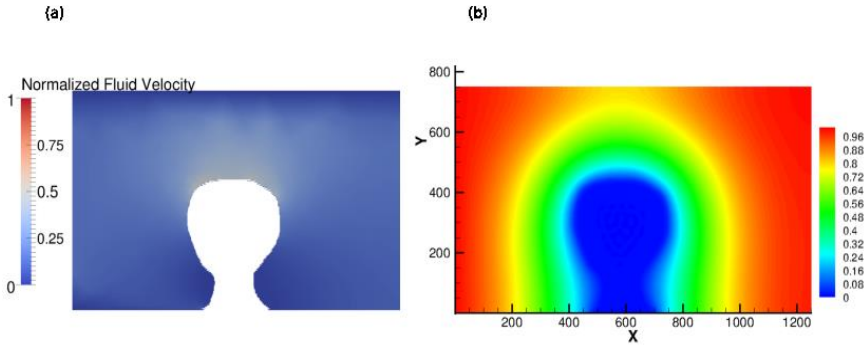
Figure. 6.2 Simulations on mature biofilm structure, (a) fluid dynamics simulation result showing the normalized velocity within the domain and (b) CDC simulations showing the normalized glucose concentration distribution in the domain.

All the simulations in the study were carried out on 3.20 GHz Intel® Core™ i7-6900K CPU running Ubuntu Linux 14.04. The parameters shown in table 6.1 were used for all the simulations, hence, the effects of change in domain size or change in fluid flow characteristics were not analyzed in this study. The total time taken for the simulations to converge to steady state were 845 s and 145 s for the fluid dynamics and CDC simulations respectively. There will be a communication overhead between the processes even when running sequentially, as indicated by the additive term in Eq. 6.9. In the next step, we simulated the fluid flow and nutrient diffusion patterns for the various stages of biofilm developments shown in fig. 6.1. We restrict ourselves to these three stages of growth since after stage 3, due to nutrient depletion, there is a possibility of bacterial dispersion from the biofilm. In this study, parallel performance analysis during the biofilm dispersion process is not included due to the possibility of multiple structural configurations during the dispersion process. We varied the number of processors P from 1 to 16. The results of the simulations are shown in fig. 6.3. We observed a plateauing of the computation time as the number of processors increased. This is due to the increase in overhead between the individual processors with increase in parallelization. Also, an interesting observation is that the stage 2 biofilms required longer processing time than stage 3 due to the larger

number of mesh elements required to simulate stage 2 as shown in fig. 6.3c. The effect arises solely from the quantity of the mesh elements and not from the quality of the elements, since all the meshes had the same minimal element radius of 0.18. The increase in number of mesh elements could be due to the meshing algorithm being dependent on the geometry of the biofilm area. However, the communication time between the processes did not follow an established trend. Since there is always a load imbalance when using parallel processors as shown in fig. 6.4a, the heterogenous distribution of mesh elements would result in variable response duration for each processor to the communication signal, thereby causing inefficient inter-process communication. This inefficient communication is evident in the mesh-dense stage 2 biofilm simulations, where the mesh decomposition is much more heterogeneous.
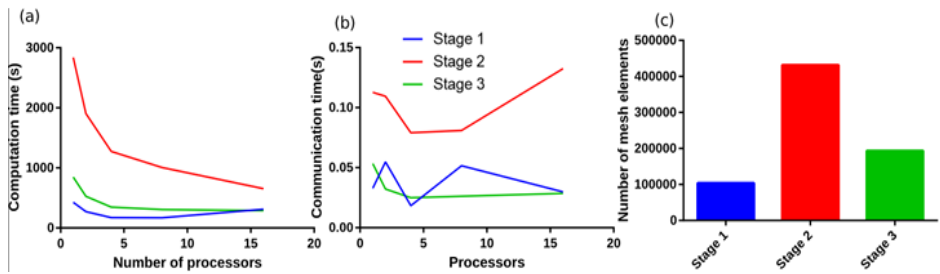

Figure. 6.3 Parallel performance at different stages of biofilm growth (a) change in computational time with increase in parallel processors, (b) change in communication time between processes m1 and m2 with increase in parallel processors and (c) number of mesh elements (N_e) used in the fluid dynamics simulation.

The estimated fractional load imbalance from the simulations is shown in fig. 6.4(a). In general, the load imbalance increased with increasing number of processors, and followed a sigmoidal curve pattern indicating the asymptotic nature of the load imbalance. The asymptotic behavior can be explained from the fact that, as the number of processors increase, the heterogeneity between the meshes allotted to the individual process decreases, resulting in an equilibrium value for fractional load imbalance. Figure 6.4(b) shows a decrease in efficiency of parallel computation at higher processor counts. This trend is expected since there is always an efficiency loss from intra-communication overheads between the processors. We also infer that, efficiency is a function of mesh elements and number of parallel processors. The geometry of the stage 2 biofilm necessitates use of large number of mesh elements to have a refined mesh boundary. Therefore, stage 2 biofilm with large number of mesh elements operates at a higher efficiency with large number of processors (>8) and underperforms with lesser number of processors than its counterparts. Although the fractional load imbalance for stage 1 biofilms is significantly higher than stage 2 and 3 biofilms using 4 processors, the efficiency for stage 1 biofilms is marginally higher than stage 2 and 3 biofilms due to the presence of fewer meshing elements and homogenous element distribution. Thus, the average number of mesh elements per processor (N_p) determines rate of decrease in parallel efficiency. We could therefore write a simplified function,

$$E_p = E_p(P, N_e, N_P) \qquad (6.13)$$

156

Increase in N_p while using large number of processors will therefore result in increased processor efficiency. Practically, this could be done by refining the fluid dynamics mesh. However, the mesh refinement should be optimized such that the trade-off between parallel efficiency and total computation time 'T' stays optimal. A similar trend is observed with the speed up values since it is indirectly proportional to the parallel computation time as shown in Eq. 6.12.
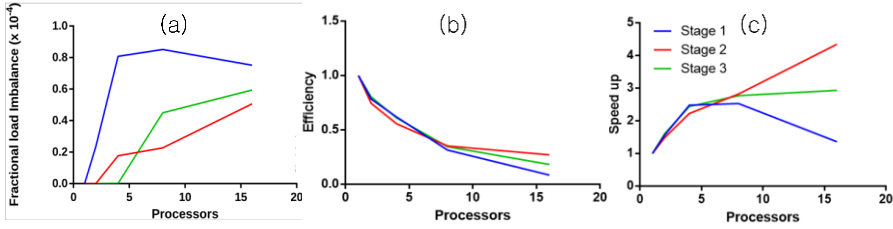

Figure. 6.4 Parallel efficiency test results, (a) estimate of fractional load imbalance on the processors, (b) change in parallel processing efficiency with increase in parallel processors and (c) Speed up resulting from change in number of processors.

6.4   Conclusion

We modeled the parallel computation efficiency at different stages of a multi-physics implementation of biofilm growth. It was found that high parallelization, at initial stages of biofilm growth simulations is not needed, since the computational efficiency from parallelization is offset by the intra-process overheads. The intermediate stage requires more parallel processors to decrease the overall computation time. This is due to the presence of large number

of mesh elements at this stage. Therefore, as a rule of thumb, the number of processors needed to optimize the speed of execution of the entire biofilm growth simulation is, $\left(N_p\right)_{stage1} < \left(N_p\right)_{stage2} > \left(N_p\right)_{stage3}$. We have developed a simplified function (E_P) dependent on the number of processors, total number of mesh elements and the mesh elements per processor for optimizing the parallel efficiency in simulating bacterial biofilm growth.

7 Conclusions and future works

The research presented in this thesis revolve around a common theme 'emergent nature of bacterial biofilm and its ecosystem'. Each chapter analyses a significant non-linear phenomenon emerging from the biofilms, in response to its interaction with the surrounding. Instead of developing a single unified model that fits in all the studies, a modular approach has been used in the model development process. The modelling process was broken down to the rudimentary principles that need to be captured by the models. There are three basic principles in the models, cell behaviour, chemical species transport and fluid dynamics. Cell behaviour has been captured using the GGH models, chemical species transport has been modelled using FVM and fluid dynamic simulations have been handled using FEM. Thus, the framework developed for the simulation studies includes three modules namely, GGH, FVM and FEM based modules. These three modules have been coupled in different ways, as necessary, to capture the underlying dynamics of the biofilm phenomenon under study. Chapter 3 includes the GGH and FVM modules to simulate and predict the morphological changes in biofilms at their developmental stages. GGH and FEM modules have been incorporated in the development of the biofilm's fluid shear response model of chapter 5. A spatiotemporally coupled model comprising of FEM and FVM modules has been implemented in Chapter 4 for predicting the QS-QQ signalling dynamics. In addition, the GGH module has been used for visualization

purposes in Chapter 4. Thus, although there are conceptually distinct phenomena studied in this thesis, the underlying principles steering these phenomena are interconnected and their spatiotemporal evolution has captured by numerical models built upon a common set of biophysical modules.

The biofilm morphology simulation model explained in chapter 3 has identified chemotaxis of nutrient deprived bacteria as the major driver behind the mushroom-shaped formations. The cells at the bottom of the colony that were under starvation were found to move vertically towards the regions of higher nutrient availability. This movement produces the neck or stalk structure of the mushroom morphology. Further competition and consequent displacement of the cells in the stalk structure, leads to overcrowding at the crown of the biofilm, which corresponds to the cap of the mushroom. These results have been validated by the experimental findings in the study. The chemotaxis mutants *ΔcheY* in the experiments seldom formed distinguishable stalk and cap structures in the flow cell but rather resembled the shape of a hemispherical dome. Thus, a combination of wet-lab experiments involving mutant bacterial strains and simulation models built on the coupled GGH-FVM modules have enabled us to unravel the physics behind formation of metabolically heterogenous biofilms. In the biofilms that formed the mushroom-shaped structures, segregation of bacteria based on their motility has been found to be of common occurrence. This implies formation of three distinct zones capable of expressing differential antibiotic response. The zones being, dormant

bottom layer, nutrient limited stalk and a fast proliferating cap. The antibiotic resistance can arise from the genetic mutations occurring due to local stresses in these stratified regions. Eradication of such biofilms is not straightforward, as removal of its head will mean exposure of the sturdy antibiotic resistant bottom. This necessitates development of proper biofilm removal strategies, which result in total elimination of biofilm formed in a system. Such strategies will have significant impact in medical and industrial biofilm eradication processes. In clinical setting, for diseases such as cystic fibrosis, it is of crucial importance that an antibiotic does not aid in the spread of the biofilm to nearby sites. To avoid such scenarios, in future, computational model based on the current GGH-FVM modules can be developed to address the structural effects of antibiotic combinations and predict a combination that completely removes the entire biofilm structure. A simple hypothetical example would be an antibiotic combination of two drugs, one targeting fast proliferating bacteria and other the targeting sessile cells. Such multi-targeting drug combinations would eliminate the cap and the bottom of the structure. One additional concern of using antibiotics is the development of antibiotic resistance due to their longer exposure to sturdy cells. Since the models developed will be able to address the metabolic segregation in bacteria, it can help reduce the overuse or use of incorrect antibiotics in bacterial infection treatments. Thus, the platform developed can act as a decision support tool for clinicians treating infections caused by bacterial biofilms.

The QS-QQ models developed in chapter 4 of the thesis, have helped elucidate the impact of mass transfer and QQ on QS behaviors in microbial communities. The experimental data driven models have clearly shown that intracellular QQ activity can never significantly influence the inter-biofilm QS signalling in aqueous and matrix-based environments. Only the extracellular QQ enzymes can effectively control QS signalling. Hence, intracellular QQ enzymes may not have evolved to degrade environmental QS signals as a competition measure. Overall, three major components that modulate the QS communication have been identified in the model. These include the extracellular matrix, local flow and quorum quenching (QQ). These components have been found to interact with each other and decide the outcome of inter-biofilm QS signalling. In open systems, convection is found to amplify the signal dispersal to the environment and thus extending the reach of the bacterial colony. Further, the extracellular matrix absorbs these dispersed signals and relays the signal messengers into the biofilm. This process allows long range inter-biofilm communication even at low extracellular signal concentration. This means that a bacterial species in one biofilm can send QS signals to its own specie members in a biofilm far away, without much dilution in the signalling strength.   Within the biofilm, the matrix further dictates the transfer of QS signals and QQ enzymes through differential diffusion. In general QS signals diffuse faster due to their small molecular size, this results in a dynamic competition of QS expansion and QQ neutralization of the QS present. The spatial segregation of the

individual populations within the biofilm has also been found to control the outcomes of QS-QQ signalling, based on the localized concentrations of the molecules. Thus, as a result of signal transport and species localization a highly heterogenous QS behaviour can be observed in multispecies biofilm communities. In future, these FEM-FVM module-based models can be easily incorporated into the morphology models discussed in chapter 3. A combination of these models would provide a framework for studying and evaluating hypotheses formed around the impact of QS-QQ in multispecies environment. QS has long been implicated for its role in biofilm dispersion. Hence, combining QS with biofilm growth models can lead to prediction of tipping points of mass dispersion within multispecies biofilms. One additional future use of the model would be in design of water filtration system, where species balance plays in important role in maintaining the efficiency of the filter system. QS-QQ models can help locate and quantify local species population based on experimental values of signal intensity in the substrate and the matrix.

FVM and FEM modules are computationally memory and processor intensive numerical models. Without proper optimization of these modules, simulations can take more execution time than wet-lab experiments. Chapter 7 provides the optimization rules necessary for parallelizing these modules in the context of biofilm simulations. The impact of the various stages of biofilm growth on the memory and processing efficiency of the computing machine have been analysed and summarized in this chapter. It has been found that at initial stages

of biofilm growth, when the biofilm is only a few micrometres high from the substratum, high parallelization is not advisable. This is due to the intra-process overheads offset the computational efficiency from parallelization. At later stages of biofilm growth, since the FEM model assumes no-slip conditions at the boundary, the number of elements required is lower compared to a short hemispherical intermediate biofilm shape. Thus, large number of processors are required for the intermediate stage to decrease the overall computation time. A simplified function has been developed in the study for optimizing the parallel efficiency in simulating bacterial biofilm growth. Although this study has examined both FVM and FEM modules' parallel efficiency, it has not considered the impact of traction force calculations. Since traction force calculations are done along the surface of the biofilm, it could mean that the parallel compute time could increase for fully developed biofilms with large surface area. In future, a study needs to be carried out, which analyses the parallel efficiency of a biofilm model simulation, which includes multiple interacting solutes (such as QS-QQ) and traction forces acting the surface, to better understand the computational requirements of such multiparameter models.
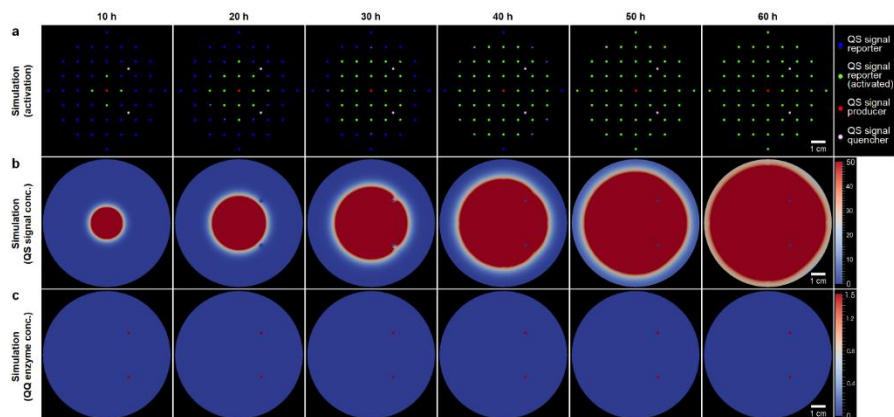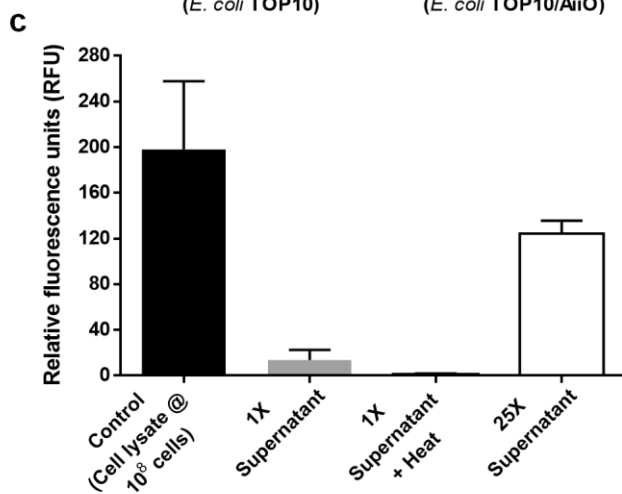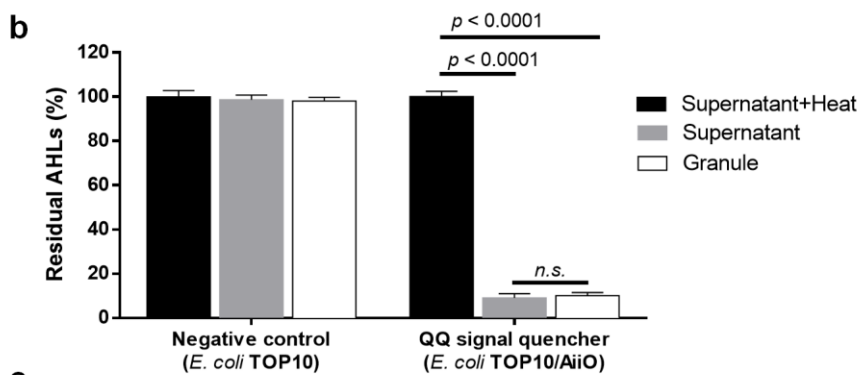
8 Appendix
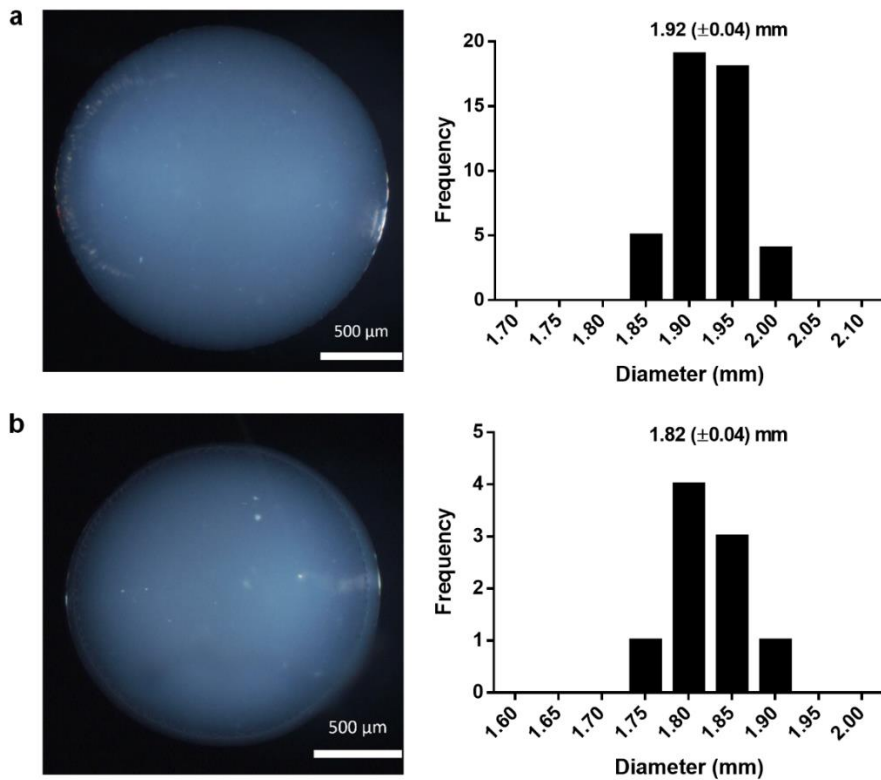
**Appendix Figure 1.** Stereo-microscopic image (left) and size distribution (right) of bacterial aggregates encapsulated in alginate hydrogel. a, QS signal (AHL) reporter cells were encapsulated in the alginate hydrogel and allowed to grow into aggregate biofilms. b, An additional layer of alginate hydrogel was coated onto the aggregates containing QS signal (AHL) producers or quenchers to prevent cell leakage.
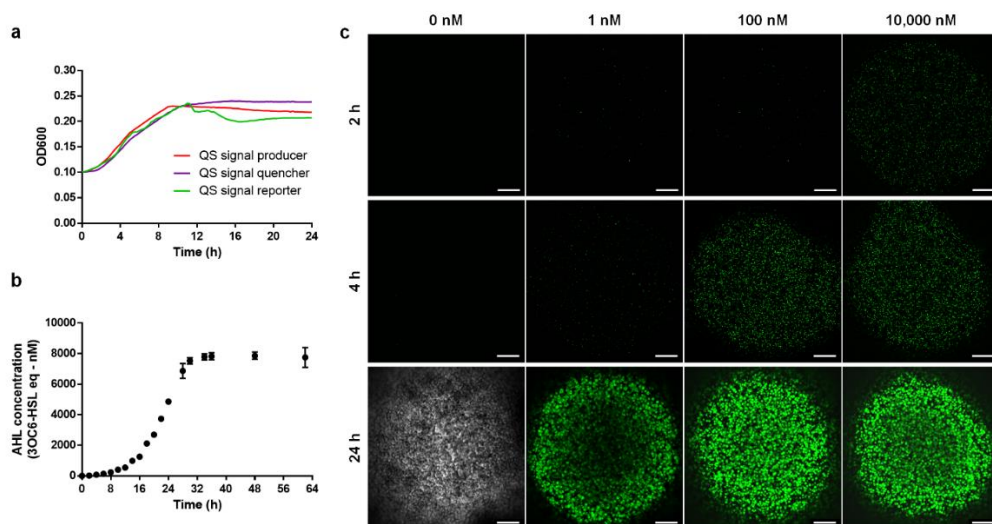
Appendix Figure 2. Characterizations of QS signal producer, quencher and reporter strains. a, Growth kinetics of individual strains. The cell density was determined over 24 h at OD_{600} nm. Means ± SD are presented (n = 3). b, QS signal (AHL) production kinetics of a single AHL producer aggregate. AHL was determined using the QS signal reporter assay. Means ± SD are presented (n = 6). c, QS signal (AHL) detection by a single AHL reporter at different concentrations of 3OC6-HSL over time. Images were acquired using confocal laser scanning microscope at 488/510 nm for GFP detection together with a phase contrast filter. Scale bar: 100 μm. In all cases (a-c), all cultures were maintained using 10% lysogeny broth supplemented with 0.095% $CaCl_2$ at room temperature. Except for (c), all cultures were maintained without shaking at 150 rpm.

Appendix Figure 3. Simulations of QS signalling in a hydrogel matrix without QQ leakage. a, Simulations of QS activation. Blue and green circles indicate uninduced and QS-activated states of reporter aggregates, respectively. Red circles located at (0, 0) indicate QS signal producer aggregates. Pink circles located at (1.5, 1.5) and (-1.5, -1.5) indicate QS signal quencher aggregates. b, Spatio-temporal prediction for the QS signal concentration profile. The colour scale: 0-50 nM. c, Spatio-temporal prediction for the QQ enzyme concentration profile. The colour scale: 0-1.5 nM. The diffusivity of QS signals (D_{AHL}), i.e., 4.75 × 10^{-6} cm^2/s was used in all simulations.
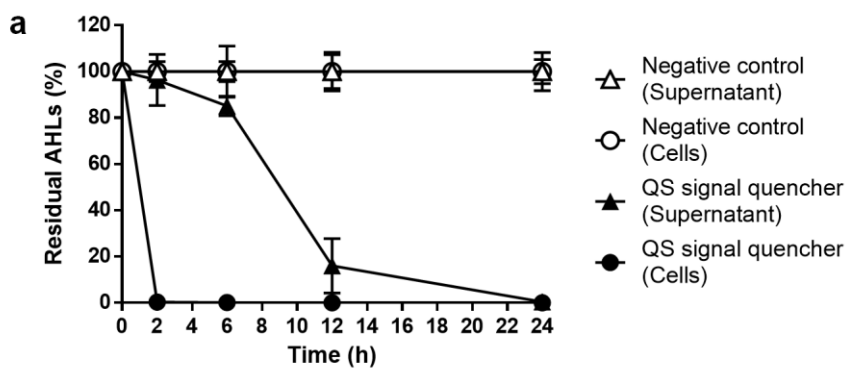
**Appendix Figure 4.** Extracellular QQ activity occurs through cell lysis. a, Temporal detection of extracellular space QQ activity. Both QS signal quencher, i.e., *E. coli* TOP10/AiiO, and the QS signal quencher mutant, i.e., *E. coli* TOP10/mAiiO, were inoculated at an initial cell density of 2×10^6 cells/mL at room temperature. Inactivation of exogenous QS signal (i.e., AHL: 3OC6-HSL) by cells suspended in PBS (i.e., intracellular QQ activity) or cell-free supernatant (i.e., extracellular QQ activity) were assessed over time. The exogenous AHL was added at 1,000 nM to each sample for 2 h and the residual AHL was detected using the QS signal reporter assay (i.e., JB525). Means ± SD are presented (n = 6). b, Detection of extracellular QQ activity. The alginate granules encapsulating the QS signal quencher, i.e., *E. coli* TOP10/AiiO, or the negative control, i.e., *E. coli* TOP10, were allowed to grow for 24 h at room temperature. Inactivation of exogenous QS signal (i.e., AHL: 3OC6-HSL) by the aggregate biofilms (i.e., granule) suspended in PBS (i.e., intra-aggregate QQ activity) or cell-free supernatant (i.e., extra-aggregate QQ activity) or heat-treated cell-free supernatant were assessed. The exogenous AHL was added at 1,000 nM to each sample for 2 h and the residual AHL was detected using the QS signal reporter assay (i.e., JB525). Means ± SD are presented (n = 6). c, Detection of extracellular alkaline phosphatase activity. The alginate granules encapsulating the QS signal quencher, i.e., *E. coli* TOP10/AiiO, were allowed to grow for 24 h at room temperature. The presence of alkaline phosphatase activity, indicative of cell lysis, in the cell-free supernatant (1X), heat-treated cell-free supernatant (1X) and concentrated cell-free supernatant (25X) were assessed. A cell lysate prepared by sonication of 2×10^8 cells was included as a positive control for cell lysis. Means ± SD are presented (n = 3).
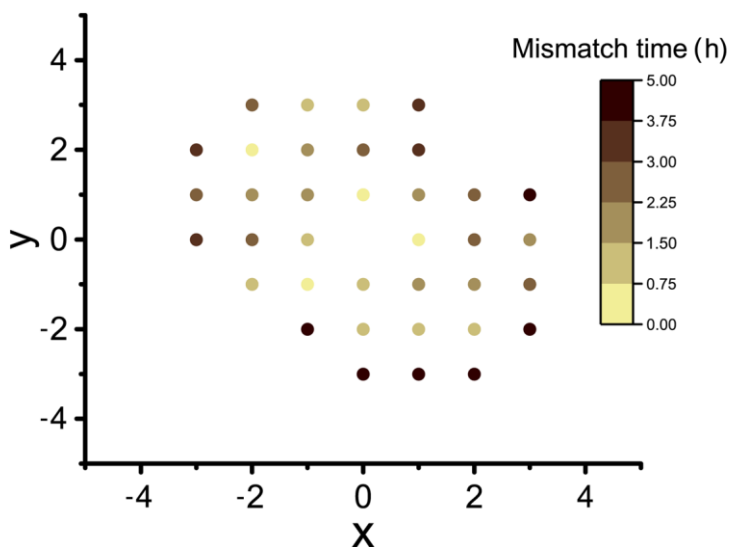
Appendix Figure 5. QS activation time mismatch between the experimental results and the simulations in a hydrogel matrix. The diffusivities of QS signals (D_{AHL}), i.e., 4.75×10^{-6} cm^2/s and QQ enzymes (D_{AiiO}), i.e., 1.35×10^{-6} cm^2/s were used in all simulations. The colour scale: 0-5 h.
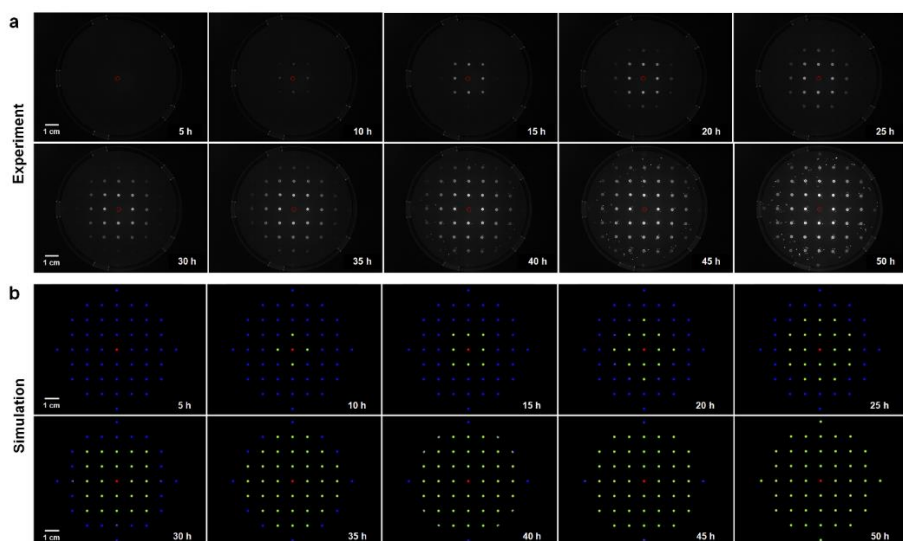
Appendix Figure 6. QS signalling in a hydrogel matrix with a single QS signal producer aggregate. a, Activation of QS signal reporter aggregates. QS signal producer aggregate (open red circles) located at (0, 0). b, Simulations of QS activation based on the signal diffusivity of 4.75×10^{-6} cm^2/s. Blue and green circles indicate uninduced and QS activated states of reporter aggregates, respectively. Red circles indicate QS signal producer aggregates.
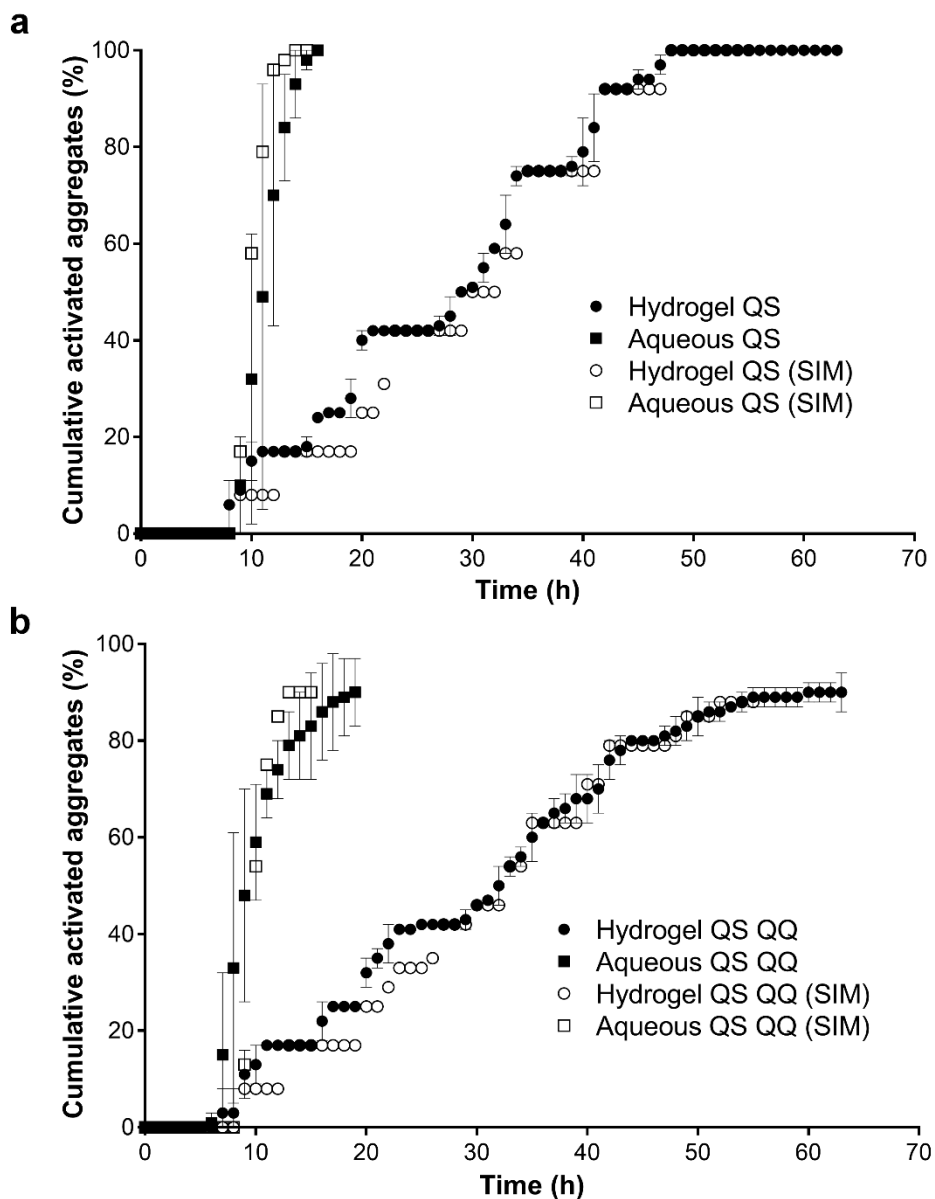
Appendix Figure 7. QS activation profiles of reporter aggregates. Cumulative QS responses of the signal reporters embedded within a hydrogel matrix (circle) or in an aqueous environment (square) were

174

determined in the absence (a) or the presence of QS signal quenchers (b) according to the community layout shown in fig. 1d. Both experimental (close) and simulation results (open) are presented. Means ± SD are presented (n = 3).
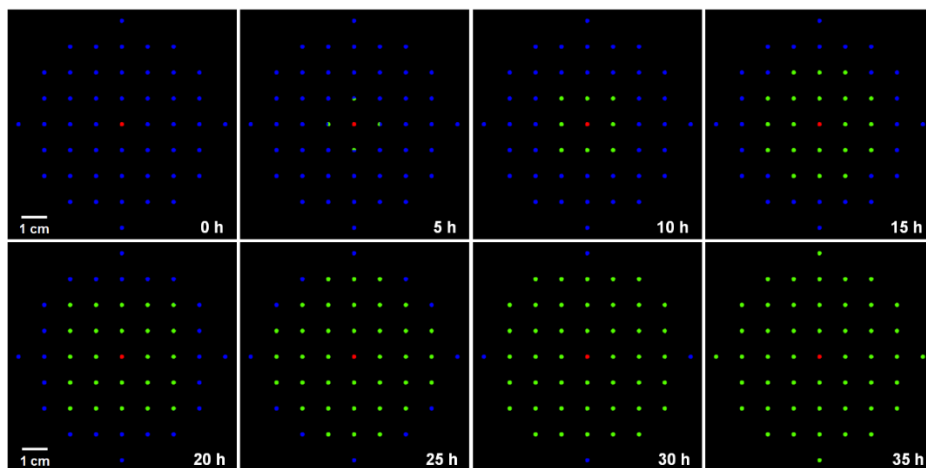
Appendix Figure 8. Simulation of QS activation in a hydrogel matrix with 100-fold increased signal production rate. Blue and green circles indicate uninduced and QS activated reporter aggregates, respectively. Red circles located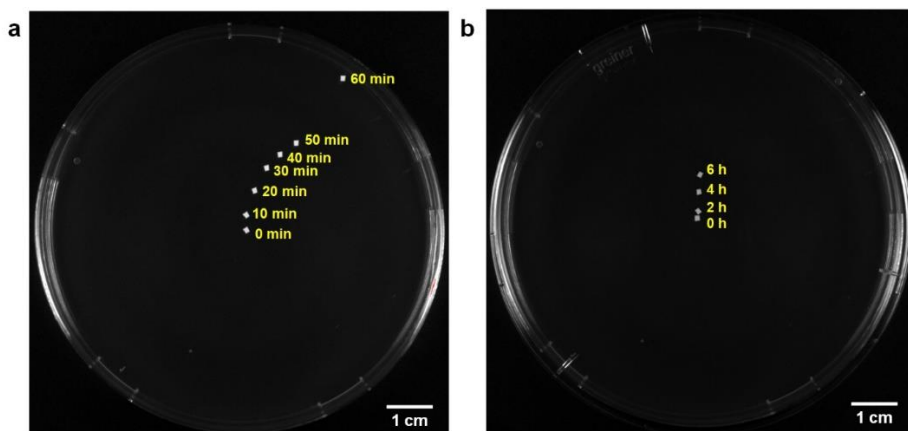 at (0, 0) indicate QS signal producer aggregates. The diffusivity of QS signals (D_{AHL}), i.e., 4.75×10^{-6} cm^2/s was used in the simulation.

Appendix Figure 9. Influence of air flow inside the enclosed chamber of Gel-Doc XR+ system on the convective flow of an aqueous medium. a, A piece of plastic slice (1.5 × 1.5 mm) was placed at the center surface of an aqueous medium in the petri-dish, and its drifting path was visualized under white epi illumination using a camera. b, The same experiment was repeated by using a transparent lid to close the petri dish so that the air flow did not affect the convective flow of the aqueous medium.
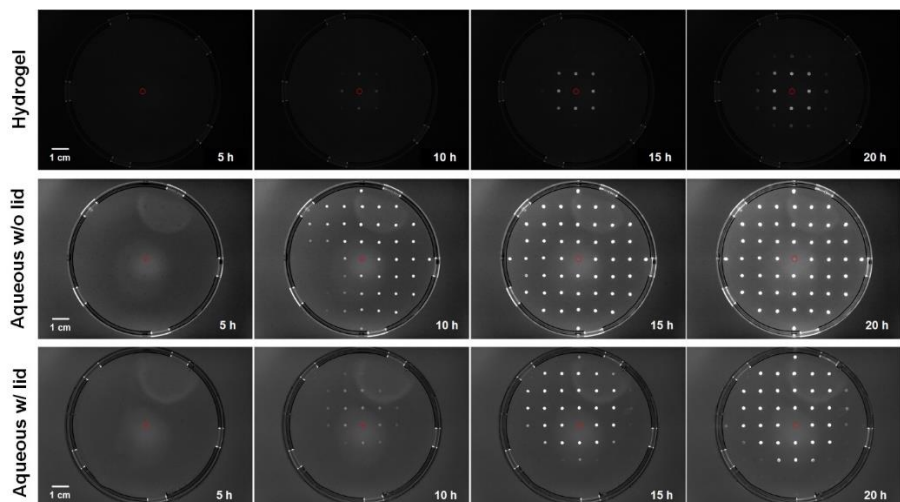
Appendix Figure 10. QS signalling with a single QS signal producer aggregate in an open hydrogel (i.e., without lid) or in an open aqueous (i.e., without lid) or in a closed aqueous system (i.e., with lid). Activation of QS signal reporter aggregates. QS signal producer aggregate (open red circles) located at (0, 0).
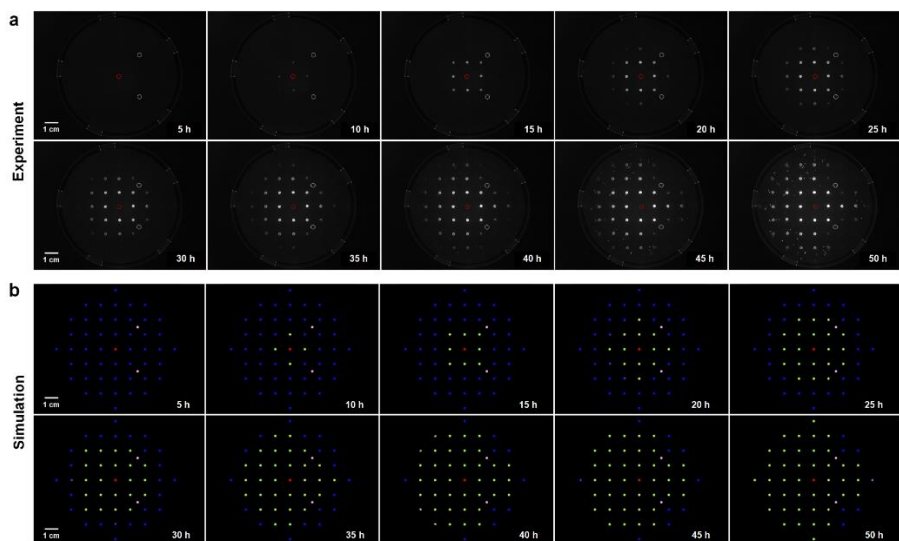
Appendix Figure 11. QS signalling in a hydrogel matrix in the presence of quorum quenchers. a, Activation of QS signal reporter aggregates. QS signal producer aggregate (open red circles): (0, 0), QS signal quencher aggregates (open pink circles): (1.5, 1.5) and (-1.5, -1.5). b, Simulations of QS activation based on the signal diffusivity of 4.75 × 10^{-6} cm^2/s, QQ enzyme diffusivity of 1.43 × 10^{-6} cm^2/s and cell leakage of 1.1%. Blue and green circles indicate uninduced and QS activated states of reporter aggregates, respectively. Red and pink circles indicate QS signal producer and quencher aggregates, respectively.

Gel-Doc XR+

Fluorescent images

Creating a template image ('Pencil tool' of Photoshop software)

Template

Analysis

Quantification of mean grey value of each reporter aggregate ('Analyze Particles' command of ImageJ software)
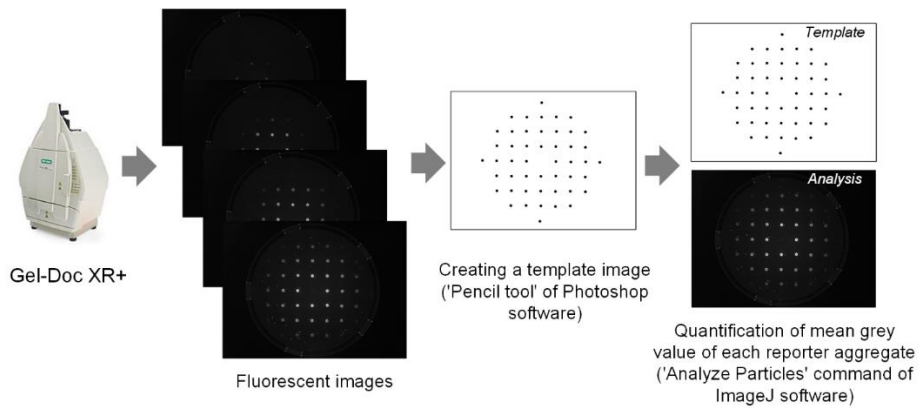
Appendix Figure 12. Scheme of image quantification process. GFP fluorescent images obtained using Gel-Doc XR+ system were analyzed using ImageJ software to quantify the fluorescence intensity for each reporter aggregate.
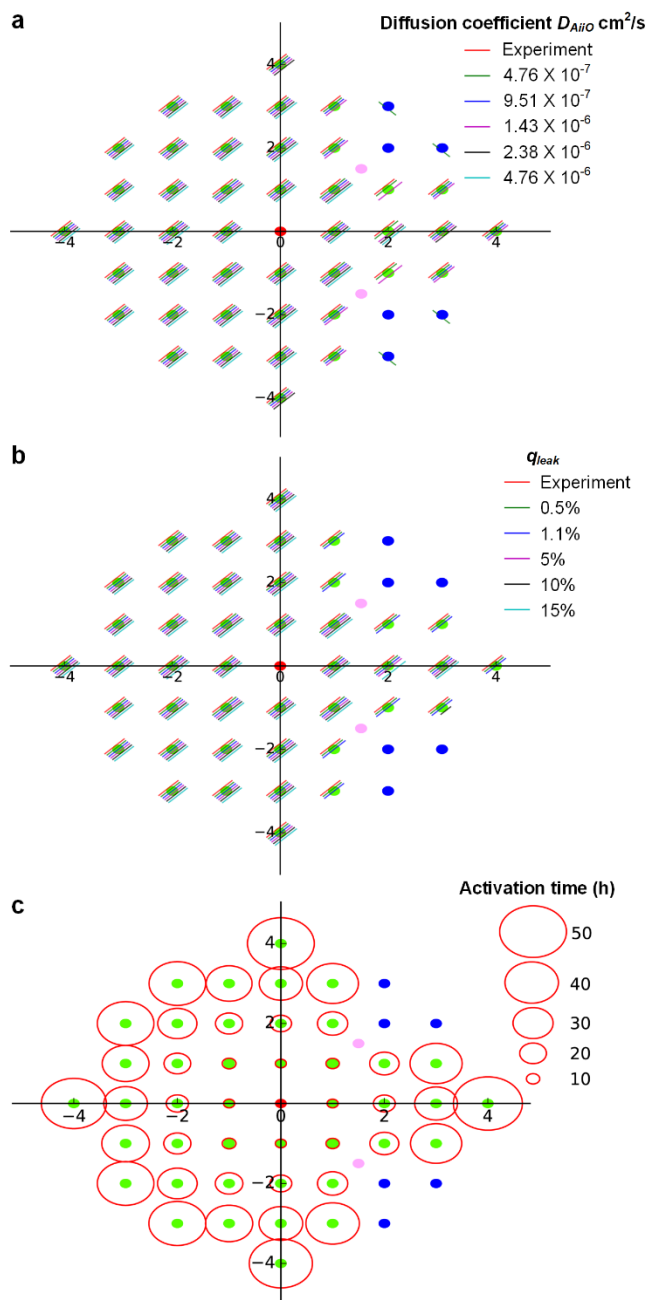
Appendix Figure 13. Parameter estimation for QS signalling in a hydrogel matrix in the presence of quorum quenchers. a, Simulations of QS activation based on the signal diffusivity of 4.75 × 10-6 cm2/s with varying diffusivities of QQ enzymes (DAiiO) and 1.1% cell leakage. b, Simulations of QS activation based on the signal diffusivity of 4.75 × 10-6 cm2/s with varying degrees of cell leakage from the QQ granule (qleak) and DAiiO of 1.43 × 10-6 cm2/s. For both a and b, the relative differences between the length of the lines denote the relative differences in the QS activation time between the experiment and simulations. c, Simulated activation time of QS signalling in a hydrogel matrix in the presence of quorum quenchers based on the signal diffusivity of 4.75 × 10-6 cm2/s, QQ enzyme diffusivity of 1.43 × 10-6 cm2/s and cell leakage of 1.1%. Size of the circles indicates the activation time of the QS signal reporter aggregates. Circle size scale: 0-50 h. For all a-c, blue and green dots indicate uninduced and QS-activated states of reporter aggregates, respectively. Red and pink dots indicate QS signal producer and quencher aggregates, respectively.

a

Ambient air flow

Air drag on upper aqueous layer

b

Slip boundary | Sliding wall boundary

Aqueous layer

Hydrogel layer

No slip boundary
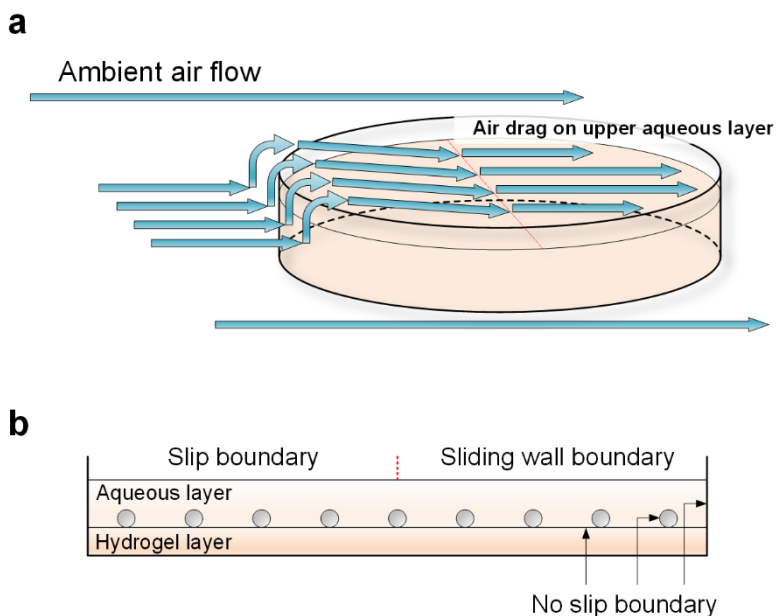
Appendix Figure 14. Influence of ambient air flow on convective flow of aqueous medium in petri dish. a, A scheme of ambient air flow. **b,** Boundary conditions implemented for solving the Navier-Stokes equation. One half of the liquid layer on the top of the petri dish is subjected to sliding wall boundary condition and the other half is set to slip condition. No slip boundary condition is applied elsewhere near the solid-liquid boundaries.
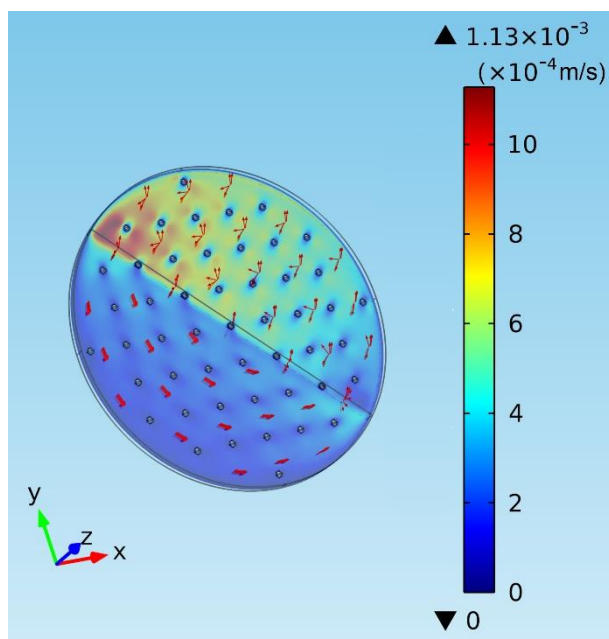
Appendix Figure 15. Velocity vectors in liquid media obtained from the Navier-Stokes simulation model. The colour bar indicates the steady-state magnitude of the velocity vectors. The spatial direction of the velocity vectors is denoted by the direction of the arrows.

Appendix Table 1. Bacterial strains used in this study.

Strain	Relevant characteristics	Reference
P. stewartii R067d	QS signal (AHL) producer isolated from a wastewater treatment plant.	[150]
E. coli TOP10	Wildtype *E. coli* strain TOP10 for plasmid transformation and gene expression.	Invitrogen, Singapore
E. coli EsaI	QS signal (AHL) producer. TOP10 strain carrying a pTrcHis2-EsaI plasmid with P_{trc}-*esaI*; Amp^R and Km^R	This study
E. coli AiiO	QS signal (AHL) quencher. TOP10 strain carrying a pTrcHis2-AiiO plasmid with P_{trc}-*aiiO*; Amp^R and Km^R	[162]
E. coli JB525	QS signal (AHL) reporter. MT102 strain carrying a pJBA132 plasmid with *luxR*-P_{luxI}-*gfp*(ASV); Tet^R	[164]

Abbreviations: AHL, acyl-homoserine lactone; *gfp*, green fluorescent protein; Amp, ampicillin; Km, kanamycin; Tet, tetracycline.

9 References

1. Štursová, M., et al., *Cellulose utilization in forest litter and soil: identification of bacterial and fungal decomposers.* FEMS Microbiology Ecology, 2012. **80**(3): p. 735-746.
2. Von Graevenitz, A., *The role of opportunistic bacteria in human disease.* Annual Reviews in Microbiology, 1977. **31**(1): p. 447-471.
3. Henrissat, B., E. Deleury, and P.M. Coutinho, *Glycogen metabolism loss: a common marker of parasitic behaviour in bacteria?* Trends in Genetics, 2002. **18**(9): p. 437-440.
4. Artis, D., *Epithelial-cell recognition of commensal bacteria and maintenance of immune homeostasis in the gut.* Nature Reviews Immunology, 2008. **8**(6): p. 411-420.
5. Van Es, F. and L.-A. Meyer-Reil, *Biomass and metabolic activity of heterotrophic marine bacteria*, in *Advances in microbial ecology*. 1982, Springer. p. 111-170.
6. Engel, M.S. and M. Alexander, *Growth and autotrophic metabolism of Nitrosomonas europaea.* Journal of bacteriology, 1958. **76**(2): p. 217.
7. Macnab, R.M., *How bacteria assemble flagella.* Annual Reviews in Microbiology, 2003. **57**(1): p. 77-100.
8. Adler, J., *The sensing of chemicals by bacteria.* Scientific American, 1976. **234**(4): p. 40-47.
9. Peel, M., W. Donachie, and A. Shaw, *Temperature-dependent expression of flagella of Listeria manocytogenes studied by electron microscopy, SDS-PAGE and Western blotting.* Microbiology, 1988. **134**(8): p. 2171-2178.
10. Teitzel, G.M. and M.R. Parsek, *Heavy metal resistance of biofilm and planktonic Pseudomonas aeruginosa.* Applied and environmental microbiology, 2003. **69**(4): p. 2313-2320.
11. Kearns, D.B., *A field guide to bacterial swarming motility.* Nature Reviews Microbiology, 2010. **8**(9): p. 634.
12. Flemming, H.-C., et al., *Biofilms: an emergent form of bacterial life.* Nature Reviews Microbiology, 2016. **14**(9): p. 563.

13. Tolker-Nielsen, T., et al., *Development and dynamics of Pseudomonassp. biofilms.* Journal of bacteriology, 2000. **182**(22): p. 6482-6489.

14. Resch, A., et al., *Differential gene expression profiling of Staphylococcus aureus cultivated under biofilm and planktonic conditions.* Applied and environmental microbiology, 2005. **71**(5): p. 2663-2676.

15. Waite, R.D., et al., *Transcriptome analysis of Pseudomonas aeruginosa growth: comparison of gene expression in planktonic cultures and developing and mature biofilms.* Journal of bacteriology, 2005. **187**(18): p. 6571-6576.

16. Wingender, J., T.R. Neu, and H.-C. Flemming, *What are bacterial extracellular polymeric substances?*, in *Microbial extracellular polymeric substances*. 1999, Springer. p. 1-19.

17. Freeman, C., et al., *Ion exchange mechanisms and the entrapment of nutrients by river biofilms.* Hydrobiologia, 1995. **297**(1): p. 61-65.

18. Römling, U. and C. Balsalobre, *Biofilm infections, their resilience to therapy and innovative treatment strategies.* Journal of internal medicine, 2012. **272**(6): p. 541-561.

19. Ciofu, O., et al., *Antimicrobial resistance, respiratory tract infections and role of biofilms in lung infections in cystic fibrosis patients.* Advanced drug delivery reviews, 2015. **85**: p. 7-23.

20. Hajishengallis, G., *Periodontitis: from microbial immune subversion to systemic inflammation.* Nature Reviews Immunology, 2015. **15**(1): p. 30.

21. Elgharably, H., et al. *Current hypotheses in cardiac surgery: biofilm in infective endocarditis*. in *Seminars in thoracic and cardiovascular surgery*. 2016. Elsevier.

22. Lehman, S.M. and R.M. Donlan, *Bacteriophage-mediated control of a two-species biofilm formed by microorganisms causing catheter-associated urinary tract infections in an in vitro urinary catheter model.* Antimicrobial agents and chemotherapy, 2015. **59**(2): p. 1127-1137.

23. Herzberg, M. and M. Elimelech, *Biofouling of reverse osmosis membranes: role of biofilm-enhanced osmotic pressure.* Journal of Membrane Science, 2007. **295**(1): p. 11-20.

24. Miura, Y., Y. Watanabe, and S. Okabe, *Membrane biofouling in pilot-scale membrane bioreactors (MBRs) treating municipal wastewater: impact of biofilm formation.* Environmental science & technology, 2007. **41**(2): p. 632-638.

25. Giacobone, A.F.F., et al., *Biocorrosion at Embalse Nuclear Power Plant. Analysis of the Effect of a Biocide Product.* Procedia Materials Science, 2015. **8**: p. 101-107.

26. Salama, P.J., et al., *Learning from listeria: safer food for all.* The Lancet, 2018. **391**(10137): p. 2305-2306.

27. Simoes, M., L.C. Simoes, and M.J. Vieira, *A review of current and emergent biofilm control strategies.* LWT-Food Science and Technology, 2010. **43**(4): p. 573-583.

28. Gibson, H., et al., *Effectiveness of cleaning techniques used in the food industry in terms of the removal of bacterial biofilms.* Journal of applied microbiology, 1999. **87**(1): p. 41-48.

29. Johansen, C., P. Falholt, and L. Gram, *Enzymatic removal and disinfection of bacterial biofilms.* Applied and environmental microbiology, 1997. **63**(9): p. 3724-3728.

30. Houry, A., et al., *Involvement of motility and flagella in Bacillus cereus biofilm formation.* Microbiology, 2010. **156**(4): p. 1009-1018.

31. Teughels, W., et al., *Effect of material characteristics and/or surface topography on biofilm development.* Clinical oral implants research, 2006. **17**(S2): p. 68-81.

32. Busscher, H., R. Bos, and H. Van der Mei, *Initial microbial adhesion is a determinant for the strength of biofilm adhesion.* FEMS microbiology letters, 1995. **128**(3): p. 229-234.

33. Cowan, M.M., T.M. Warren, and M. Fletcher, *Mixed-species colonization of solid surfaces in laboratory biofilms.* Biofouling, 1991. **3**(1): p. 23-34.

34. Koutsoudis, M.D., et al., *Quorum-sensing regulation governs bacterial adhesion, biofilm development, and host colonization in Pantoea stewartii subspecies stewartii.* Proceedings of the National Academy of Sciences, 2006. **103**(15): p. 5983-5988.

35. Labbate, M., et al., *Quorum-sensing regulation of adhesion in Serratia marcescens MG1 is surface dependent.* Journal of bacteriology, 2007. **189**(7): p. 2702-2711.

36.   Redfield, R.J., *Is quorum sensing a side effect of diffusion sensing?* Trends in microbiology, 2002. **10**(8): p. 365-370.

37.   Davies, D.G., et al., *The involvement of cell-to-cell signals in the development of a bacterial biofilm.* Science, 1998. **280**(5361): p. 295-298.

38.   Hong, K.-W., et al., *Quorum quenching revisited—from signal decays to signalling confusion.* Sensors, 2012. **12**(4): p. 4661-4696.

39.   Moy, B.P., et al., *High organic loading influences the physical characteristics of aerobic sludge granules.* Letters in Applied Microbiology, 2002. **34**(6): p. 407-412.

40.   Holliger, C., G. Wohlfarth, and G. Diekert, *Reductive dechlorination in the energy metabolism of anaerobic bacteria.* FEMS Microbiology Reviews, 1998. **22**(5): p. 383-398.

41.   Pollmann, K., et al., *Metal binding by bacteria from uranium mining waste piles and its technological applications.* Biotechnology advances, 2006. **24**(1): p. 58-68.

42.   Costerton, J.W., et al., *Microbial biofilms.* Annual Reviews in Microbiology, 1995. **49**(1): p. 711-745.

43.   Klapper, I. and J. Dockery, *Finger formation in biofilm layers.* SIAM Journal on Applied Mathematics, 2002. **62**(3): p. 853-869.

44.   Klausen, M., et al., *Biofilm formation by Pseudomonas aeruginosa wild type, flagella and type IV pili mutants.* Molecular microbiology, 2003. **48**(6): p. 1511-1524.

45.   Barken, K.B., et al., *Roles of type IV pili, flagellum-mediated motility and extracellular DNA in the formation of mature multicellular structures in Pseudomonas aeruginosa biofilms.* Environmental microbiology, 2008. **10**(9): p. 2331-2343.

46.   Taherzadeh, D., C. Picioreanu, and H. Horn, *Mass transfer enhancement in moving biofilm structures.* Biophysical journal, 2012. **102**(7): p. 1483-1492.

47.   Petrova, O.E. and K. Sauer, *Escaping the biofilm in more than one way: desorption, detachment or dispersion.* Current opinion in microbiology, 2016. **30**: p. 67-78.

48.   Kim, S.-K. and J.-H. Lee, *Biofilm dispersion in Pseudomonas aeruginosa.* Journal of microbiology, 2016. **54**(2): p. 71-85.

49.   Morgenroth, E. and P.A. Wilderer, *Influence of detachment mechanisms on competition in biofilms.* Water Research, 2000. **34**(2): p. 417-426.

50.   Morgan, R., et al., *BdlA, a chemotaxis regulator essential for biofilm dispersion in Pseudomonas aeruginosa.* Journal of bacteriology, 2006. **188**(21): p. 7335-7343.

51.   Uppuluri, P., et al., *The transcriptional regulator Nrg1p controls Candida albicans biofilm formation and dispersion.* Eukaryotic cell, 2010. **9**(10): p. 1531-1537.

52.   Sauer, K., et al., *Characterization of nutrient-induced dispersion in Pseudomonas aeruginosa PAO1 biofilm.* Journal of bacteriology, 2004. **186**(21): p. 7312-7326.

53.   Solano, C., M. Echeverz, and I. Lasa, *Biofilm dispersion and quorum sensing.* Current opinion in microbiology, 2014. **18**: p. 96-104.

54.   Sawyer, L.K. and S.W. Hermanowicz, *Detachment of biofilm bacteria due to variations in nutrient supply.* Water Science and Technology, 1998. **37**(4-5): p. 211-214.

55.   James, G., et al., *Digital image analysis of growth and starvation responses of a surface-colonizing Acinetobacter sp.* Journal of bacteriology, 1995. **177**(4): p. 907-915.

56.   Favero, M., et al., *Pseudomonas aeruginosa: growth in distilled water from hospitals.* Science, 1971. **173**(3999): p. 836-838.

57.   Høiby, N., et al., *Pseudomonas aeruginosa and the in vitroand in vivo biofilm mode of growth.* Microbes and Infection, 2001. **3**(1): p. 23-35.

58.   Williamson, K. and P.L. McCarty, *Verification studies of the biofilm model for bacterial substrate utilization.* Journal (Water Pollution Control Federation), 1976: p. 281-296.

59.   Benefield, L. and F. Molz, *Mathematical simulation of a biofilm process.* Biotechnology and bioengineering, 1985. **27**(7): p. 921-931.

60.   Kissel, J.C., P.L. McCarty, and R.L. Street, *Numerical simulation of mixed-culture biofilm.* Journal of Environmental Engineering, 1984. **110**(2): p. 393-411.

61.   Wanner, O. and W. Gujer, *A multispecies biofilm model.* Biotechnology and bioengineering, 1986. **28**(3): p. 314-328.

62.   Molz, F.J., M. Widdowson, and L. Benefield, *Simulation of microbial growth dynamics coupled to nutrient and oxygen transport in porous media.* Water Resources Research, 1986. **22**(8): p. 1207-1216.

63.   De Beer, D., et al., *Effects of biofilm structures on oxygen distribution and mass transport.* Biotechnology and bioengineering, 1994. **43**(11): p. 1131-1138.

64.   Stewart, P.S., *Biofilm accumulation model that predicts antibiotic resistance of Pseudomonas aeruginosa biofilms.* Antimicrobial agents and chemotherapy, 1994. **38**(5): p. 1052-1058.

65.   Hermanowicz, S., U. Schindler, and P. Wilderer, *Fractal structure of biofilms: new tools for investigation of morphology.* Water Science and Technology, 1995. **32**(8): p. 99-105.

66.   Matsushita, M. and H. Fujikawa, *Diffusion-limited growth in bacterial colony formation.* Physica A: Statistical Mechanics and its Applications, 1990. **168**(1): p. 498-506.

67.   Von Neumann, J. and A.W. Burks, *Theory of self-reproducing automata.* IEEE Transactions on Neural Networks, 1966. **5**(1): p. 3-14.

68.   Kroc, J., P.M.A. Sloot, and A.G. Hoekstra, *Simulating Complex Systems by Cellular Automata*. Understanding Complex Systems. 2010.

69.   Kroc, J. and P.M. Sloot, *Complex systems modeling by cellular automata*, in *Encyclopedia of Artificial Intelligence*. 2009, IGI Global. p. 353-360.

70.   Sloot, P. and A. Hoekstra, *Modeling dynamic systems with cellular automata.* 2007.

71.   Black, P.E., *Manhattan distance"" Dictionary of algorithms and data structures.* http://xlinux. nist. gov/dads//, 2006.

72.   dos Santos, R.M.Z. and S. Coutinho, *Dynamics of HIV infection: A cellular automata approach.* Physical review letters, 2001. **87**(16): p. 168102.

73.   Mallet, D.G. and L.G. De Pillis, *A cellular automata model of tumor–immune system interactions.* Journal of theoretical biology, 2006. **239**(3): p. 334-350.

74.   Mancini, E., et al., *HIV reservoirs and immune surveillance evasion cause the failure of structured treatment interruptions: A computational study.* PloS one, 2012. **7**(4): p. e36108.

75.   Sloot, P.M., et al., *HIV decision support: from molecule to man.* Philosophical Transactions of the Royal Society of London A: Mathematical, Physical and Engineering Sciences, 2009. **367**(1898): p. 2691-2703.

76.   Sottoriva, A., et al., *Cancer stem cell tumor model reveals invasive morphology and increased phenotypical heterogeneity.* Cancer research, 2010. **70**(1): p. 46-56.

77.   Naumov, L., A. Hoekstra, and P. Sloot, *Cellular automata models of tumour natural shrinkage.* Physica A: Statistical Mechanics and its Applications, 2011. **390**(12): p. 2283-2290.

78.   Smith III, A.R., *Real-time language recognition by one-dimensional cellular automata.* Journal of Computer and System Sciences, 1972. **6**(3): p. 233-253.

79.   Bartolozzi, M. and A.W. Thomas, *Stochastic cellular automata model for stock market dynamics.* Physical review E, 2004. **69**(4): p. 046112.

80.   Rothman, D.H. and J.M. Keller, *Immiscible cellular-automaton fluids.* Journal of Statistical Physics, 1988. **52**(3-4): p. 1119-1127.

81.   Kaandorp, J.A., et al., *Effect of nutrient diffusion and flow on coral morphology.* Physical Review Letters, 1996. **77**(11): p. 2328.

82.   Colasanti, R., *Cellular automata models of microbial colonies.* BINARY COMPUTING IN MICROBIOLOGY, 1992. **4**: p. 191-191.

83.   Wimpenny, J.W. and R. Colasanti, *A unifying hypothesis for the structure of microbial biofilms based on cellular automaton models.* FEMS Microbiology Ecology, 1997. **22**(1): p. 1-16.

84.   Picioreanu, C., M.C. Van Loosdrecht, and J.J. Heijnen, *Mathematical modeling of biofilm structure with a hybrid differential-discrete cellular automaton approach.* Biotechnology and bioengineering, 1998. **58**(1): p. 101-116.

85.   Hermanowicz, S.W., *A simple 2D biofilm model yields a variety of morphological features.* Mathematical biosciences, 2001. **169**(1): p. 1-14.

86.   Pizarro, G., et al., *Two-dimensional cellular automaton model for mixed-culture biofilm.* Water Science and Technology, 2004. **49**(11-12): p. 193.

87.   Chambless, J.D., S.M. Hunt, and P.S. Stewart, *A three-dimensional computer model of four hypothetical mechanisms protecting biofilms from antimicrobials.* Applied and environmental microbiology, 2006. **72**(3): p. 2005-2013.

88.   Hunt, S.M., et al., *A computer investigation of chemically mediated detachment in bacterial biofilms.* Microbiology, 2003. **149**(5): p. 1155-1163.

89.   Kreft, J.-U., G. Booth, and J.W. Wimpenny, *BacSim, a simulator for individual-based modelling of bacterial colony growth.* Microbiology, 1998. **144**(12): p. 3275-3287.

90.   Kreft, J.-U., et al., *Individual-based modelling of biofilms.* Microbiology, 2001. **147**(11): p. 2897-2912.

91.   Xavier, J.B., C. Picioreanu, and M.C. Van Loosdrecht, *A framework for multidimensional modelling of activity and structure of multispecies biofilms.* Environmental microbiology, 2005. **7**(8): p. 1085-1103.

92.   Ghanbari, A., et al., *Inoculation density and nutrient level determine the formation of mushroom-shaped structures in Pseudomonas aeruginosa biofilms.* Scientific reports, 2016. **6**: p. 32097.

93.   Glazier, J.A., A. Balter, and N.J. Popławski, *Magnetization to morphogenesis: a brief history of the Glazier-Graner-Hogeweg model*, in *Single-Cell-Based Models in Biology and Medicine*. 2007, Springer. p. 79-106.

94.   Glazier, J.A., *Grain growth in three dimensions depends on grain topology.* Physical Review Letters, 1993. **70**(14): p. 2170.

95.   Glazier, J.A., M.P. Anderson, and G.S. Grest, *Coarsening in the two-dimensional soap froth and the large-Q Potts model: a detailed comparison.* Philosophical Magazine B, 1990. **62**(6): p. 615-645.

96.   Ashkin, J. and E. Teller, *Statistics of two-dimensional lattices with four components.* Physical Review, 1943. **64**(5-6): p. 178.

97.   Shirinifard, A., et al., *3D multi-cell simulation of tumor growth and angiogenesis.* PloS one, 2009. **4**(10): p. e7190.

98. Popławski, N.J., et al., *Simulation of single-species bacterial-biofilm growth using the Glazier-Graner-Hogeweg model and the CompuCell3D modeling environment.* Mathematical biosciences and engineering: MBE, 2008. **5**(2): p. 355.

99. Swat, M.H., et al., *CompuCell3D Reference Manual Version 3.6. 2.* Biocomplexity Institute and Department of Physics, 2012.

100. Dobre, T.G. and J.G.S. Marcano, *Chemical engineering: Modeling, simulation and similitude*. 2007: John Wiley & Sons.

101. Orlande, H.R., et al., *Finite difference methods in heat transfer*. 2017: CRC press.

102. Reddy, J.N., *An introduction to the finite element method*. Vol. 2. 1993: McGraw-hill New York.

103. Stewart, P.S. and M.J. Franklin, *Physiological heterogeneity in biofilms.* Nature Reviews Microbiology, 2008. **6**(3): p. 199-210.

104. Bayles, K.W., *The biological role of death and lysis in biofilm development.* Nature Reviews Microbiology, 2007. **5**(9): p. 721-726.

105. Nikaido, H., *Multidrug resistance in bacteria.* Annual review of biochemistry, 2009. **78**: p. 119-146.

106. Stewart, P.S. and J.W. Costerton, *Antibiotic resistance of bacteria in biofilms.* The lancet, 2001. **358**(9276): p. 135-138.

107. Haagensen, J.A., et al., *Differentiation and distribution of colistin-and sodium dodecyl sulfate-tolerant cells in Pseudomonas aeruginosa biofilms.* Journal of bacteriology, 2007. **189**(1): p. 28-37.

108. Haagensen, J., et al., *Spatiotemporal pharmacodynamics of meropenem-and tobramycin-treated Pseudomonas aeruginosa biofilms.* Journal of Antimicrobial Chemotherapy, 2017.

109. Wood, T.K., S.J. Knabel, and B.W. Kwan, *Bacterial persister cell formation and dormancy.* Applied and environmental microbiology, 2013. **79**(23): p. 7116-7121.

110. Organization, W.H. *WHO publishes list of bacteria for which new antibiotics are urgently needed*. 2017, February 27; Available from: http://www.who.int/mediacentre/news/releases/2017/bacteria-antibiotics-needed/en/.

111. Kim, W., et al., *Spaceflight promotes biofilm formation by Pseudomonas aeruginosa.* PloS one, 2013. **8**(4): p. e62437.

112. Hentzer, M., et al., *Attenuation of Pseudomonas aeruginosa virulence by quorum sensing inhibitors.* The EMBO journal, 2003. **22**(15): p. 3803-3815.

113. Pamp, S.J., et al., *Tolerance to the antimicrobial peptide colistin in Pseudomonas aeruginosa biofilms is linked to metabolically active cells, and depends on the pmr and mexAB-oprM genes.* Molecular microbiology, 2008. **68**(1): p. 223-240.

114. Lobritz, M.A., et al., *Antibiotic efficacy is linked to bacterial cellular respiration.* Proceedings of the National Academy of Sciences, 2015. **112**(27): p. 8173-8180.

115. Chiang, W.-C., et al., *The metabolically active subpopulation in Pseudomonas aeruginosa biofilms survives exposure to membrane-targeting antimicrobials via distinct molecular mechanisms.* FEMS Immunology & Medical Microbiology, 2012. **65**(2): p. 245-256.

116. Chua, S.L., et al., *Selective labelling and eradication of antibiotic-tolerant bacterial populations in Pseudomonas aeruginosa biofilms.* Nature communications, 2016. **7**.

117. Bjarnsholt, T., et al., *Pseudomonas aeruginosa tolerance to tobramycin, hydrogen peroxide and polymorphonuclear leukocytes is quorum-sensing dependent.* Microbiology, 2005. **151**(2): p. 373-383.

118. Herrmann, G., et al., *Colistin-tobramycin combinations are superior to monotherapy concerning the killing of biofilm Pseudomonas aeruginosa.* The Journal of infectious diseases, 2010. **202**(10): p. 1585-1592.

119. Klausen, M., et al., *Involvement of bacterial migration in the development of complex multicellular structures in Pseudomonas aeruginosa biofilms.* Molecular microbiology, 2003. **50**(1): p. 61-68.

120. Wood, T.K., et al., *Motility influences biofilm architecture in Escherichia coli.* Applied microbiology and biotechnology, 2006. **72**(2): p. 361-367.

121. Pamp, S.J. and T. Tolker-Nielsen, *Multiple roles of biosurfactants in structural biofilm development by*

Pseudomonas aeruginosa. Journal of bacteriology, 2007. **189**(6): p. 2531-2539.

122. Farrell, F., et al., *Mechanically driven growth of quasi-two-dimensional microbial colonies.* Physical review letters, 2013. **111**(16): p. 168101.

123. Picioreanu, C., et al., *Microbial motility involvement in biofilm structure formation–a 3D modelling study.* Water science and technology, 2007. **55**(8-9): p. 337-343.

124. Emerenini, B.O., et al., *A mathematical model of quorum sensing induced biofilm detachment.* PloS one, 2015. **10**(7): p. e0132385.

125. Chihara, K., et al., *Mathematical modeling of dormant cell formation in growing biofilm.* Frontiers in microbiology, 2015. **6**.

126. Chua, S.L., et al., *Bis-(3´-5´)-cyclic dimeric GMP regulates antimicrobial peptide resistance in Pseudomonas aeruginosa.* Antimicrobial agents and chemotherapy, 2013. **57**(5): p. 2066-2075.

127. Sternberg, C. and T. Tolker-Nielsen, *Growing and analyzing biofilms in flow cells.* Current protocols in microbiology, 2006: p. 1B. 2.1-1B. 2.15.

128. Jacobs, M.A., et al., *Comprehensive transposon mutant library of Pseudomonas aeruginosa.* Proceedings of the National Academy of Sciences, 2003. **100**(24): p. 14339-14344.

129. Held, K., et al., *Sequence-verified two-allele transposon mutant library for Pseudomonas aeruginosa PAO1.* Journal of bacteriology, 2012. **194**(23): p. 6387-6389.

130. Beyenal, H., S.N. Chen, and Z. Lewandowski, *The double substrate growth kinetics of Pseudomonas aeruginosa.* Enzyme and Microbial Technology, 2003. **32**(1): p. 92-98.

131. Fagerlind, M.G., et al., *Dynamic modelling of cell death during biofilm development.* Journal of theoretical biology, 2012. **295**: p. 23-36.

132. Picioreanu, C., J. Vrouwenvelder, and M. Van Loosdrecht, *Three-dimensional modeling of biofouling and fluid dynamics in feed spacer channels of membrane devices.* Journal of Membrane Science, 2009. **345**(1): p. 340-354.

133. Lewandowski, Z. and H. Beyenal, *Fundamentals of biofilm research*. 2013: CRC press.

134. Glazier, J.A., A. Balter, and N. Poplawski, *II. 1 Magnetization to morphogenesis: A brief history of the Glazier-Graner-Hogeweg Model*. Single-Cell-Based Models in Biology and Medicine, 2007: p. 79.

135. Balter, A., et al., *II. 4 The Glazier - Graner - Hogeweg Model: Extensions, Future Directions, and Opportunities for Further Study*. Mathematics and Biosciences in Interaction, 2007: p. 151.

136. Gibiansky, M.L., et al., *Bacteria use type IV pili to walk upright and detach from surfaces*. Science, 2010. **330**(6001): p. 197-197.

137. Swat, M.H., et al., *Multi-scale modeling of tissues using CompuCell3D*. Methods in cell biology, 2012. **110**: p. 325.

138. Williamson, K.S., et al., *Heterogeneity in Pseudomonas aeruginosa biofilms includes expression of ribosome hibernation factors in the antibiotic-tolerant subpopulation and hypoxia-induced stress response in the metabolically active population*. Journal of bacteriology, 2012. **194**(8): p. 2062-2073.

139. Stewart, P.S., et al., *Contribution of stress responses to antibiotic tolerance in Pseudomonas aeruginosa biofilms*. Antimicrobial agents and chemotherapy, 2015. **59**(7): p. 3838-3847.

140. Yum, H.-K., et al., *Recurrent Pseudomonas aeruginosa Infection in Chronic Lung Diseases: Relapse or Reinfection?* Tuberculosis and respiratory diseases, 2014. **77**(4): p. 172-177.

141. Walters, M.C., et al., *Contributions of antibiotic penetration, oxygen limitation, and low metabolic activity to tolerance of Pseudomonas aeruginosa biofilms to ciprofloxacin and tobramycin*. Antimicrobial agents and chemotherapy, 2003. **47**(1): p. 317-323.

142. Darch, S.E., et al., *Density-dependent fitness benefits in quorum-sensing bacterial populations*. Proceedings of the National Academy of Sciences of the United States of America, 2012. **109**(21): p. 8259-8263.

143. Papenfort, K. and B.L. Bassler, *Quorum sensing signal–response systems in Gram-negative bacteria.* Nature Reviews: Microbiology, 2016. **14**: p. 576-588.

144. Jousset, A., et al., *Evolutionary history predicts the stability of cooperation in microbial communities.* Nature Communications, 2013. **4**: p. 2573.

145. Wang, M., et al., *Quorum sensing and policing of Pseudomonas aeruginosa social cheaters.* Proceedings of the National Academy of Sciences of the United States of America, 2015. **112**(7): p. 2187-2191.

146. Dandekar, A.A., S. Chugani, and E.P. Greenberg, *Bacterial quorum sensing and metabolic incentives to cooperate.* Science, 2012. **338**(6104): p. 264-266.

147. Whiteley, M., S.P. Diggle, and E.P. Greenberg, *Progress in and promise of bacterial quorum sensing research.* Nature, 2017. **551**: p. 313-320.

148. Oh, H.-S. and C.-H. Lee, *Origin and evolution of quorum quenching technology for biofouling control in MBRs for wastewater treatment.* Journal of Membrane Science, 2018. **554**: p. 331-345.

149. Tan, C.H., et al., *The role of quorum sensing signalling in EPS production and the assembly of a sludge community into aerobic granules.* The ISME Journal, 2014. **8**(6): p. 1186-1197.

150. Tan, C.H., et al., *Community quorum sensing signalling and quenching: microbial granular biofilm assembly.* npj Biofilms and Microbiomes, 2015. **1**: p. 15006.

151. D'Angelo-Picard, C., et al., *Diversity of N-acyl homoserine lactone-producing and-degrading bacteria in soil and tobacco rhizosphere.* Environmental Microbiology, 2005. **7**(11): p. 1796-1808.

152. Muras, A., et al., *High prevalence of quorum-sensing and quorum-quenching activity among cultivable bacteria and metagenomic sequences in the Mediterranean sea.* Genes, 2018. **9**(2): p. 100.

153. Bjarnsholt, T., et al., *The in vivo biofilm.* Trends in Microbiology, 2013. **21**(9): p. 466-474.

154. Stacy, A., et al., *The biogeography of polymicrobial infection.* Nature Reviews: Microbiology, 2015. **14**: p. 93-105.

155. Decho, A.W., et al., *Autoinducers extracted from microbial mats reveal a surprising diversity of N-acylhomoserine lactones (AHLs) and abundance changes that may relate to diel pH.* Environmental Microbiology, 2009. **11**(2): p. 409-420.

156. Flemming, H.-C., et al., *Biofilms: an emergent form of bacterial life.* Nature Reviews: Microbiology, 2016. **14**: p. 563-575.

157. Kim, M.K., et al., *Local and global consequences of flow on bacterial quorum sensing.* Nature Microbiology, 2016. **1**(1): p. 15005.

158. Dilanji, G.E., et al., *Quorum activation at a distance: spatiotemporal patterns of gene regulation from diffusion of an autoinducer signal.* Journal of the American Chemical Society, 2012. **134**(12): p. 5618-5626.

159. Flickinger, S.T., et al., *Quorum sensing between Pseudomonas aeruginosa biofilms accelerates cell growth.* Journal of the American Chemical Society, 2011. **133**(15): p. 5966-5975.

160. Connell, J.L., et al., *Real-time monitoring of quorum sensing in 3D-printed bacterial aggregates using scanning electrochemical microscopy.* Proceedings of the National Academy of Sciences of the United States of America, 2014. **111**(51): p. 18255-18260.

161. Darch, S.E., et al., *Spatial determinants of quorum signaling in a Pseudomonas aeruginosa infection model.* Proceedings of the National Academy of Sciences of the United States of America, 2018.

162. Oh, H.-S., et al., *Quorum quenching bacteria can be used to inhibit the biofouling of reverse osmosis membranes.* Water Research, 2017. **112**: p. 29-37.

163. Mohanty, A., C.H. Tan, and B. Cao, *Impacts of nanomaterials on bacterial quorum sensing: differential effects on different signals.* Environmental Science: Nano, 2016. **3**(2): p. 351-356.

164. Andersen, J.B., et al., *gfp-based N-acyl homoserine-lactone sensor systems for detection of bacterial communication.* Applied and Environmental Microbiology, 2001. **67**(2): p. 575-585.

165. Nielsen, P.H., et al., *A conceptual ecosystem model of microbial communities in enhanced biological phosphorus removal plants.* Water Research, 2010. **44**(17): p. 5070-5088.

166. Almstrand, R., et al., *New methods for analysis of spatial distribution and coaggregation of microbial populations in complex biofilms.* Applied and Environmental Microbiology, 2013. **79**(19): p. 5978-5987.

167. Stewart, P.S., *Diffusion in biofilms.* Journal of Bacteriology, 2003. **185**(5): p. 1485-1491.

168. Czajkowski, R., et al., *Inactivation of AHLs by Ochrobactrum sp. A44 depends on the activity of a novel class of AHL acylase.* Environmental Microbiology Reports, 2011. **3**(1): p. 59-68.

169. Charlton, T.S., et al., *A novel and sensitive method for the quantification of N-3-oxoacyl homoserine lactones using gas chromatography–mass spectrometry: application to a model bacterial biofilm.* Environmental Microbiology, 2000. **2**(5): p. 530-541.

170. Hense, B.A., et al., *Does efficiency sensing unify diffusion and quorum sensing?* Nature Reviews: Microbiology, 2007. **5**(3): p. 230-239.

171. Quiñones, B., G. Dulla, and S.E. Lindow, *Quorum sensing regulates exopolysaccharide production, motility, and virulence in Pseudomonas syringae.* Molecular Plant-Microbe Interactions, 2005. **18**(7): p. 682-693.

172. Von Bodman, S.B., W.D. Bauer, and D.L. Coplin, *Quorum sensing in plant-pathogenic bacteria.* Annual Review of Phytopathology, 2003. **41**(1): p. 455-482.

173. Von Bodman, S.B., D.R. Majerczak, and D.L. Coplin, *A negative regulator mediates quorum-sensing control of exopolysaccharide production in Pantoea stewartii subsp. stewartii.* Proceedings of the National Academy of Sciences of the United States of America, 1998. **95**(13): p. 7687-7692.

174. Diggle, S.P., et al., *Cooperation and conflict in quorum-sensing bacterial populations.* Nature, 2007. **450**(7168): p. 411-414.

175. Rumbaugh, K.P., et al., *Kin selection, quorum sensing and virulence in pathogenic bacteria.* Proceedings of the Royal Society B: Biological Sciences, 2012. **279**(1742): p. 3584.

176. Song, X. and D.S. Nobes, *Experimental investigation of evaporation-induced convection in water using laser based measurement techniques.* Experimental Thermal and Fluid Science, 2011. **35**(6): p. 910-919.

177.   Carminati, A., et al., *Dynamics of soil water content in the rhizosphere.* Plant and Soil, 2010. **332**(1-2): p. 163-176.

178.   Dulla, G. and S.E. Lindow, *Quorum size of Pseudomonas syringae is small and dictated by water availability on the leaf surface.* Proceedings of the National Academy of Sciences of the United States of America, 2008. **105**(8): p. 3082-3087.

179.   Mudie, D.M., et al., *Quantification of gastrointestinal liquid volumes and distribution following a 240 mL dose of water in the fasted state.* Molecular Pharmaceutics, 2014. **11**(9): p. 3039-3047.

180.   Fetzner, S., *Quorum quenching enzymes.* Journal of Biotechnology, 2015. **201**: p. 2-14.

181.   Utari, P.D., J. Vogel, and W.J. Quax, *Deciphering physiological functions of AHL quorum quenching acylases.* Frontiers in Microbiology, 2017. **8**: p. 1123.

182.   Dong, Y.-H., et al., *Insecticidal Bacillus thuringiensis silences Erwinia carotovora virulence by a new form of microbial antagonism, signal interference.* Applied and Environmental Microbiology, 2004. **70**(2): p. 954-960.

183.   Grandclément, C., et al., *Quorum quenching: role in nature and applied developments.* FEMS Microbiology Reviews, 2015. **40**(1): p. 86-116.

184.   Malamy, M.H. and B.L. Horecker, *Release of alkaline phosphatase from cells of Escherichia coli upon lysozyme spheroplast formation.* Biochemistry, 1964. **3**(12): p. 1889-1893.

185.   Whitchurch, C.B., et al., *Extracellular DNA required for bacterial biofilm formation.* Science, 2002. **295**(5559): p. 1487-1487.

186.   Schaefer, A.L., et al., *Generation of cell-to-cell signals in quorum sensing: acyl homoserine lactone synthase activity of a purified Vibrio fischeri LuxI protein.* Proceedings of the National Academy of Sciences of the United States of America, 1996. **93**(18): p. 9505-9509.

187.   Wang, L.-H., et al., *Specificity and enzyme kinetics of the quorum-quenching N-acyl homoserine lactone lactonase (AHL-lactonase).* Journal of Biological Chemistry, 2004. **279**(14): p. 13645-13651.

188. Fekete, A., et al., *Dynamic regulation of N-acyl-homoserine lactone production and degradation in Pseudomonas putida IsoF.* FEMS Microbiology Ecology, 2010. **72**(1): p. 22-34.

189. Railsback, S.F. and V. Grimm, *Agent-based and individual-based modeling: a practical introduction*. 2011: Princeton university press.

190. Gilbert, N., *Agent-based models*. 2008: Sage.

191. Wilensky, U. and W. Rand, *An introduction to agent-based modeling: modeling natural, social, and engineered complex systems with NetLogo*. 2015: MIT Press.

192. Holcombe, M., S. Coakley, and R. Smallwood. *A general framework for agent-based modelling of complex systems*. in *Proceedings of the 2006 European conference on complex systems*. 2006. European Complex Systems Society Paris, France.

193. Li, X., et al., *Skin stem cell hypotheses and long term clone survival–explored using agent-based modelling.* Scientific reports, 2013. **3**: p. 1904.

194. Luke, S., et al., *Mason: A multiagent simulation environment.* Simulation, 2005. **81**(7): p. 517-527.

195. Lardon, L.A., et al., *iDynoMiCS: next-generation individual-based modelling of biofilms.* Environmental microbiology, 2011. **13**(9): p. 2416-2434.

196. Jayathilake, P.G., et al., *A mechanistic individual-based model of microbial communities.* PloS one, 2017. **12**(8): p. e0181965.

197. Sheraton, M., et al., *Mesoscopic energy minimization drives Pseudomonas aeruginosa biofilm morphologies and consequent stratification of antibiotic activity based on cell metabolism.* Antimicrobial agents and chemotherapy, 2018: p. AAC. 02544-17.

198. Akanuma, T., et al., *Memory of cell shape biases stochastic fate decision-making despite mitotic rounding.* Nature communications, 2016. **7**: p. 11963.

199. Li, J.F. and J. Lowengrub, *The effects of cell compressibility, motility and contact inhibition on the growth of tumor cell clusters using the Cellular Potts Model.* Journal of theoretical biology, 2014. **343**: p. 79-91.

200.   Hester, S.D., et al., *A multi-cell, multi-scale model of vertebrate segmentation and somite formation.* PLoS computational biology, 2011. **7**(10): p. e1002155.

201.   Sutherland, I.W., *The biofilm matrix–an immobilized but dynamic microbial environment.* Trends in microbiology, 2001. **9**(5): p. 222-227.

202.   Roberts, M.E. and P.S. Stewart, *Modelling protection from antimicrobial agents in biofilms through the formation of persister cells.* Microbiology, 2005. **151**(1): p. 75-80.

203.   Mah, T.-F.C. and G.A. O'toole, *Mechanisms of biofilm resistance to antimicrobial agents.* Trends in microbiology, 2001. **9**(1): p. 34-39.

204.   Liu, T., et al., *Effect of fluid flow on biofilm formation and microbiologically influenced corrosion of pipelines in oilfield produced water.* Journal of Petroleum Science and Engineering, 2017. **156**: p. 451-459.

205.   Vigneron, A., I.M. Head, and N. Tsesmetzis, *Damage to offshore production facilities by corrosive microbial biofilms.* Applied microbiology and biotechnology, 2018. **102**(6): p. 2525-2533.

206.   George, R., U. Kamachi Mudali, and B. Raj, *Characterizing biofilms for biofouling and microbial corrosion control in cooling water systems.* Anti-Corrosion Methods and Materials, 2016. **63**(6): p. 477-489.

207.   Fortunato, L., et al., *Spatially-resolved in-situ quantification of biofouling using optical coherence tomography (OCT) and 3D image analysis in a spacer filled channel.* Journal of Membrane Science, 2017. **524**: p. 673-681.

208.   Vrouwenvelder, J., et al., *Pressure drop increase by biofilm accumulation in spiral wound RO and NF membrane systems: role of substrate concentration, flow velocity, substrate load and flow direction.* Biofouling, 2009. **25**(6): p. 543-555.

209.   Jessen, B. and L. Lammert, *Biofilm and disinfection in meat processing plants.* International biodeterioration & biodegradation, 2003. **51**(4): p. 265-269.

210.   Stewart, P.S., *A model of biofilm detachment.* Biotechnology and Bioengineering, 1993. **41**(1): p. 111-117.

211. Peyton, B.M. and W.G. Characklis, *A statistical analysis of the effect of substrate utilization and shear stress on the kinetics of biofilm detachment.* Biotechnology and bioengineering, 1993. **41**(7): p. 728-735.

212. Li, C., Y. Zhang, and C. Yehuda, *Individual based modeling of Pseudomonas aeruginosa biofilm with three detachment mechanisms.* RSC Advances, 2015. **5**(96): p. 79001-79010.

213. Picioreanu, C., M.C. Van Loosdrecht, and J.J. Heijnen, *Two-dimensional model of biofilm detachment caused by internal stress from liquid flow.* Biotechnology and bioengineering, 2001. **72**(2): p. 205-218.

214. Tierra, G., et al., *Multicomponent model of deformation and detachment of a biofilm under fluid flow.* Journal of The Royal Society Interface, 2015. **12**(106): p. 20150045.

215. Chindapol, N., et al., *Modelling growth and form of the scleractinian coral Pocillopora verrucosa and the influence of hydrodynamics.* PLoS computational biology, 2013. **9**(1): p. e1002849.

216. Závodszky, G., et al., *Red blood cell and platelet diffusivity and margination in the presence of cross-stream gradients in blood flows.* Physics of Fluids, 2019. **31**(3): p. 031903.

217. Rupp, C.J., C.A. Fux, and P. Stoodley, *Viscoelasticity of Staphylococcus aureus biofilms in response to fluid shear allows resistance to detachment and facilitates rolling migration.* Applied and environmental microbiology, 2005. **71**(4): p. 2175-2178.

218. Stoodley, P., et al., *Structural deformation of bacterial biofilms caused by short-term fluctuations in fluid shear: An in situ investigation of biofilm rheology.* Biotechnology and bioengineering, 1999. **65**(1): p. 83-92.

219. Stoodley, P., et al., *Biofilm material properties as related to shear-induced deformation and detachment phenomena.* Journal of Industrial Microbiology and Biotechnology, 2002. **29**(6): p. 361-367.

220. Versteeg, H.K. and W. Malalasekera, *An introduction to computational fluid dynamics: the finite volume method.* 2007: Pearson Education.

221. Wang, Q. and T. Zhang, *Review of mathematical models for biofilms.* Solid State Communications, 2010. **150**(21-22): p. 1009-1022.

222. Swat, M.H., et al., *Multi-scale modeling of tissues using CompuCell3D*, in *Methods in cell biology*. 2012, Elsevier. p. 325-366.

223. Swat, M.H., et al., *Compucell3d reference manual version-3.7. 2*.

224. Valen-Sendstad, K., et al., *A comparison of finite element schemes for the incompressible Navier–Stokes equations*, in *Automated Solution of Differential Equations by the Finite Element Method*. 2012, Springer. p. 399-420.

225. Rusconi, R., et al., *Secondary flow as a mechanism for the formation of biofilm streamers.* Biophysical journal, 2011. **100**(6): p. 1392-1399.

226. Valiei, A., et al., *A web of streamers: biofilm formation in a porous microfluidic device.* Lab on a Chip, 2012. **12**(24): p. 5133-5137.

227. Drescher, K., et al., *Biofilm streamers cause catastrophic disruption of flow with consequences for environmental and medical systems.* Proceedings of the National Academy of Sciences, 2013. **110**(11): p. 4345-4350.

228. Dhatt, G., E. LefranÃ, and G. Touzot, *Finite element method*. 2012: John Wiley & Sons.

229. Chen, S. and G.D. Doolen, *Lattice Boltzmann method for fluid flows.* Annual review of fluid mechanics, 1998. **30**(1): p. 329-364.

230. Zhang, L., et al., *Multiscale agent-based cancer modeling.* Journal of mathematical biology, 2009. **58**(4-5): p. 545-559.

231. Fox, G.C., et al., *Solving problems on concurrent processors. Vol. 1: General techniques and regular problems*. 1988: Prentice-Hall, Inc.

232. Fozard, J.A., et al., *Inhibition of quorum sensing in a computational biofilm simulation.* Biosystems, 2012. **109**(2): p. 105-114.

233. Picioreanu, C., M.C. Van Loosdrecht, and J.J. Heijnen, *Two-dimensional model of biofilm detachment caused by internal*

stress from liquid flow. Biotechnology & Bioengineering, 2001. **72**(2): p. 205-218.

234. Weitz, J.S., H. Hartman, and S.A. Levin, *Coevolutionary arms races between bacteria and bacteriophage.* Proceedings of the National Academy of Sciences of the United States of America, 2005. **102**(27): p. 9535-9540.

235. Han, K. and O. Levenspiel, *Extended Monod kinetics for substrate, product, and cell inhibition.* Biotechnology and bioengineering, 1988. **32**(4): p. 430-447.

236. Alowayyed, S., et al., *Load balancing of parallel cell-based blood flow simulations.* Journal of Computational Science, 2018. **24**: p. 1-7.

237. Cytowski, M. and Z. Szymanska, *Large-scale parallel simulations of 3d cell colony dynamics.* Computing in Science & Engineering, 2014. **16**(5): p. 86-95.

238. Logg, A., K.-A. Mardal, and G. Wells, *Automated solution of differential equations by the finite element method: The FEniCS book.* Vol. 84. 2012: Springer Science & Business Media.

239. Alnæs, M., et al., *The FEniCS project version 1.5.* Archive of Numerical Software, 2015. **3**(100): p. 9-23.

240. Guermond, J.-L., P. Minev, and J. Shen, *An overview of projection methods for incompressible flows.* Computer methods in applied mechanics and engineering, 2006. **195**(44-47): p. 6011-6045.

241. Geuzaine, C. and J.F. Remacle, *Gmsh: A 3-D finite element mesh generator with built-in pre-and post-processing facilities.* International journal for numerical methods in engineering, 2009. **79**(11): p. 1309-1331.

242. Guyer, J.E., D. Wheeler, and J.A. Warren, *FiPy: Partial differential equations with Python.* Computing in Science & Engineering, 2009. **11**(3).

243. Heroux, M.A., et al., *An overview of the Trilinos project.* ACM Transactions on Mathematical Software (TOMS), 2005. **31**(3): p. 397-423.

244. Axner, L., et al., *Performance evaluation of a parallel sparse lattice Boltzmann solver.* Journal of Computational Physics, 2008. **227**(10): p. 4895-4911.

10   Summary

The response of biofilms to any external stimuli is a cumulative response aggregated from individual bacteria residing within the biofilm. Any perturbation at a microscopic level manifests response at a macroscopic scale. Therefore, the organizational complexity of biofilm can be studied effectively by understanding the bacterial interaction at cell level. The overall aim of the thesis is to explore the complex evolutionary behaviour of bacterial biofilms subject to external perturbations. This thesis is divided into three major studies based on the type of perturbation analysed in the study. These studies answer the fundamental questions associated with the complexity of biofilm development. The first study analyses the physics behind the development of mushroom-shaped complex structures from the influence of nutrient cues in Pseudomonas aeruginosa biofilms. Glazier-Graner-Hogeweg model is used to simulate the cell characteristics such a motility, proliferation, and adhesion in the study. From the study, it is observed that chemotaxis of bacterial cells towards nutrient source is one of the major precursors for formation of mushroom shaped structures. Also, formation of such cap-and-stalk structures leads to the development and segregation of bacterial antibiotic resistance within the biofilm. The objective of the second study is to analyse the impact of ambient environmental conditions on the inter-biofilm quorum sensing signalling. The study reveals that the

dynamics of inter-biofilm bacterial communications is significantly affected by the characteristics of the fluid medium surrounding the biofilm. Using a hybrid convection-diffusion-reaction model, the simulations predict the diffusivity of quorum sensing molecules, the spatiotemporal variations of quorum sensing signal concentrations and consequently, the competition outcome between quorum sensing and quorum quenching mutant bacterial communities present under various environmental conditions. The mechanical effects associated with the fluid-biofilm interaction is addressed in the third study. A novel fluid-structure interaction model based on fluid dynamics and structural energy minimization is developed in the study. Model simulations are used to analyse the detachment and surface effects of the fluid stresses on multi-species biofilms. In addition to the mechanistic models described, a separate study is carried out to estimate the computational efficiency of the biofilm growth model and predict the optimal processor allocation for simulating different stages of biofilm growth.

11 Publications

Sheraton, M.V., Yam, J.K.H., Tan, C.H., Oh, H.S., Mancini, E., Yang, L., Rice, S.A. and Sloot, P.M.A., 2018. Mesoscopic Energy Minimization Drives *Pseudomonas aeruginosa* Biofilm Morphologies and Consequent Stratification of Antibiotic Activity Based on Cell Metabolism. Antimicrobial agents and chemotherapy, 62(5), pp.e02544-17.

- Contribution: Sloot conceived the research, Sheraton developed the simulation model and helped in designing the experiments. Yam carried out the experiments. Sheraton wrote the manuscript, other authors contributed in revision of the manuscript.

Sheraton, M.V. and Sloot, P.M.A.,2018. Parallel Performance Analysis of Bacterial Biofilm Simulation Models. Lecture Notes in Computer Science (LNCS).

- Contribution: Sloot conceived the research, Sheraton developed the simulation model and wrote the manuscript. The other author contributed in revision of the manuscript.

Tan C.H. †, Oh H.S. †, Sheraton M.V. †, Mancini E., Chye1 J.L.S., Kjelleberg S., Sloot P.M.A., and Rice S.A. The Impact of Mass Transfer and Quorum Quenching on Quorum Sensing Behaviors. Submitted to Science Advances.

- Contribution: Rice and Sloot conceived the research, Sheraton developed the simulation model and helped in designing the experiments. Oh and Tan carried out the experiments. Sheraton wrote the modelling part of the manuscript, Oh and Tan wrote the experimental part of the manuscript. Other authors contributed in revision of the manuscript. † - equal contribution.

Sheraton M.V., Melnikov V and Sloot P. M. A Prediction and Quantification of Bacterial Biofilm Detachment Using Glazier-Graner-Hogeweg Method-Based Model Simulations. In-preparation for Journal of Theoretical Biology.

- Contribution: Sloot conceived the research, Sheraton developed the simulation model and wrote the manuscript. Valentin carried out part of the simulations and helped in manuscript preparation. All authors contributed in revision of the manuscript.

12   Acknowledgements

Thank you, ***Peter***, for helping me understand how science and philosophy are intertwined.

My sincere thanks to all the co-authors - biologists and computer scientists, who put aside all their disciplinary biases and collaborated on the projects in this thesis.